Pressure profiles of plasmas confined in the field of a dipole magnet

Matthew Stiles Davis

SUBMITTED IN PARTIAL FULFILLMENT OF THE

REQUIREMENTS FOR THE DEGREE OF

DOCTOR OF PHILOSOPHY

IN THE GRADUATE SCHOOL OF ARTS AND SCIENCES

COLUMBIA UNIVERSITY

2013

ABSTRACT

Pressure profiles of plasmas confined in the field of a dipole magnet

Matthew Stiles Davis

Understanding the maintenance and stability of plasma pressure confined by a strong magnetic field is a fundamental challenge in both laboratory and space plasma physics. Using magnetic and X-ray measurements on the Levitated Dipole Experiment (LDX), the equilibrium plasma pressure has been reconstructed, and variations of the plasma pressure for different plasma conditions have been examined. The relationship of these profiles to the magnetohydrodynamic (MHD) stability limit, and to the enhanced stability limit that results from a fraction of energetic trapped electrons, has been analyzed. In each case, the measured pressure profiles and the estimated fractional densities of energetic electrons were qualitatively consistent with expectations of plasma stability.

LDX confines high temperature and high pressure plasma in the field of a superconducting dipole magnet. The strong dipole magnet can be either mechanically supported or magnetically levitated. When the dipole was mechanically supported, the plasma density profile was generally uniform while the plasma pressure was highly peaked. The uniform density was attributed to the thermal plasma being rapidly lost along the field to the mechanical supports. In contrast, the strongly peaked plasma pressure resulted from a fraction of energetic, mirror trapped electrons created by microwave heating at the electron cyclotron resonance (ECRH). These hot electrons are known to be gyrokinetically stabilized by the background plasma and can adopt pressure profiles steeper than the MHD limit. X-ray measurements indicated that this hot electron population could be described by an energy distribution in the range 50-100 keV. Combining information from the magnetic reconstruc-

tion of the pressure profile, multi-chord interferometer measurements of the electron density profile, and X-ray measurements of the hot electron energy distribution, the fraction of energetic electrons at the pressure peak was estimated to be $\sim 35\%$ of the total electron population.

When the dipole was magnetically levitated the plasma density increased substantially because particle losses to the mechanical supports were eliminated so particles could only be lost via slower cross-field transport processes. The pressure profile was observed to be broader during levitated operation than it was during supported operation, and the pressure appeared to be contained in both a thermal population and an energetic electron population. X-ray spectra indicated that the X-rays came from a similar hot electron population during levitated and supported operation; however, the hot electron fraction was an order of magnitude smaller during levitated operation ($< 3\%$ of the total electron population).

Pressure gradients for both supported and levitated plasmas were compared to the MHD limit. Levitated plasmas had pressure profiles that were (i) steeper than, (ii) shallower than, or (iii) near the MHD limit dependent on plasma conditions. However, those profiles that exceeded the MHD limit were observed to have larger fractions of energetic electrons. When the dipole magnet was supported, high pressure plasmas always had profiles that exceeded the MHD interchange stability limit, but the high pressure in these plasmas appeared to arise entirely from a population of energetic trapped electrons.

Contents

List of Figures

List of Tables

Acknowledgements

I would like to thank my thesis advisor, Professor Michael Mauel, for his guidance, encouragement, and limitless enthusiasm throughout my time as a graduate student. I am especially grateful to have had the opportunity to work on the Levitated Dipole Experiment and to have worked with the people that comprise the LDX team. The many conversations I have had with Jay Kesner and Darren Garnier have been insightful, engaging, and invaluable both to my work in this thesis and to my life beyond it. I also thank Rick Lations, Don Strahan, Alex Zhukovsky, and Phil Michael without whom LDX could not have run. Furthermore, I thank my fellow graduate students Jennifer Ellsworth, Matthew Worstell, Brian Grierson, Alex Boxer, Dennis Boyle, and Max Roberts for enriching both my educational and social experience in New York City and in Cambridge.

On a personal note, I thank my family for their love and support. To my mother, father, sister, Jan and Nik, you are the foundation and inspiration for all my endeavors.

Chapter 1

Introduction

The Levitated Dipole Experiment (LDX) [1, 2] has been built to study the confinement of plasmas in a magnetic dipole field. One of the principal research objectives of the experiment is to test whether plasmas confined by a magnetically levitated current ring adopt the highly peaked density and pressure profiles observed in planetary magnetospheres and predicted by theory [3, 4, 5, 6]. The pressure profiles are predicted to relax to where the plasma is marginally stable to the ideal magnetohydrodynamic (MHD) interchange mode [4, 7]:

$$\delta\left(pV^{\gamma}\right) = 0 \tag{1.1}$$

where p is the plasma pressure, V is the differential flux-tube volume ($V \equiv \oint dl/B$), and γ is the ratio of specific heats ($\gamma = 5/3$ for a three dimensional system). Equation (1.1) states that the entropy density factor (defined as $G \equiv pV^{\gamma}$) is a constant. Because the flux-tube volume in a dipole increases dramatically with radius ($V \sim R^4$) eq. (1.1) implies that the pressure increases dramatically near the dipole. The density profiles are predicted to relax to where the number of particles per unit flux-tube volume is constant [5, 6].

Dipole confined plasmas have been extensively explored because of their presence in nature, specifically, planetary magnetospheres, which have largely dipolar magnetic fields. In the past century, man-made satellites have travelled through planetary magnetospheres and observed trapped plasma with peaked density [5, 8, 9] and pressure profiles [4]. More recent studies have brought interest in dipole confinement back to Earth with the possibility of using a levitated dipole as a nuclear fusion reactor [3, 6, 10, 11].

An important idea behind plasma confinement by a dipole magnetic field is that the plasma will tend toward invariant density and pressure profiles. Invariant profiles are profiles that remain unchanged during interchange motion [6]. For invariant pressure and density profiles plasma flux-tubes can exchange position without changing either the pressure or the density profile. The remarkable feature of invariant profiles is that their invariant nature reflects a flattening of gradients in magnetic flux-space, not real space. Therefore, if the magnetic flux-tube volume varies greatly in real space, as it does in a dipole field, the invariant profiles can be very peaked. Equation (1.1), which is derived under the collisional assumption of ideal MHD, describes an invariant pressure profile. The same invariant pressure profile can be derived with a collisionless gyrokinetic approach [6, 12].

The invariant density profile has an equal number of particles per flux-tube:

$$\delta\left(nV\right) = 0 \tag{1.2}$$

where n is the plasma density and V is the differential flux-tube volume. For an invariant density profile an exchange of flux-tubes does not change the density profile [5, 6].

The significance of invariant profiles is that they lack the density, temperature, and pressure gradients (gradients in magnetic flux-space) that typically drive instabilities in magnetized plasmas. Like tokamaks, dipole confined plasmas are potentially unstable to

both pressure gradient driven MHD modes, and density or temperature gradient driven drift modes. Theoretical studies have shown that stability to the MHD interchange mode is sufficient for stability to MHD ballooning modes [13, 14]. Studies of drift modes [15, 16, 17, 18] have shown that the critical parameter for stability is $\eta \equiv \frac{d\ln T}{d\ln n} = \frac{\nabla T}{T}/\frac{\nabla n}{n}$, and the most stable operating point is $\eta = \gamma - 1 = 2/3$, which combined with eq. (1.1) corresponds to the invariant density and temperature profiles.

That the invariant profiles correspond to the marginal stability point for MHD interchange modes might cause concern since any violation of MHD stability leads to a rapid loss of the plasma in most plasma confinement devices. However, in the dipole this stability limit is viewed as a 'soft' limit. Rather than cause a catastrophic loss of the plasma, MHD interchange modes drive convective cells that act to bring the plasma back to the marginally stable profile. Quasilinear [19] and nonlinear [20] analyses show that a violation of the marginal stability criteria causes convective transport that restores the invariant density and pressure profiles. Gyrokinetic simulations [21] show that entropy-mode driven transport drives the density and pressure toward their invariant profiles ($\eta = 2/3$).

Levitation is critical to the formation of invariant profiles on LDX because it eliminates losses along the magnetic field. When the magnetic dipole is mechanically supported invariant profiles are not observed. The density profile tends to be flat because thermal particles are lost along the magnetic field to the supports. The pressure tends to be highly peaked, which is consistent with the pressure consisting of a hot, mirror trapped electron population that forms as a result of electron cyclotron resonance heating (ECRH). When the dipole is magnetically levitated particle losses to the supports are eliminated as particles are able to travel along the field through the center of the dipole. Previous work on LDX has shown that when the floating coil is levitated the plasma adopts a nearly invariant density profile

[22, 23]. It is predicted that the turbulent mixing of flux-tubes that drives the plasma to adopt the nearly invariant density profile will also drive the plasma toward the invariant pressure profile.

The work in this thesis aims to (1) measure the pressure profile, (2) examine variations of the plasma pressure for different plasma conditions, and (3) analyze the pressure gradient, particularly its relation to the MHD stability limit: $\delta(pV^{\gamma}) \geq 0$.

The pressure profile is measured by using magnetic sensors to reconstruct the diamagnetic current distribution in the plasma [24, 25]. For a plasma in MHD equilibrium, the gradient of the pressure profile is proportional to the current distribution ($\nabla P = \mathbf{j} \times \mathbf{B}$). Thus, with knowledge of the plasma boundary conditions (i.e., the pressure goes to zero at the plasma edge) the pressure profile of the plasma can be deduced. Challenges unique to performing a magnetic reconstruction of the pressure profile on LDX include accounting for the changes in position and current of the magnetic-flux-conserving, superconducting, levitated dipole magnet, and distinguishing between hot and thermal electron populations.

Hot electrons (> 50 keV) form on LDX as a result of the electron cyclotron resonance heating (ECRH) that is used to create and heat the plasma. Distinguishing between the hot and thermal populations is important because the hot electrons are subject to a different stability limit than the thermal plasma. Specifically, gyrokinetic stabilization of the hot electrons by the background plasma allows the hot electron pressure gradient to be steeper than the MHD limit. The pressure measured by the magnetic reconstruction includes both the hot electrons and the thermal plasma. Three methods for estimating the portion of the pressure in the thermal plasma are (1) comparing supported and levitated plasmas, (2) measuring the decay times of the stored energy [26], and (3) measuring the X-ray emission.

Measurements presented in this thesis show that levitated plasmas adopt pressure profiles

that are broader than the pressure profiles observed during supported operation. During supported operation the plasma pressure gradient is observed to exceed the MHD limit and X-ray measurements indicate the presence of hot electrons that can be described by a log-linear energy distribution in the range 50-100 keV. The plasma pressure during supported operation is interpreted to consist entirely of hot, mirror trapped electrons.

During levitated operation the plasma pressure gradient is less steep than it is during supported operation. Dependent on plasma conditions the pressure gradient is observed to exceed or not exceed the MHD limit. Levitated plasmas with pressure profiles that exceed the MHD limit are interpreted to have a significant portion of the pressure in hot electrons. X-ray measurements (serving as a proxy for the number of hot electrons) indicate that plasmas with fewer hot electrons tend to have broader pressure profiles that do not exceed the MHD limit.

This thesis is organized as follows: Chapter 2 discusses the dipole fusion reactor concept and the invariant density and pressure profiles that are fundamental to plasma confinement in a dipole. Chapter 3 describes the experiment and the experiment diagnostics. Chapter 4 details the methodology used to reconstruct the pressure profile from the magnetic measurements. Chapter 5 describes the results of magnetic reconstructions of the pressure profile for a variety of plasma shots. Chapter 6 discusses X-ray measurements that are used to characterize the hot electron population that is present in most LDX plasmas. Chapter 7 analyzes and interprets the observations presented in Chapters 5 and 6. Chapter 8 discusses conclusions and potential future work.

Chapter 2

Background

2.1 Fusion energy and the dipole

Designs for generating controlled fusion energy sort broadly into two categories: magnetic confinement fusion (MCF) and inertial confinement fusion (ICF). The principal ICF design uses multiple lasers to implode a small capsule of fusion fuel and is being tested at the National Ignition Facility (NIF) in Livermore, California [27, 28]. The principal MCF design is the tokamak. The tokamak has been extensively studied and tested over the past half century and will have its grandest manifestation in ITER (International Thermonuclear Experimental Reactor) which is currently under construction in Cadarache, France [29, 30, 31]. The promise offered by nuclear fusion, the promise of a practically inexhaustible and comparatively clean and safe energy source, combined with the difficulty in attaining it, has led to a plethora of alternative confinement designs in addition to these principal designs. The dipole is one such alternative magnetic confinement design.

The idea of using a levitated superconducting magnetic coil and a large diameter dipole

confined plasma as a fusion reactor is credited to Akira Hasegawa for his 1987 paper *A Dipole Field Fusion Reactor* [6]. However, the study of dipole confined plasmas far predate this paper. Interest in dipole confined plasmas has historically been related to their presence in nature. Planetary magnetospheres have largely dipolar magnetic fields which confine plasmas that originate in the solar wind. Investigations into the aurora by Birkeland (circa 1903-1909) led to early laboratory plasma experiments with a terrella, or 'little Earth' [32]. Later the space age drew considerable attention to plasmas in dipoles as spacecraft traveled through the magnetospheres of Earth and other planets. These spacecraft discovered large populations of trapped energetic particles with peaked density [5] and pressure profiles [4]. The dipole fusion reactor was first proposed by Bo Lehnert in 1958 [33, 34] and in the 1960s Lehnert experimentally examined the possibility of a mechanically supported dipole fusion device with magnetically shielded current leads [35].

The dipole fusion reactor as envisioned by Hasegawa [6, 10] eliminates losses to mechanical supports and current leads by magnetically levitating a superconducting coil. Plasma confined in the dipole field can then only be lost via radial, cross-field transport. This leads to the confined plasma adopting density and pressure profiles that are highly peaked near the levitated coil

$$n(R) \sim R^{-4} \tag{2.1}$$

$$p(R) \sim R^{-4\gamma} \tag{2.2}$$

$$T(R) = p(R)/n(R) \sim R^{-4(\gamma-1)} \tag{2.3}$$

where γ is the ratio of specific heats ($\gamma = 5/3$ for a three dimensional system), R is the radial coordinate, $n(R)$ is the density, $p(R)$ is the pressure, and $T(R)$ is the temperature.

From eqs. (2.1) and (2.2), the peak values of the density and pressure are related to the density and temperature at the plasma edge

$$n_{peak} = n_{edge}\left(\frac{R_{edge}}{R_{peak}}\right)^{4} \tag{2.4}$$

$$p_{peak} = p_{edge}\left(\frac{R_{edge}}{R_{peak}}\right)^{4\gamma} \tag{2.5}$$

$$T_{peak} = T_{edge}\left(\frac{R_{edge}}{R_{peak}}\right)^{4(\gamma-1)}. \tag{2.6}$$

Thus, the basic design for a dipole reactor has a small coil levitated inside of a large vacuum chamber.

A distinguishing feature of the dipole confinement design compared to other magnetic confinement designs, such as the tokamak, is that the plasma is confined outside of the coil. This allows for very good field usage and mitigates issues related to heat dissipation in the diverter since the geometry allows for a large, cooling expansion of magnetic flux. Additional merits of the dipole design are that it is inherently steady state and not prone to major disruptions since it carries only diamagnetic current [3]. Furthermore, the formation of adiabatic convective cells [36] may allow for the decoupling of the particle confinement time, τ_P, from the energy confinement time, τ_E, such that $\tau_E > \tau_P$. This would allow for the use of advanced fuels such as D-D that require the removal of fusion ash products that can otherwise build up and quench the fusion reaction [11, 37]. The primary drawback to the dipole design is the presence of the superconducting coil in the middle of the plasma. However, this engineering difficulty is mitigated by the simplicity of the coil set and its lack of interlocking coils which allows easy access to the coil for routine maintenance.

2.2 Invariant profiles

The dipole fusion concept centers around the tendency for dipole confined plasmas to adopt highly peaked density and pressure profiles. These profiles, which are peaked in real space, correspond to flattened gradients in magnetic flux-space. For the invariant density profile, there is an equal number of particles in tubes of equal magnetic flux. For the invariant pressure profile, the pressure is constant within a magnetic flux-tube and the entropy density factor (defined $G \equiv pV^{\gamma}$) is equal in tubes of equal magnetic flux. The profiles are termed invariant because an exchange of flux-tubes leaves the profiles unchanged. The invariant density and pressure profiles are

$$nV = constant \qquad \Longrightarrow \qquad n(R) \sim R^{-4} \tag{2.7}$$

$$pV^{\gamma} = constant \qquad \Longrightarrow \qquad p(R) \sim R^{-4\gamma} \tag{2.8}$$

where γ is the ratio of specific heats ($\gamma = 5/3$ for a three dimensional system), and V is the differential flux-tube volume (defined $V \equiv \oint dl/B$, and for a dipole: $V \sim R^4$).

From eqs. (2.7) and (2.8) the invariant temperature profile, $T(R)$, is

$$T \propto p(R)/n(R) \qquad \Longrightarrow \qquad T(R) \sim R^{-4(\gamma-1)} \quad . \tag{2.9}$$

The invariant profiles also describe plasmas that are marginally stable to low-frequency magnetic and electric fluctuations. From gyrokinetics the marginal stability condition is $\partial F(\mu, J, \psi)/\partial\psi = 0$, where the particle distribution function is written in terms of the adiabatic invariants of the particle motion. This condition leads to the invariant profiles for both the density and the pressure. From MHD, marginal stability to the interchange

mode ($\delta(pV^\gamma)$=0) leads to the invariant pressure profile. MHD stability of a rotating plasma corresponds to marginal stability to the centrifugally driven interchange mode ($\delta(nV)$)=0). Both the gyrokinetic approach and MHD approach are discussed further in the following sections.

2.2.1 Particle motion in a dipole

A charged particle confined in a strong magnetic field, such as a dipole, performs three periodic motions that occur on three different time scales. These periodic motions are the cyclotron motion (ω_C), the bounce motion (ω_B), and the drift motion (ω_D). The frequencies of these motions are ordered $\omega_C >> \omega_B >> \omega_D$. The fastest of these motions, the cyclotron motion, is the result of the Lorentz force causing the particle to gyrate in a small helical orbit about a magnetic field line. The second motion occurs along the magnetic field line. In a dipole, as a particle moves along the field it is reflected away from the magnetic poles provided the ratio of the particle's parallel and perpendicular energy is less than the mirror ratio minus one ($v_\parallel^2/v_\perp^2 < B_{max}/B_{min} - 1$, where B_{min} and B_{max} are the minimum and maximum magnetic field strength along the particle trajectory) [38]. As a particle moves along a field line toward the regions of higher field strength located at the poles it experiences a magnetic mirror force that pushes it back toward the region of lower field strength. Thus the particle streams along the field line bouncing between the two poles with the frequency ω_B. The slowest motion is the drift motion due to the magnetic field gradient and curvature. The inhomogeneity of the field causes a small perturbation of the cyclotron orbit that can be described as a drift of the cyclotron orbit center. The drift is in the azimuthal direction causing the particle to orbit around the dipole.

From mechanics it is known that a strictly periodic motion has an associated conserved

quantity. For example, energy is conserved in the periodic motion of a swinging pendulum. The cyclotron, bounce, and drift motions are nearly periodic but are not strictly periodic. As such, their nearly periodic motions have associated adiabatic invariants. Adiabatic invariants are constants of the motion when the parameters of the motion vary slowly. The classic illustration of an adiabatic invariant is a pendulum with a gradually shortening string. Treating the shortening pendulum as a simple oscillator with a slowly increasing frequency ($\omega = \sqrt{g/l}$) the adiabatic invariant of the shortening pendulum is E/ω [39]. The important aspect of adiabatic invariants is that they are conserved so long as the parameters of the motion change on a time scale that is long compared to the time scale of the periodic motion [40]. Table 2.1 summarizes the adiabatic invariants for particle motion in a magnetic dipole and figs. 2.1 and 2.2 illustrate the particle motions. Table 2.2 shows a list of characteristic times on LDX.

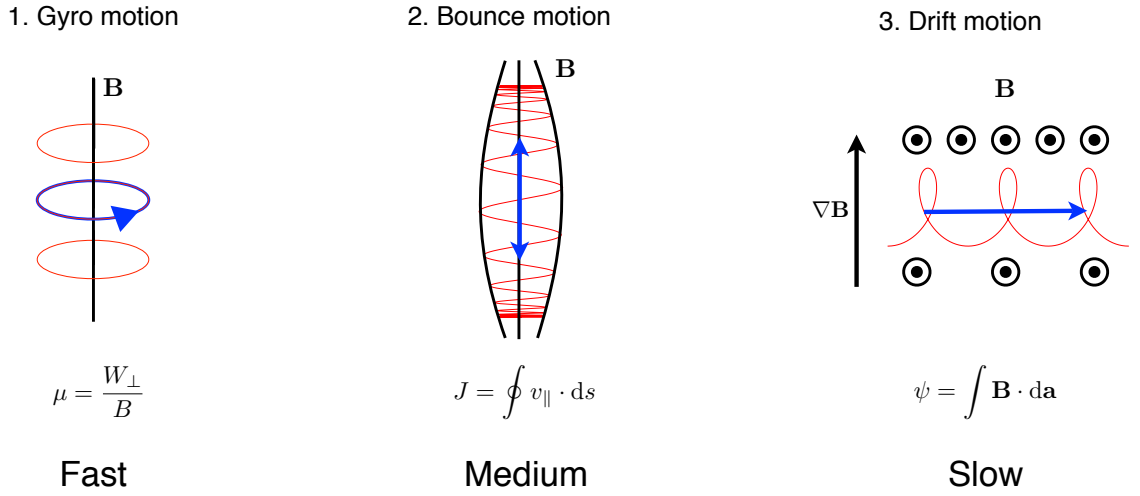

Figure 2.1: Illustration depicting the periodic particle motions in the dipole and their associated adiabatic invariants.

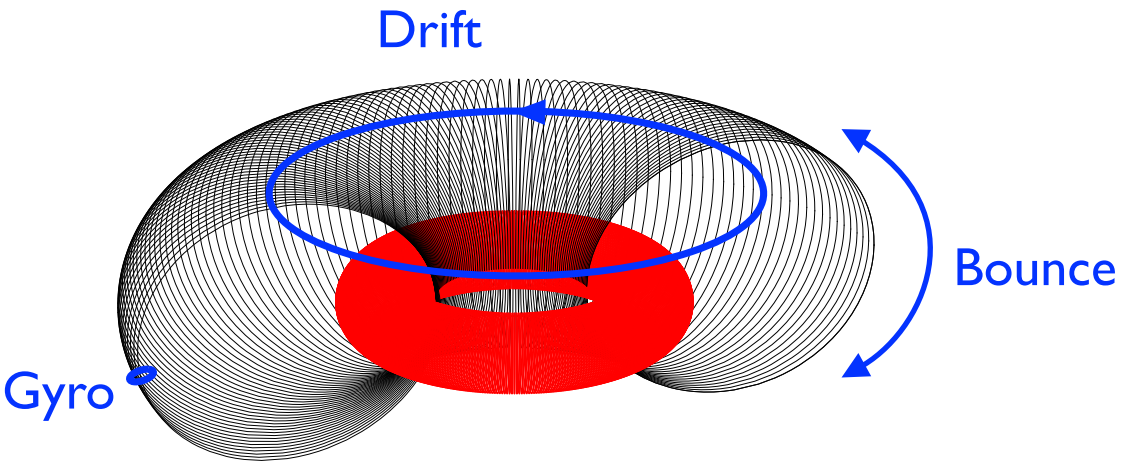

Figure 2.2: Cartoon illustration depicting particle motions in the dipole.

Symbol	Name	Motion	Definition
μ	First invariant or Magnetic moment	Cyclotron	$\frac{\frac{1}{2}mv_{\perp}^2}{B}$
J	Second invariant or Longitudinal invariant	Bounce	$\oint v_{\parallel} \cdot \mathrm{d}s$
ψ	Third invariant or Flux-invariant	Drift	$\int \mathbf{B} \cdot d\mathbf{a}$

Table 2.1: Adiabatic invariants of the motion in a dipole geometry.

T_e	$\omega_D/2\pi$	ν_{ei}	$\omega_B/2\pi$	$\omega_C/2\pi$
1 eV	11 Hz	28 MHz	260 kHz	2.5 GHz
10 eV	110 Hz	1.2 MHz	830 kHz	2.5 GHz
100 eV	1.1 kHz	48 kHz	2.6 MHz	2.5 GHz
1 keV	11 kHz	1.8 kHz	8.3 MHz	2.5 GHz
10 keV	110 kHz	68 Hz	26 MHz	2.5 GHz
100 keV	1.1 MHz	2.5 Hz	830 MHz	2.5 GHz

Table 2.2: Approximate frequencies (drift motion, ω_D, electron-ion collision, ν_{ei}, bounce motion, ω_B, and cyclotron motion, ω_C) for an electron located at a radius of 80 cm with a plasma density of $10^{18}\ m^{-3}$ in LDX.

2.2.2 Particle distribution function

A particle can be labelled by any suitable set of coordinates. A standard set of coordinates is the Cartesian coordinate system which can be used to describe a particle's position, $\mathbf{x}$, and velocity, $\mathbf{v}$. For a collection of many particles the distribution of the particles in the coordinate space is described by a distribution function, $f(\mathbf{v}, \mathbf{x})$.

The distribution function can be written in terms of the adiabatic invariants [6, 12].

$$f(\mathbf{v}, \mathbf{x}) \longrightarrow f(\mu, J, \psi) \tag{2.10}$$

Here the phase space distribution is given by the μ and J coordinates and the spatial distribution is given by the ψ coordinate [41]. The benefit of describing the distribution function in terms of adiabatic invariants rather than velocities and spatial coordinates is that it decouples the coordinates based on time scales. For a collisionless, non-interacting plasma the distribution function does not change, $\partial f(\mu, J, \psi)/\partial t = 0$. If very low frequency (ω, where $\omega << \omega_D << \omega_B << \omega_C$) fluctuations are introduced the distribution function will remain unchanged because all three of the adiabatic invariants are conserved. However, if drift-resonant ($\omega \sim \omega_D << \omega_B << \omega_C$) fluctuations are introduced the flux-invariant, ψ, is broken (i.e., it is not conserved) and the distribution function can change, $\partial f(\mu, J, \psi)/\partial t \neq 0$. The change in the distribution function will only occur in the flux coordinate since μ and J are still conserved during these low frequency fluctuations [42]. By allowing only low frequency disturbances that cause small steps in phase space the change of the distribution can be described as a diffusion in flux-space [12]

$$\frac{\partial f(\mu, J, \psi)}{\partial t} = \frac{\partial}{\partial \psi}\left(D_{\psi\psi}\frac{\partial}{\partial \psi} f(\mu, J, \psi)\right). \tag{2.11}$$

Thus, low-frequency fluctuations that break the flux-invariant while preserving μ and J lead to a diffusion of particles in flux-space. This means that plasmas confined in a magnetic dipole tend toward distributions that have an equal number of particles per flux-tube. Because the flux-tube volume varies in real space as $V \sim R^4$, the particle density is very peaked in real space

$$n \sim \frac{1}{V} \sim \frac{1}{R^4} \quad . \tag{2.12}$$

Additionally, the conservation of μ and J cause particles to gain energy as they move inward. The perpendicular energy increases in proportion to the magnetic field strength $E_\perp \sim B \sim 1/R^3$. Conservation of J causes the parallel energy to go as $E_\parallel \sim 1/R^2$ [6, 12].

2.2.3 Fluid description

Plasmas confined in a magnetic dipole can be modeled as a collection of plasma filled flux-tubes. A flux-tube is a volume defined by the magnetic topology such that each flux-tube contains an equal amount of magnetic flux, and magnetic field lines at the surface of the flux-tube align parallel to the surface. The differential flux-tube volume is defined as

$$V \equiv \oint \frac{dl}{B} \tag{2.13}$$

where the integration is along a magnetic field line and B is the magnetic field strength. In the ideal MHD limit the plasma moves with the magnetic field so a rearrangement of the plasma can be viewed as a rearrangement of the flux-tubes. In the dipole geometry the magnetic field strength decreases rapidly as a function of radius ($B \sim 1/R^3$) and the differential flux-tube volume increases rapidly with radius ($V \sim R^4$, since $\oint dl \sim R$). Thus,

as a flux-tube moves radially its volume changes dramatically. This change in volume acts to adiabatically heat or cool the plasma contained within the flux-tube.

The MHD interchange mode is a flute-like ($k_{\|} = 0$) instability. It can be thought of visually as two flux-tubes interchanging positions. The outer flux-tube decreases in volume as it moves in and heats the plasma within it; meanwhile, the inner flux-tube expands as it moves outward and cools the plasma with in it. In their seminal 1957 paper, *Stability of Plasmas Confined by Magnetic Fields*, Rosenbluth and Longmire [7] analyzed the interchange instability from both the particle and MHD perspective. In their MHD analysis they employed the energy principle. This principle states that a system will tend to the lowest potential energy state available to it. In the process of moving to this lower potential energy state the excess potential energy is converted into the kinetic energy of the instability.

Thus, the stability of a plasma to the MHD interchange mode is determined by whether the interchange of two neighboring flux-tubes results in a positive or negative change in energy, ΔE. For $\Delta E > 0$ the plasma is stable, for $\Delta E < 0$ the plasma is unstable, and $\Delta E = 0$ is a marginally stable point. The defining feature of the interchange mode is that there is no change in the magnetic energy during rearrangement of the plasma so only the energy of the plasma is examined. This leads to Rosenbluth and Longmire's result that a plasma is stable to the interchange mode if

$$\Delta E = V^{-\gamma}\,\delta(pV^{\gamma})\,\delta V > 0 \quad . \tag{2.14}$$

For a plasma to be stable the two differential quantities in eq. (2.14) must have the same sign. In their analysis Rosenbluth and Longmire stated that $\delta(pV^{\gamma}) < 0$ since in most plasma devices the pressure decreases away from the central axis (i.e., the pressure gradient

is negative) and goes to zero at the edge ($p \longrightarrow 0$) such that the pressure gradient dominates the flux gradient:

$$\left|\frac{\delta p}{p}\right| > \left|\frac{\gamma \delta V}{V}\right| \quad . \tag{2.15}$$

In this scenario stability requires $\delta V < 0$. This is the basis of the idea of favorable and unfavorable magnetic field curvature in plasma confinement. Favorable curvature has $\delta V < 0$ which corresponds to magnetic field lines that are convex toward the plasma and is generally stable. Unfavorable curvature has $\delta V > 0$ which corresponds to magnetic field lines that are concave toward the plasma and is generally unstable.

Nevertheless, it is possible for a plasma to be stable in regions of unfavorable curvature if the pressure gradient is sufficiently shallow and the magnetic flux gradient is sufficiently steep. That is to say

$$\delta(pV^{\gamma}) > 0 \quad . \tag{2.16}$$

This is fundamental to plasma confinement in a dipole since a dipole has unfavorable curvature in most of the plasma confining volume. In the scenario described by eq. (2.16) the interchange of two flux-tubes requires a net positive change in energy because it takes more energy to heat the inward bound, compressing flux-tube than is released by the outward bound, expanding flux-tube. Thus, the plasma is said to be stabilized by compressibility. The marginal stability point to the MHD interchange mode corresponds to the invariant pressure profile

$$\delta(pV^{\gamma}) = 0 \qquad \Longrightarrow \qquad p \sim R^{-4\gamma} \quad . \tag{2.17}$$

Similar MHD energy principle arguments describe the invariant density profile ($\delta(nV) = 0$) for a plasma rotating in a dipole magnetic field [5].

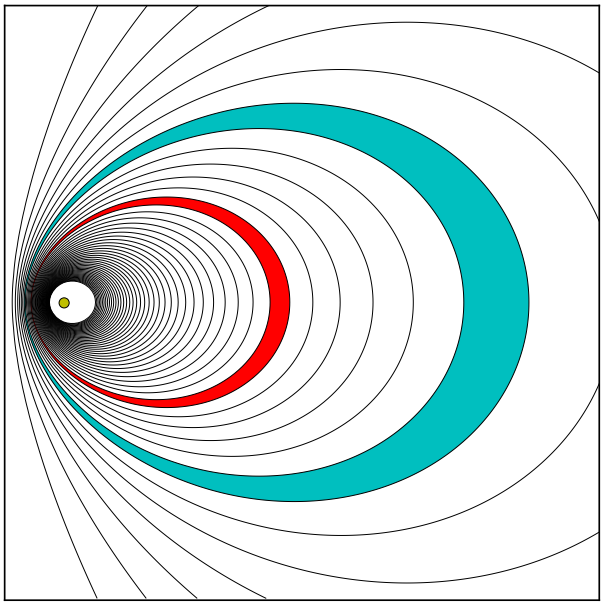

Figure 2.3: Cartoon illustration depicting the interchange of two flux-tubes in the dipole geometry. The contours mark flux surfaces (or equivalently magnetic field lines) and the yellow circle indicates the current location (the system is rotationally symmetric about the left vertical box edge). The red and cyan flux-tubes contain equal amounts of magnetic flux but the cyan flux-tube envelops a much larger physical volume. When the two flux-tubes interchange position the cyan flux-tube decreases in physical volume compressing and heating the plasma within it. Meanwhile the red flux-tube increases in physical volume cooling the plasma within it.

2.2.4 Stability and a tendency toward invariant profiles

The invariant pressure and density profiles describe profiles that are unchanged during interchange motion; however, these stationary profiles are maintained by a turbulent, convective mixing of the plasma. The turbulent mixing is driven by the instability of the plasma profile to the MHD interchange mode and weaker entropy modes [15, 16, 17, 18, 21]. The invariant profiles occur at the marginal stability point to MHD interchange modes but internal plasma heating (by ECRH) continually drives the profiles unstable. Rather than cause a catastrophic loss of the plasma, violations of the MHD limit drive convective cells in the

plasma that bring the plasma back to the invariant profile. Theoretical quasilinear [19] and nonlinear [20] analyses show that a violation of the marginal stability criteria causes convective transport that restores the invariant density and pressure profiles. Random mixing of the plasma flux-tubes leads to profiles that have an equal number of particles per flux-tube and an equal entropy density factor ($G \equiv pV^{\gamma}$) per flux-tube.

Additional theoretical studies have shown that stability to the MHD interchange mode ($k_{\|} = 0$) is sufficient for stability to the MHD ballooning modes ($k_{\|} > 0$) [13, 14]. Studies of drift modes [15, 16, 17, 18] have shown that critical parameter for stability is $\eta \equiv \frac{d\ln T}{d\ln n} = \frac{\nabla T}{T}/\frac{\nabla n}{n}$, and the most stable operating point is $\eta = \gamma - 1 = 2/3$, which combined with eq. (1.1) corresponds to the invariant density and temperature profiles. Gyrokinetic simulations [21] show that entropy-mode driven transport drives the density and pressure toward their invariant profiles ($\eta = 2/3$).

2.2.5 Observations of invariant density profiles on LDX

Previous work by Boxer, et al. [22] has shown that when the superconducting coil is magnetically levitated on LDX the density approaches the invariant profile in which there is an equal number of electrons per flux-tube. This was shown using a four channel interferometer to measure and reconstruct the density profile. The density profiles were observed to exhibit 'profile consistency' [23] meaning the shape of the profiles were consistent for a range of parameters (power, fueling, etc.) although the magnitude of the density varied. The timescale of the formation of the density profiles was found to be consistent with a turbulent inward pinch caused by random electric fluctuations. Random fluctuations in the azimuthal electric field cause the plasma to take random $\mathbf{E} \times \mathbf{B}$ steps in the radial direction. The diffusion coefficient of this process is $D_{\psi\psi} = R^2\langle E_{\phi}^2\rangle\tau_{cor}$ where R is the radial cylindrical coordinate,

$\langle E_\phi^2 \rangle$ is the mean-square of the azimuthal electric field fluctuations, and τ_{cor} is the correlation time of the fluctuations [9]. An array of edge probes measured the azimuthal electric field fluctuations and estimated the diffusion coefficient to be $D_{\psi\psi} \approx 0.047(V \cdot s)^2 s^{-1}$. The time evolution of the density profile obeyed eq. (2.11) with a single diffusion coefficient with the value measured by the edge probes [22]. This low-frequency $\mathbf{E} \times \mathbf{B}$ interchange mixing should also cause diffusion in the entropy density factor ($G \equiv pV^\gamma$), which would produce a peaked, invariant pressure profile.

2.2.6 Supported operation pressure measurements

Previous work on LDX [43, 44] magnetically reconstructed the pressure profile for plasmas when the dipole was mechanically supported. During supported operation the plasma energy is stored entirely in a deeply mirror trapped hot electron population since any thermal population is rapidly lost along the magnetic field to the mechanical supports. Reconstructions determined that the pressure profile was much steeper than the invariant profile. X-ray measurements (see fig. 4.19) observed the pressure to be highly anisotropic, although, the reconstructions were found to be incapable of measuring the level of anisotropy [43]. This work motivated the installation of several internal flux loops that are closer to the plasma in order to better constrain the pressure profile parameters, specifically, the pressure peak location, the pressure profile steepness parameter, and the pressure anisotropy. The work presented in this thesis uses the new flux loops and a new magnetic reconstruction code to confirm the previous results for supported operation and more importantly it magnetically reconstructs the pressure profile during levitated operation.

2.2.7 Challenges to observing invariant pressure profiles on LDX

Plasmas created on LDX typically have a hot electron population in addition to a cooler thermal plasma. The hot electron population forms as a result of the way the plasmas are heated: electron cyclotron resonance heating (ECRH). ECRH transfers energy from an electromagnetic wave to electrons at spatially localized resonance regions in the plasma. The energy transfer increases the electron's velocity perpendicular to the magnetic field. In a magnetic mirror, such as a dipole, increasing the perpendicular velocity of a particle causes it to be more deeply mirror trapped. Hot electron formation is most pronounced when the resonance region is located at the magnetic minimum along a field line because all the particles are heated and the ECRH causes pitch-angle diffusion and anisotropic pressures peaked in the resonance region.

The hot electron population must be taken into account when interpreting the pressure profiles on LDX because hot electron interchange modes can be stable with pressure gradients steeper than the MHD limit that characterizes the predicted invariant pressure profiles of the background plasma. The gyrokinetic stability of the hot electron population is due to its interaction with the background ions. The hot electron modes resonate with the hot electron drift motion with a real frequency $\omega \sim m\,\omega_{dh}$ where m is the azimuthal mode number and ω_{dh} is the drift frequency of the hot electrons. The ions have a much slower drift motion so they observe the mode rapidly pass by them and the rapidly changing electric field associated with the mode induces a stabilizing ion polarization current [45, 46].

For a sufficiently dense hot electron population the low-frequency hot electron interchange (HEI) mode [45, 46, 47, 48, 49, 50, 51] becomes unstable when [2]

$$-\frac{d\ln \bar{n}_{eh}}{d\ln V} > 1 + \frac{m_\perp^2}{24}\frac{\omega_{dh}}{\omega_{ci}}\frac{\bar{n}_i}{\bar{n}_{eh}} \tag{2.18}$$

where $V = \int dl/B$, $\bar{n}_{eh}$ is the flux-tube averaged hot electron density, $\bar{n}_i$ is the flux-tube averaged ion density, $m_\perp$ is total perpendicular mode number [48], ω_{dh} is the hot electron drift frequency, and ω_{ci} is the ion cyclotron frequency. Equation (2.18) shows that the plasma is unstable to the HEI if the spatial gradient of the hot electron density is too large in the region of unfavorable magnetic field curvature. The HEI mode can be stabilized by increasing the right side of eq. (2.18) by either decreasing the hot electron fraction ($\bar{n}_{eh}/\bar{n}_i$) or increasing the hot electron temperature (since $\omega_{dh} \propto T_{eh}$). Both methods of stabilization work by increasing the ion polarization current, which provides a stabilizing current to oppose the perturbed diamagnetic current. Importantly, with sufficient background density the hot electron population can be stable even when the hot electron pressure gradient is much steeper than the MHD limit.

On LDX the hot electron population is very well confined and the hot electrons can have a large energy content. In supported operation essentially all the plasma stored energy is in the hot electrons. One of the primary difficulties in measuring the pressure profile of the thermal plasma during levitation is discerning how much of the plasma energy is stored in the hot electrons and how much is stored in the thermal plasma. Three methods for estimating this are (1) comparing supported and levitated plasmas, (2) measuring the decay times of the stored energy [26], and (3) measuring the X-ray emission.

Chapter 3

Overview of the Levitated Dipole Experiment

3.1 Experimental setup

The Levitated Dipole Experiment magnetically levitates a superconducting current ring, which has been energized to 1.2 MA, in a large vacuum chamber.

The basic experiment setup is illustrated in fig. 3.1. The magnetic coil set consists of three coils: the floating coil (F-coil), the levitation coil (L-coil), and the charging coil (C-coil). The F-coil is the coil that is levitated in the middle of the vacuum chamber and produces the dipole magnetic field that confines the plasma. It is a superconducting coil made from single strand of Nb^3Sn with 716 turns and is housed in a cryostat that levitates with it in the vacuum chamber [1]. The F-coil typically operates with a total current of 1.2 MA·turns and is inductively charged by the C-coil. This is done by putting the F-coil inside the C-coil while the F-coil is warm and is not in its superconducting state. The C-coil

current is ramped up then held steady. This induces a current in the F-coil but the current is rapidly lost via resistive heating. The F-coil is then cooled to its superconducting state. The current in the C-coil is ramped down to zero. This again induces a current in the F-coil but the current stays since the F-coil is now superconducting. The F-coil is mechanically lifted in the center of the vacuum chamber where it can be magnetically levitated by the L-coil. The L-coil is made from a copper wire with 80 turns, typically carries $\sim$ 3500 A (280 kA·turns), and sits on top of the vacuum vessel approximately 1.5 meters above the middle of the vacuum vessel where the F-coil is positioned.

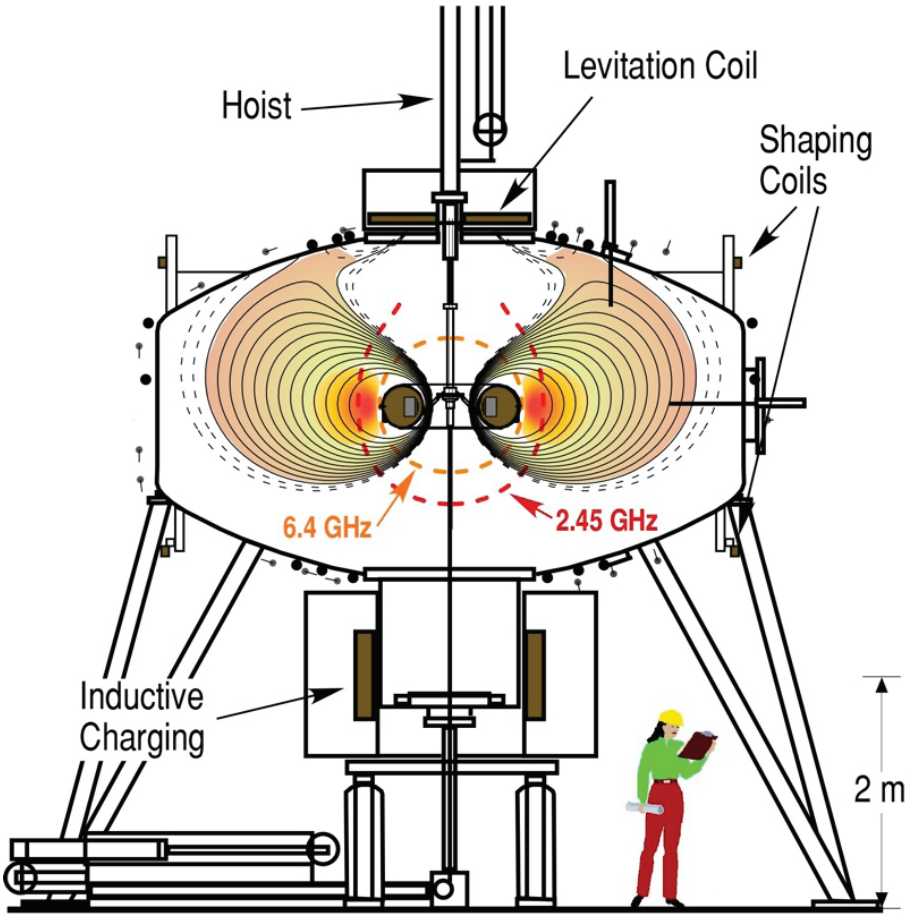

Figure 3.1: The LDX vacuum chamber and magnetic coil set.

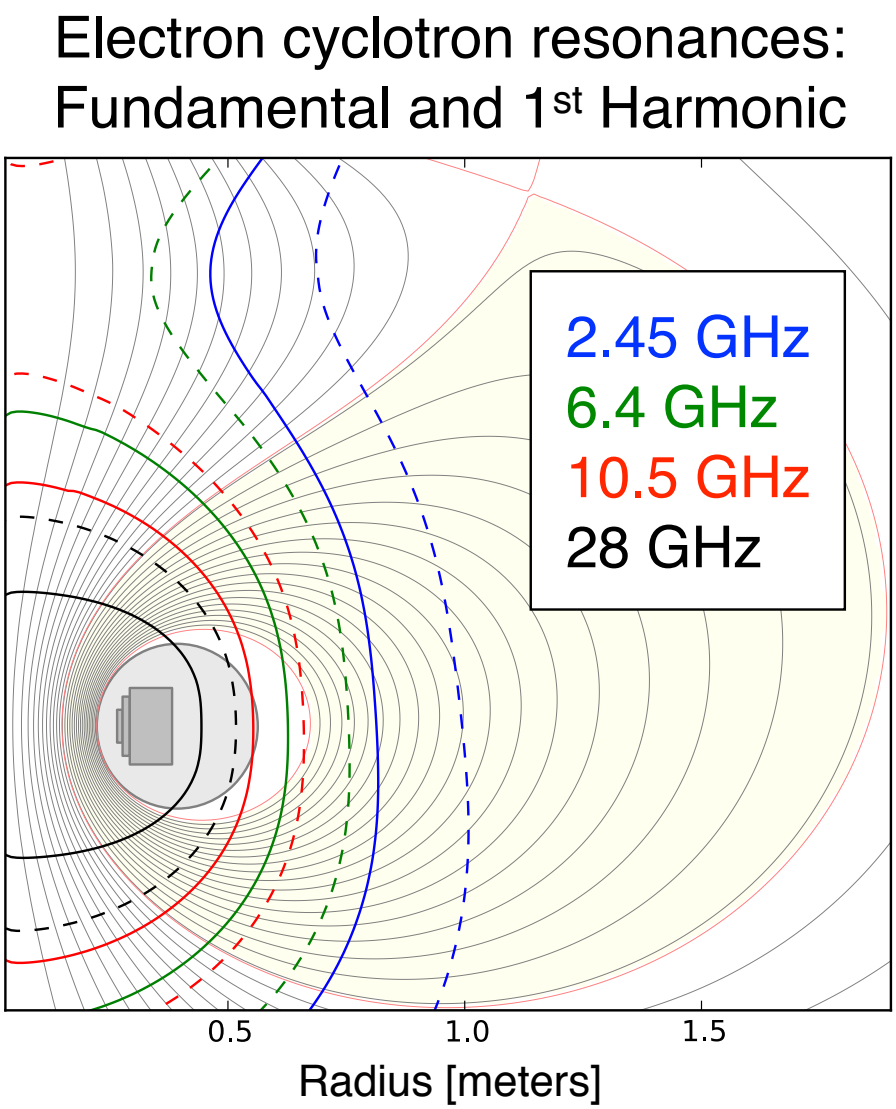

Figure 3.2: Locations of the fundamental and 1^{st} harmonic electron cyclotron resonances for the microwave heating sources on LDX. Solid lines mark the fundamental resonances and dashed lines mark 1^{st} harmonic resonances.

3.2 Creation of the plasmas

Plasmas on LDX are created and heated with electron cyclotron resonance heating (ECRH).

An electron in a magnetic field gyrates at the electron cyclotron frequency. When a wave

with a frequency resonant with the electron's cyclotron motion interacts with the electron, energy can be transferred between the wave and the electron. Because the cyclotron frequency depends only on the magnetic field strength and fundamental constants (electron mass and charge) the spatial region where the wave can deposit energy into the electron population is determined by the magnetic topology.

LDX has 5 ECRH sources at 4 different frequencies that provide a total of 28 kW of microwave power. There are 2 sources at 2.45 GHz (2 kW and 3 kW), 1 source at 6.4 GHz (3 kW), 1 source at 10.5 GHz (10 kW), and 1 source at 28 GHz (10 kW). Experiments begin by puffing a small amount of neutral gas (typically deuterium or helium) into the vacuum chamber. Then the ECRH is turned on. The small population of free electrons in the puffed gas gains energy from the ECRH and ionizes much of the remaining gas through collisions. The process of creating, sustaining, and dissipating a plasma is called an experimental shot. Shots on LDX are pre-programmed to have a duration between 10-20 seconds.

3.3 Diagnostics

Table 3.1 provides a summary of the diagnostics on LDX. Figure 3.3 provides a cartoon depiction of the approximate locations and views of a subset of the LDX diagnostic set. The diagnostics used principally in this thesis are the magnetic flux loops, poloidal field coils, and X-ray light detectors. These diagnostics are more completely discussed in the following sections.

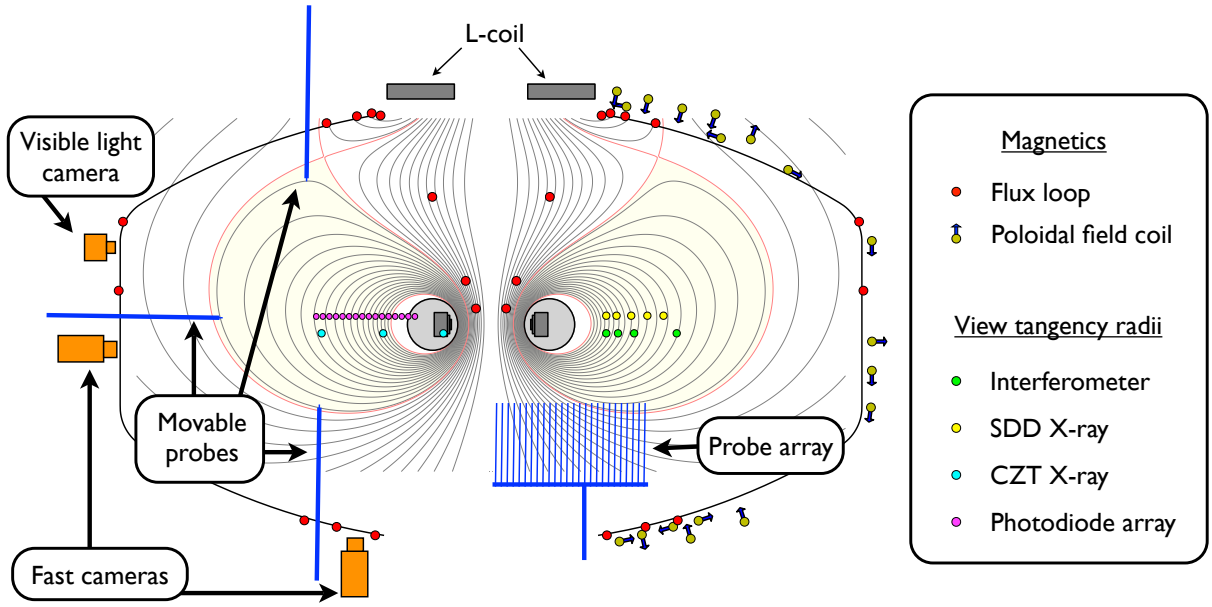

Figure 3.3: A cartoon overview of a subset of the LDX diagnostic set.

Magnetics	Description
Flux loops	9 external, 4 internal, integrated change in flux
Poloidal field coils	18 external, integrated change in flux
Hall sensors	18 external, field strength
Mirnov coils	8 internal, change in flux

X-ray light detectors	Description
Silicon drift detector (SDD)	2-20 keV, photon counting
Cadmium-Zinc-Telluride (CZT) detector	10-650 keV, photon counting
Sodium Iodide (NaI) detector	15 keV - 3 MeV, integrated intensity

Microwave light detectors	Description
Interferometer	4 chords, 60 GHz, density measurement
V-band radiometer	50-75 GHz, electron cyclotron emission (ECE)

Visible light detectors	Description
Visible light camera	
Spectrometer	340-550 nm, 0.3 nm resolution
Photodiodes	with atomic line emission filters
Visible light fast cameras	up to 40,000 frames per second

Probes	Description
Probe array	24 probes spanning $\pi/2$ azimuthally, floating and ion saturation
Movable probes	3 probes, operate as either swept-voltage, floating-voltage, or ion saturation probes

Other	Description
Vessel ion gauge	1-100 AMU, gas pressure

Table 3.1: Summary of the diagnostics on LDX.

3.3.1 Magnetics

There are 27 magnetic sensors used to reconstruct the plasma pressure profiles: 12 flux loops and 15 poloidal field coils. Both types of sensors are essentially loops of wire that measure changes in the magnetic field. From Faraday's law the time rate of change of the magnetic field inside a wire loop induces a voltage at the ends of the loop:

$$V_{loop} = \int \frac{\partial \mathbf{B}}{\partial t} \cdot d\mathbf{A} \tag{3.1}$$

where V_{loop} is the voltage at the end of the wire loop, $\frac{\partial \mathbf{B}}{\partial t}$ is the time rate of change of the magnetic field, and the integration is over the area enclosed by the wire loop.

For the poloidal field coils the enclosed area is small enough that the magnetic field is approximately constant over area of integration so eq. (3.1) can be approximated as

$$V_{loop} = \frac{\partial B}{\partial t} NA \tag{3.2}$$

where B is the magnitude of the magnetic field normal to the integration surface, A is the area enclosed by the loop, and N is the number of windings (loops).

For the flux loops the magnetic field cannot be assumed constant over the integration surface; however, eq. (3.1) can be rewritten in terms of the magnetic flux,

$$V_{loop} = \frac{\partial}{\partial t} \int \mathbf{B} \cdot d\mathbf{A} = \frac{\partial \psi_p}{\partial t} \tag{3.3}$$

where the normal vector of the area enclosed by the loop is taken to be in the z-direction so the enclosed flux can be written as the enclosed poloidal flux, ψ_p.

The flux loop and poloidal field coil loop voltages are proportional to the time rate of

change of the magnetic flux and the magnetic field strength, respectively. For the magnetic reconstruction of the equilibrium pressure profile the quantities of interest are the magnetic flux and the magnetic field strength so the loop voltages are integrated over time. The loop voltages are integrated with active analog integration circuits [43]. The output voltage from the integration circuit is

$$V_{out} = -\frac{1}{RC}\int V_{loop}\, dt \tag{3.4}$$

where R and C are the resistance and capacitance that characterize the integrator (the integrator time constant: $\tau = RC$).

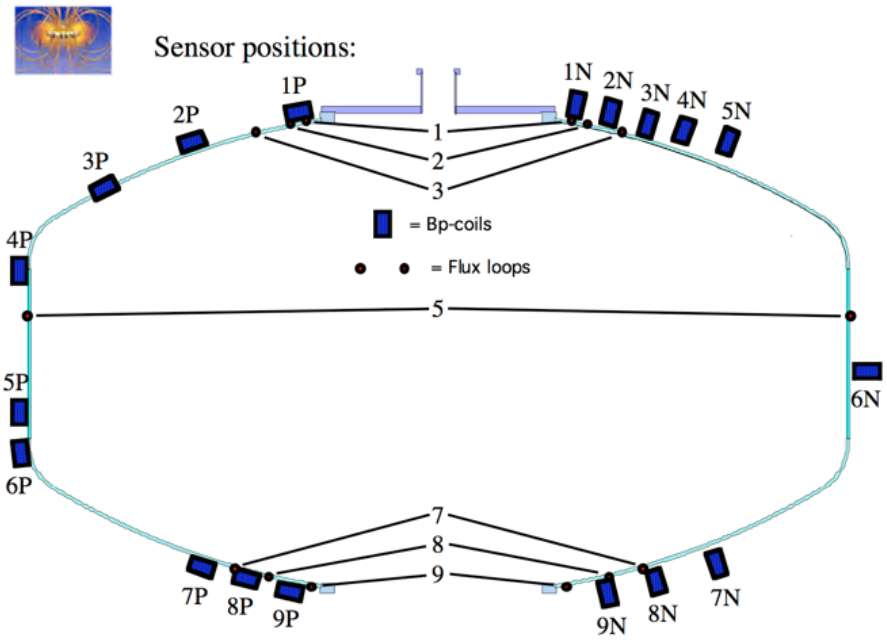

(a)

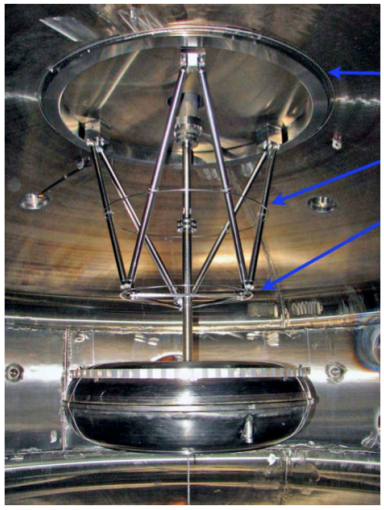

(b)

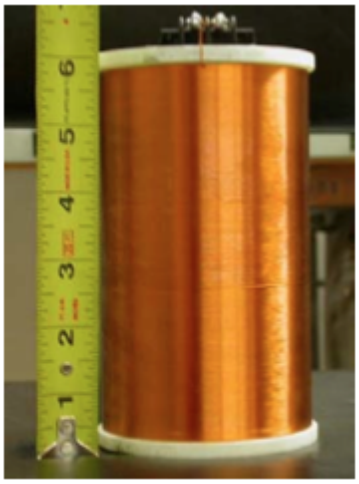

(c)

Figure 3.4: Sensor locations and images [43]. (a) Poloidal field coil and external flux loops locations. Illustration shows poloidal field coils at different azimuthal locations for aesthetic reasons; however, all poloidal field coils are actually located at the same azimuthal angle. (b) Picture of the internal flux loops located on the upper catcher structure. (c) Picture showing the size of a poloidal field coil.

3.3.2 X-ray detectors

Silicon Drift Detector (SDD)

The SDD measures soft X-rays in the energy range 1-20 keV. The detector used is the XR-100SDD with a 0.5 mil beryllium window and is manufactured by Amptek [52]. The detector is installed in vacuum on a port with a flexible baffle that allows the detector's view to be adjusted. The detector views at the mid-plane with different tangency radii, where the tangency radius is the shortest distance between the central view chord and the center of the vacuum chamber. Five view positions were used with tangency radii 77 cm, 83 cm, 93 cm, 105 cm, and 116 cm. Photon flux to the detector is restricted by a tungsten disk with a 60 mil diameter pinhole (disk is 1 inch in diameter and 40 mil thick). The detector's distance behind the pinhole determines the photon fluence to the detector and the detector view angle. The view angle of the detector was about 10° so there is considerable overlap between the five different views. Figures 3.5(a) and 3.5(b) show the detector and the detector installed in vacuum. Figures 3.6(a) and 3.6(b) show the detector's central view lines and the detector's efficiency at detecting X-ray photons of different energies.

(a)

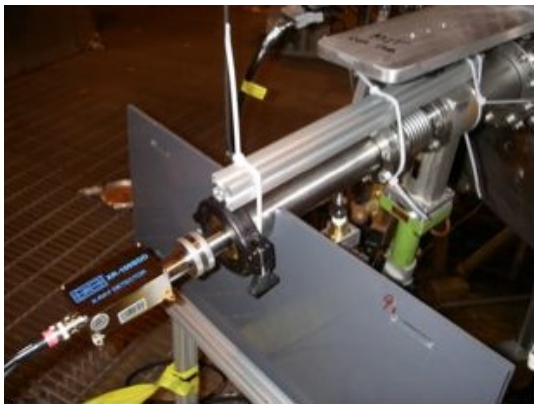

(b)

Figure 3.5: (a) The SDD X-ray detector. (b) The SDD X-ray detector mounted on a vacuum port on LDX. The flexible bellows allows the detector to be pointed at different radial positions.

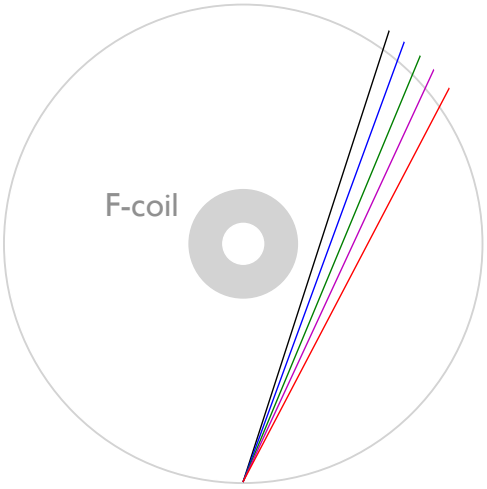

(a)

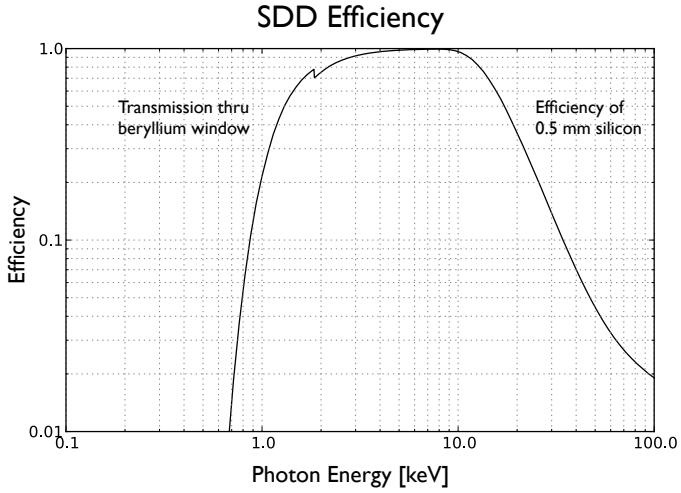

(b)

Figure 3.6: (a) Views lines for the SDD. (b) Detection efficiency for the SDD. At low energies the beryllium window blocks photons. High energy photons pass through the thin detector.

Cadmium-Zinc-Telluride detectors (CZT)

The CZT detectors measure X-rays in the energy range 10-650 keV. The present data system allows for 3 CZT detectors to be operated in addition to the SDD. The detectors view at the mid-plane with tangency radii 30 cm, 72 cm, and 113 cm. In the experiment X-rays have to pass through a 0.005" (127 μm) beryllium vacuum window, an air gap, and the detector window which is 0.001" (25.4 μm) aluminum and 0.0005" (12.5 μm) stainless steel. The CZT crystal is 5x5x5 mm with a density of 5.8 g/cm^{3}and the relative composition 9 Cd, 1 Zn, 10 Te [53]. Figures 3.7(a) and 3.7(b) show the detectors' central view lines and the detectors' efficiency at detecting X-ray photons of different energies.

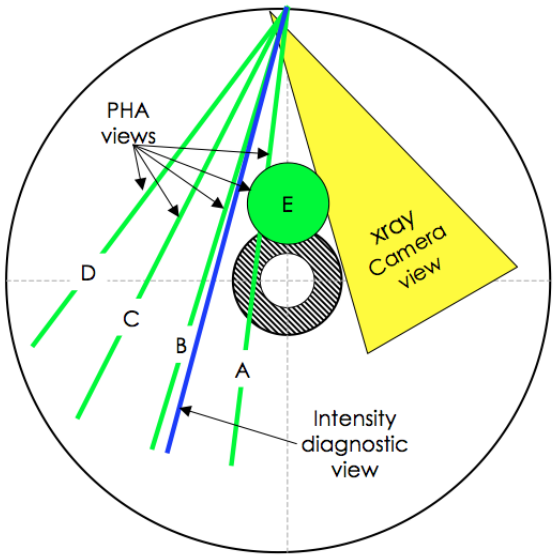

(a)

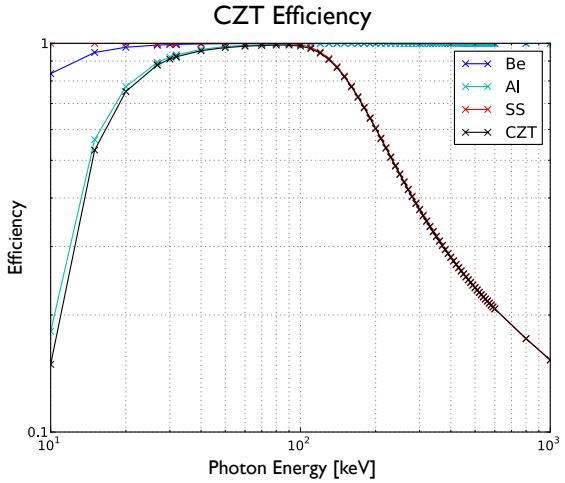

(b)

Figure 3.7: (a) Views lines for the CZT detectors [54]. Detector's had views A, B, and C. (b) Detection efficiency for the CZT detectors [53].

Pulse counting

The SDD and CZT detectors are pulse counting devices meaning that they count individual photons. A photon incident on the detector causes the voltage at the detector's preamplifier

to increase by an amount proportional to the energy of the photon. The SDD has a reset preamplifier. Thus as photons hit the detector the signal at the reset preamplifier increases like a staircase but with steps of many different sizes. Once the reset preamplifier reaches its maximum voltage it abruptly resets to its minimum value. By contrast the CZT detectors have resistive-feedback preamplifiers which have characteristic decay times that prevent the preamplifier voltage from reaching its maximum so long as the detector is not saturated by photons.

The task of pulse counting is simply to bin the voltage steps according to size. One method for performing the pulse counting is done with a pulse shaper and Multi-Channel Analyzer (MCA), which is a programmable electronic device that counts pulses while doing its best to avoid potential pitfalls (i.e., pulse pile-up). The disadvantage of this method is that preamplifier signal is never seen, only the processed data is recorded. Concerns about the detector performance in the LDX environment based on previous X-ray measurements [53] made it desirable to use an alternative pulse counting method that allowed the detector preamplifier signal to be recorded and perform the pulse counting as a post-process. A fast digitizer board was acquired that can digitize 4 channels at 50 Msps (or 8 channels at 25 Msps, or 16 channels at 15 Msps). This board allows the preamplifier signal to be seen; however, to achieve sufficient energy resolution with the digitizer the signal was passed through another preamplifier before being digitized.

Preamplifier board

The purpose of the preamplifier board is to increase the energy resolution of the digitized signal. The signal from the SDD reset preamplifier is approximately 1 mV/keV. The digitizer is 14-bit and has a minimum dynamic range of $\pm$ 2.5 V. Thus directly digitizing the

signal from the reset preamplifier would result in very poor energy resolution ($\sim 300\ eV$). The preamplifier board acts as a high-pass filter and amplifier that transforms the reset preamplifier's staircase signal into a series of pulses with a characteristic decay time. The signal from the preamplifier board is digitized and stored for post-processing (pulse shaping and counting).

The preamplifier board design is based closely on the first stage (the analog prefilter) of the Amptek DP5 board [55]. The preamplifier is integrated into the DP5 board, which does complete digital signal processing, and could not be purchased separately from Amptek. Figure B.1 shows a schematic of the preamplifier that was built for use on LDX with both the SDD and CZT X-ray detectors. There are 5 stages: a buffer isolates the board from the input, a high-pass filter transforms the input signal, two stages of amplification increase the signal strength, and a low-pass filter removes noise from the signal and provides power to send the signal to the digitizer. Additional resistors in the high-pass stage allow the board to be adapted for use with either the SDD (reset preamplifier) or the CZT detectors (resistive feedback preamplifier). The output of the preamplifier board is a pulse with a fast rise time and a slower exponential decay. The decay time of the output pulse is $3.2\,\mu s$.

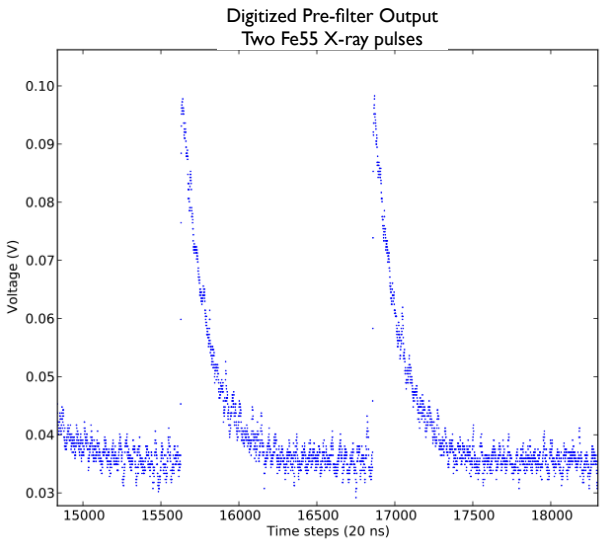

Figure 3.8: Preamplifier board output showing the pulses caused by two Fe^{55} photons.

Pulse shaping

Pulse shaping is done as a post-process of the digitized preamplifier data. Pulses from the preamplifier are shaped into trapezoidal pulses [56, 57]. Characteristics of the trapezoidal pulse (rise time, flat top time) are parameters of the shaping algorithm. Figure 3.9 illustrates a preamplifier pulse shaped into both a short and long trapezoidal pulse.

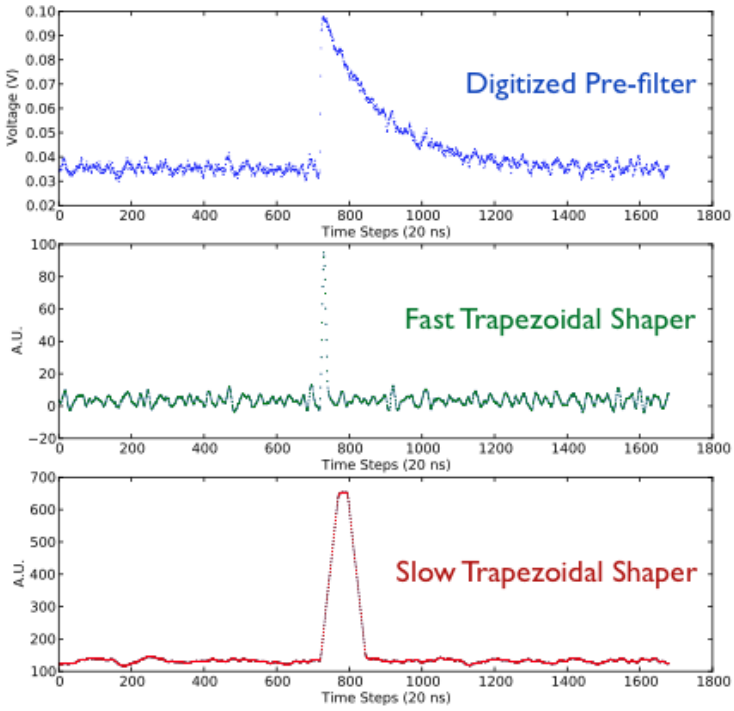

Figure 3.9: Pulses from the preamplifier board can be shaped into both short and long trapezoidal pulses.

Pile-up rejection

Pile-up refers to multiple photons entering the detector at nearly the same time causing errors in the measurement. For example, if two low energy photons hit the detector too close in time the shaping and counting algorithms may misinterpret the two photons as a single higher energy photon. This can cause distortions in the measured spectra. To avoid errors due to pile-up, photon counting algorithms are designed to recognize when pile-up may be occurring and reject data collected during that time. This is called pile-up rejection. It results in some data being thrown away on the assumption that it is better to have some data that can be trusted than a lot of data that cannot. If the flux of photons to the detector is too high pile-up rejection can result in all the data being rejected so it is important to

limit the photon flux to a rate the system can handle.

Limitations to the maximum input rate is a common feature of pulse counting systems. A classical example of a pulse counting system being overloaded occurred during the discovery of the Van Allen radiation belts by the *Explorer I* and *Explorer III* satellite missions. Geiger counters installed on the satellites measured times with zero counts surrounded by times with high count rates. It was discovered that the zero count times corresponded to times when the Geiger tubes were being saturated by a high flux of radiation [58, 59]. These regions of high radiation became known as the Van Allen radiation belts.

The pile-up rejection algorithm that is implemented with the SDD and CZT detectors uses both a fast (short) and a slow (long) trapezoidal shaping of the input pulses. There is a tradeoff when performing the trapezoidal shaping. Long trapezoidal pulses offer better energy resolution but are more likely to overlap in time with other long pulses than are shorter pulses. The pile-up rejection algorithm uses fast pulses to determine the pulse arrival times and determine if a pulse is isolated enough in time to be cleanly counted. Pulses that have been deemed countable by the fast shaping have their energy calculated from the slow shaping.

To summarize the pulse counting process: a photon enters detector, the voltage at the detector preamplifier increases a step proportional to the photon energy, the step is shaped into a pulse by another preamplifier board, the signal is digitized, post-processing performs trapezoidal shaping, pile-up rejection and sorting of pulses by energy to form a spectrum.

Calibration

The SDD and CZT spectra are calibrated using the iron radionuclide Fe^{55} and the americium radionuclide Am^{241}. Table 3.2 lists the atomic transitions for the lines used in the calibration

[60].

Radionuclide	Energy [keV]
Fe^{55}	5.90
Fe^{55}	6.50
Am^{241}	7.48
Am^{241}	8.26
Am^{241}	11.87
Am^{241}	13.94
Am^{241}	16.11
Am^{241}	17.06
Am^{241}	17.75
Am^{241}	20.83
Am^{241}	21.51
Am^{241}	59.54

Table 3.2: X-ray lines used for calibrating the SDD and CZT detectors.

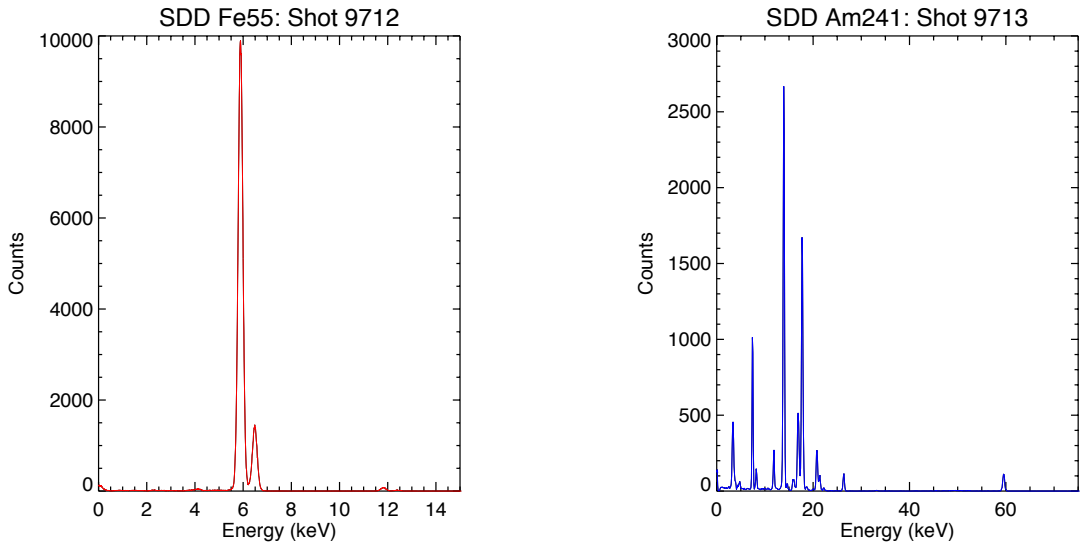

(a) (b)

Figure 3.10: SDD calibration spectrum with (a) Fe^{55} and (b) Am^{241}.

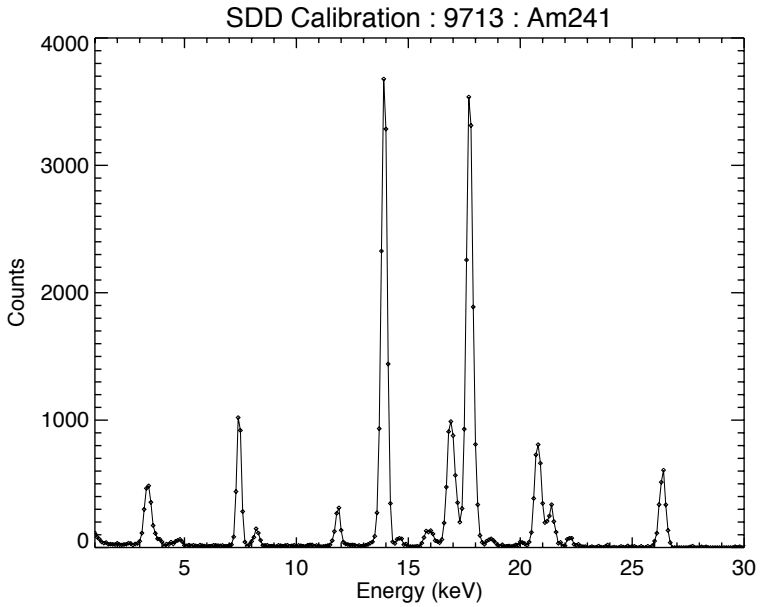

Figure 3.11: Zoomed view of the lower energy SDD spectrum with Am^{241}.

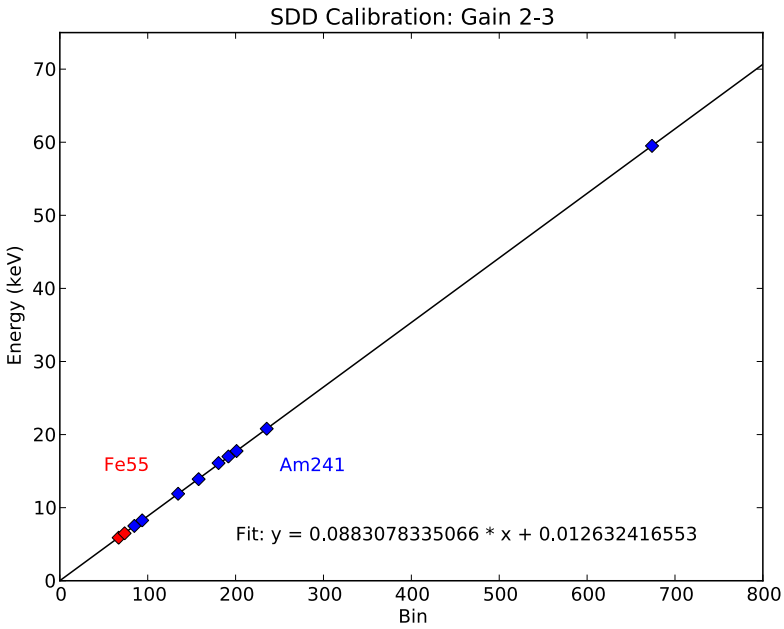

Figure 3.12: SDD calibration line from least squares fit to observed lines from Am^{241} and Fe^{55}.

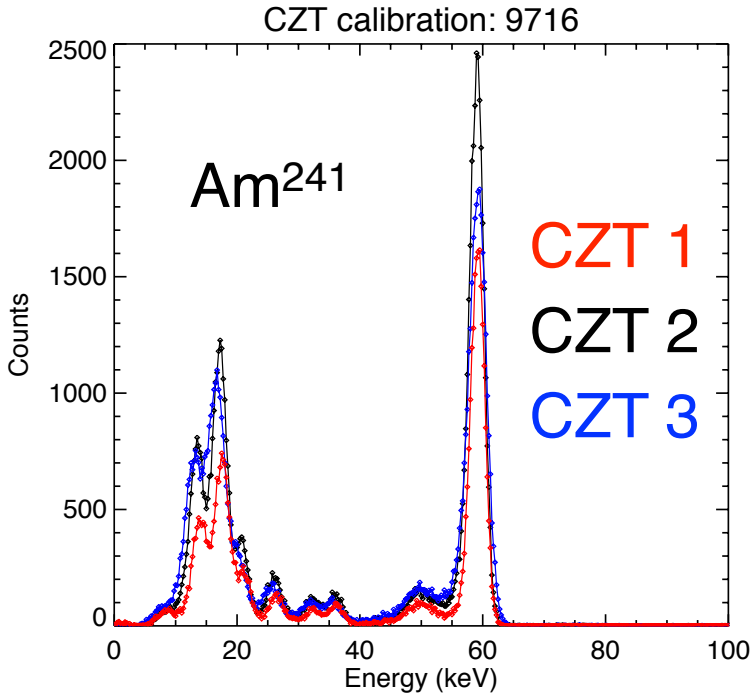

Figure 3.13: CZT detector calibration spectrum with Am^{241}.

Chapter 4

Magnetic reconstructions: Method

In an equilibrium state there is no net force, which is to say all forces balance. For a plasma in magnetohydrodynamic equilibrium the forces that balance are the force from the pressure gradient, ∇P, and the $\mathbf{j} \times \mathbf{B}$ force [38, 61]. Thus, if the current density, $\mathbf{j}$, and magnetic field, $\mathbf{B}$, are known throughout a plasma in equilibrium, then the gradients of the pressure throughout the plasma are also known. With knowledge of the plasma boundary conditions (i.e., the pressure goes to zero at the plasma edge) the pressure profile of the plasma can be deduced.

Magnetic reconstruction of the pressure profile on LDX is an inverse problem. Measurements of the magnetic field outside of the plasma are used to deduce the currents and magnetic field inside of the plasma [24, 25, 62, 63]. This chapter discusses how measurements of the magnetic field are used to perform a model-based reconstruction of the pressure profile on LDX.

4.1 Magnetohydrodynamic equilibrium

Magnetohydrodynamic equilibrium is defined by the relation:

$$\nabla P = \mathbf{J} \times \mathbf{B} \tag{4.1}$$

where P is the plasma pressure, $\mathbf{J}$ is the current density and $\mathbf{B}$ is the magnetic field. In this definition the pressure is isotropic; however, a more general form may be used:

$$\nabla \cdot \bar{\mathbf{P}} = \mathbf{J} \times \mathbf{B} \tag{4.2}$$

where $\bar{\mathbf{P}}$ is the pressure tensor. In LDX plasmas there is often a pressure anisotropy because the plasma is heated with ECRH and is deeply mirror trapped. The pressure tensor may be represented as

$$\bar{\mathbf{P}} = \begin{bmatrix} P_\perp & 0 & 0 \\ 0 & P_\perp & 0 \\ 0 & 0 & P_\parallel \end{bmatrix} = P_\perp \bar{\mathbf{I}} + (P_\parallel - P_\perp)\hat{\mathbf{b}}\hat{\mathbf{b}} \tag{4.3}$$

where $P_\perp$ and $P_\parallel$ denote the perpendicular and parallel pressure components, respectively, $\bar{\mathbf{I}}$ is the identity matrix, and $\hat{\mathbf{b}}$ is a unit vector along the magnetic field ($\mathbf{B} = B\hat{\mathbf{b}}$). The degree of anisotropy on LDX is likely limited by stability to mirror modes [64].

4.1.1 Grad-Shafranov equation

In many plasma experiments, including LDX, the plasma can be approximated as being azimuthally symmetric. Using this assumption of azimuthal symmetry as well as two constraints regarding the behavior of currents and magnetic fields (Ampere's Law and the

$\nabla \cdot \mathbf{B} = \mathbf{0}$ law) eq. (4.1) can be rewritten as a partial differential equation named the Grad-Shafranov equation [61]:

$$\Delta^* \psi = -\mu_o R^2 \frac{\partial P}{\partial \psi} - F \frac{\partial F}{\partial \psi} \tag{4.4}$$

where Δ^* is an elliptic operator defined by

$$\Delta^* \psi \equiv R^2 \nabla \cdot \left(\frac{\nabla \psi}{R^2} \right) = R \frac{\partial}{\partial R} \left(\frac{1}{R} \frac{\partial \psi}{\partial R} \right) + \frac{\partial^2 \psi}{\partial Z^2} \quad . \tag{4.5}$$

As eq. (4.4) looks little like eq. (4.1) some explanation is in order. This explanation is important because the Grad-Shafranov equation represents the condition of radial force balance and is at the heart of the magnetic reconstruction.

First note that eq. (4.4) is a function of the variable ψ, which is defined $\psi = RA_\phi$, where R is the radial coordinate in a cylindrical coordinate system, (R, ϕ, Z), and A_ϕ is the toroidal component of the vector potential. A more intuitive sense of the variable ψ can be found from its close relation to the poloidal flux, ψ_p, passing through a circular disk aligned normal to the Z direction, specifically $\psi_p = 2\pi\psi$ [61]. Thus, ψ is a magnetic flux coordinate and, as such, labels surfaces of constant magnetic flux.

$P(\psi)$ and $F(\psi)$ are flux functions, meaning they have constant values on flux surfaces. The function $P(\psi)$ is the pressure seen in eq. (4.1). The function F is defined $F = RB_\phi$. On LDX there is no toroidal component to the magnetic field ($B_\phi = 0$) so $F = 0$. Thus, the second term on the right of eq. (4.4) can be eliminated:

$$\Delta^* \psi = -\mu_o R^2 \frac{\partial P}{\partial \psi} \quad . \tag{4.6}$$

Equation (4.6) can also be written in terms of the toroidal current density:

$$\Delta^* \psi = -\mu_o R J_\phi \tag{4.7}$$

$$J_\phi = R \frac{\partial P}{\partial \psi} \quad . \tag{4.8}$$

4.1.2 Magnetic field of a current loop

The azimuthal symmetry of LDX allows currents in the machine to be modeled as a collection of circular current loops. The analytic form of the magnetic field of a current loop is written down here because of its ubiquity in calculating mutual inductances, boundary conditions for magnetic reconstructions, and magnetic flux and field values on LDX. The analytic form is expressed in terms of elliptic functions of the first and second kind

$$K(k) = \int_0^{\pi/2} \left(1 - k^2 \sin^2 y\right)^{1/2} dy \tag{4.9}$$

$$E(k) = \int_0^{\pi/2} \frac{dy}{\left(1 - k^2 \sin^2 y\right)^{1/2}} \quad . \tag{4.10}$$

The derivatives of the elliptical functions are:

$$\frac{dK(k)}{dk} = \frac{E(k)}{k(1-k^2)} - \frac{K(k)}{k} \tag{4.11}$$

$$\frac{dE(k)}{dk} = \frac{E(k) - K(k)}{k} \quad . \tag{4.12}$$

The vector potential in cylindrical coordinates, (R, ϕ, Z), for a circular loop of current with radius a, height h, and current I is

$$A_\phi = \frac{\mu_o I}{2\pi k} \sqrt{\frac{a}{R}} \left[(2 - k^2) K(k) - 2E(k) \right] \tag{4.13}$$

where

$$k^2 = \frac{4aR}{(R+a)^2 + (Z-h)^2} \tag{4.14}$$

and μ_o is the permeability of free space. The magnetic field has only an R and Z component

$$B_R = -\frac{\partial A_\phi}{\partial Z} = -\frac{\mu_o I k (Z-h)}{4\pi\sqrt{aR^3}}\left[K - \frac{2-k^2}{2(1-k^2)}E\right] \tag{4.15}$$

$$B_Z = \frac{\partial (RA_\phi)}{R\partial R} = \left(\frac{\mu_o I k}{4\pi\sqrt{aR}}\right)\left[K + E\left(\frac{k^2(R+a) - 2R}{2R(1-k^2)}\right)\right] \quad . \tag{4.16}$$

4.2 Errors in the magnetics measurements

There are two primary sources of error in the magnetics measurements: uncertainty from the sensor properties, such as the electronic gain from the integrator, and the physical location of the sensors. From eqs. (3.2) to (3.4) the poloidal field and flux loop measurements can be expressed as

$$\Delta B = \frac{\tau\, V_{out}}{NA} \tag{4.17}$$

$$\Delta\psi = \tau\, V_{out} \quad . \tag{4.18}$$

Thus, the errors in the measurements due to uncertainty about the sensors can be approximated as

$$\sigma_{\Delta B,s} \approx \sqrt{\frac{\tau^2}{(NA)^2}\sigma^2_{V_{out}} + \frac{V^2_{out}}{(NA)^2}\sigma^2_\tau + \frac{\tau^2\, V^2_{out}}{(NA)^4}\sigma^2_{NA}} \tag{4.19}$$

$$\sigma_{\Delta\psi,s} \approx \sqrt{\tau^2\, \sigma^2_{V_{out}} + V^2_{out}\, \sigma^2_\tau} \quad . \tag{4.20}$$

The errors in the measurement due to uncertainty about the location of the sensors can be approximated as

$$\sigma_{\Delta B,p} \approx \sqrt{\frac{\partial B}{\partial R}\sigma^2_{R_0} + \frac{\partial B}{\partial Z}\sigma^2_{Z_0} + \frac{\partial B}{\partial \Theta}\sigma^2_{\theta_0}} \tag{4.21}$$

$$\sigma_{\Delta \psi,p} \approx \sqrt{\frac{\partial \psi}{\partial R}\sigma^2_{R_0} + \frac{\partial \psi}{\partial Z}\sigma^2_{Z_0}} \quad . \tag{4.22}$$

The total uncertainty of the measurements is then

$$\sigma_{\Delta B} \approx \sqrt{\sigma^2_{\Delta B,s} + \sigma^2_{\Delta B,p}} \tag{4.23}$$

$$\sigma_{\Delta \psi} \approx \sqrt{\sigma^2_{\Delta \psi,s} + \sigma^2_{\Delta \psi,p}} \quad . \tag{4.24}$$

Table 4.1 summarizes the magnitudes and sources of the uncertainties that go into eqs. (4.23) and (4.24). A more complete inventory of the errors in each sensor is listed in Appendix A. The measurement error is calculated for each shot.

Error	Magnitude	Source of error
$\sigma_{V_{out}}$	0.2 mV	digitizer resolution
σ_τ	$\sim 2\%$ of τ	uncertainty in time constant, estimated from "copper plasma" calibration shots
σ_{NA}	$\sim 0.02\, m^2$	measurement of B_p coil dimensions
σ_{R_0}	3 mm	uncertainty in measurement of sensor location
σ_{Z_0}	3 mm	uncertainty in measurement of sensor location
σ_{Θ_0}	1°	uncertainty in measurement of sensor location

Table 4.1: Summary of magnitudes and sources of magnetic measurement errors. A more complete inventory of the errors in each sensor is listed in Appendix A.

4.3 Calibration with 'copper plasma'

In the summer of 2009 visiting graduate student Dennis Boyle attempted to reduce the measurement errors on the positions and gains of the magnetic sensors by using a copper coil installed inside the LDX vacuum vessel [65]. The calibration shots performed with this copper coil are referred to as the 'copper plasma'. To be clear, the 'copper plasma' shots are not plasma shots; they are shots taken with a copper coil positioned at the approximate location where the plasma ring current is during LDX plasma shots.

For the work done in this thesis, the 'copper plasma' was used to calibrate the gains of the magnetic measurements and estimate the measurement errors. The calibration used 36 shots with the coil in 6 different positions (R ={0.762 m, 0.915 m}, Z={-0.06 m, 0.00 m, +0.05 m} where the positions are relative to the vacuum vessel center) and with the current run in both polarities. Most magnetic measurements agreed with the calculated values to within 1-2% for all the shots. This is illustrated in figs. 4.2(a) and 4.2(b).

In addition to calibrating the magnetic measurements, the 'copper plasma' provides the opportunity for verification of some of the code that is used in the magnetic reconstructions of plasma shots. This includes verification of the code's basic calculations, models and minimization algorithms used to find best fits to the magnetics data. Figure 4.3(a) shows that the χ^2 minimization algorithm works well at determining the location and magnitude of the current ring in the simple case of the 'copper plasma'.

Figure 4.1: Rick Lations and Darren Garnier install the 'copper plasma' for calibrations. The 76 cm and 92 cm coils can be seen in green and red, respectively.

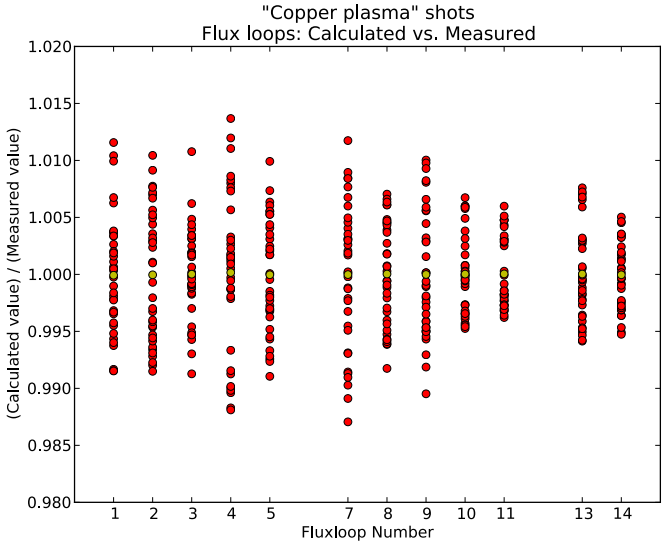

(a)

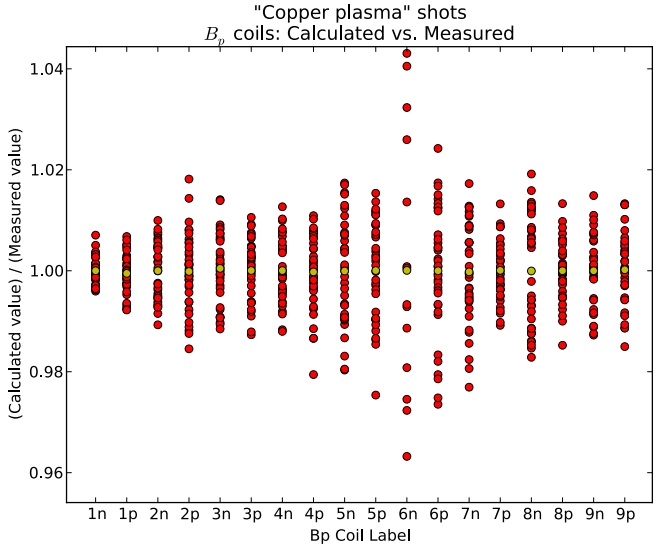

(b)

Figure 4.2: Using 36 calibration shots with the 'copper plasma' in 6 different positions (2 radial, 3 vertical) the magnetic flux loops and poloidal field coils were calibrated and the errors in the measurements estimated. The ratio of the calculated value of the measurement to the measurement for (a) the flux loops and (b) the poloidal field coils. For the 'copper plasma' the measured valued was with in 1-2% for almost all the magnetic sensors. The large variation in B_p coil 6N is simply due to the very small signal that the coil observes in this current configuration.

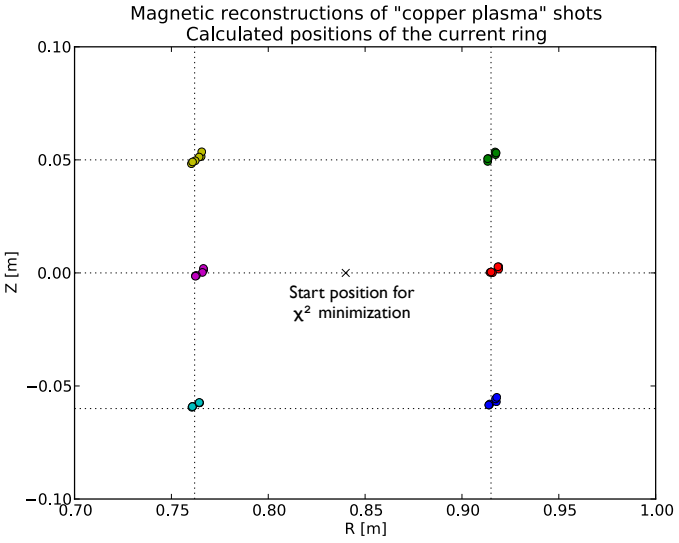

(a)

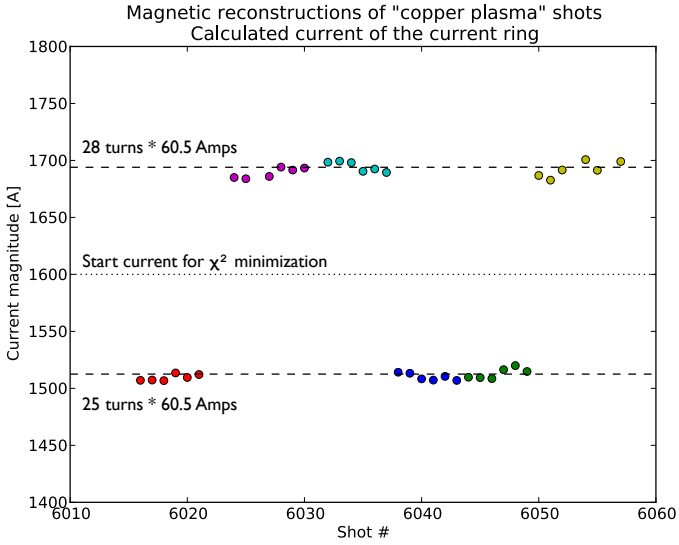

(b)

Figure 4.3: The position and magnitude of the 'copper plasma' ring current for 36 different shots found via a χ^2 minimization with 3 free parameters: radial location (R), vertical position (Z), and current (I). (a) Locations of the current ring. The approximate measured positions of the 'copper plasma' coil are indicated by the intersections of the dotted lines (R ={0.762 m, 0.915 m}, Z={-0.06 m, 0.00 m, +0.05 m} where the positions are relative to the vacuum vessel center). The start location of the minimizations is marked by an 'x' located at [0.84, 0.0]. (b) Magnitude of the ring current. The approximate measured current for the 25 turn setup (1512 A) and the 28 turn setup (1694 A) are shown by the dashed lines. The start current for the minimizations is marked by the dotted line at 1600 A.

4.4 Vacuum magnetic reconstructions

Vacuum magnetic shots provide another verification of the models and code that are used in the magnetic reconstructions. There are two types of vacuum magnetic shots: L-coil only and F-coil jogs. In the L-coil only shots the F-coil is neither not charged nor in the vacuum chamber. The L-coil current is ramped up to a level, held steady for a duration, then ramped back down. These shots allow verification of the L-coil model and the measurement of the L-coil current. F-coil jog shots are more complicated because they involve the levitated F-coil. In these shots the levitation feedback control system is used to lift the F-coil about 4 mm, hold it at this new position for a duration, then return the F-coil to its original position. These shots allow verification of the F-coil model and the measurement of the F-coil position.

It is more difficult to model the F-coil jog than it is to model the L-coil alone. Part of the difficulty is that it requires a more complicated model (two coils, one of which is a flux conserving superconductor) but the primary difficulty is knowing the position of the F-coil. The levitation system uses multiple lasers to determine the location and velocity of the F-coil. These lasers can be used as a measurement of the F-coil position; however, they must be calibrated for every lift of the F-coil. The absolute measurement of the F-coil position based on the lasers can be off by as much as 1 cm. The relative position (movement from the established zero point on a lift) is sensitive to how the lasers have been tuned (with a screwdriver) but can be reasonably calibrated with a linear scale factor (i.e., $z_{real} = Az_{laser} + B$). The calibration of the absolute and relative position of the F-coil are done with the magnetics using a vacuum F-coil jog shot.

It is important to emphasize some of the scales involved here. The F-coil is about 1 meter in diameter, weighs about 565 kg, carries about 1.2 MA of current, and is suspended

magnetically about 1.5 m below the L-coil. The calibrations of the laser positions are necessary because the magnetics are sensitive to as little as a 0.1 mm change in the relative position of the F-coil (that is a tenth of a millimeter change in the F-coil position during the shot, not a tenth of a millimeter change in the absolute position). A Monte Carlo estimation of the errors in the calibrated position of the F-coil shows that the changes in the vertical position of the F-coil are measured to an accuracy of less than 0.1 mm.

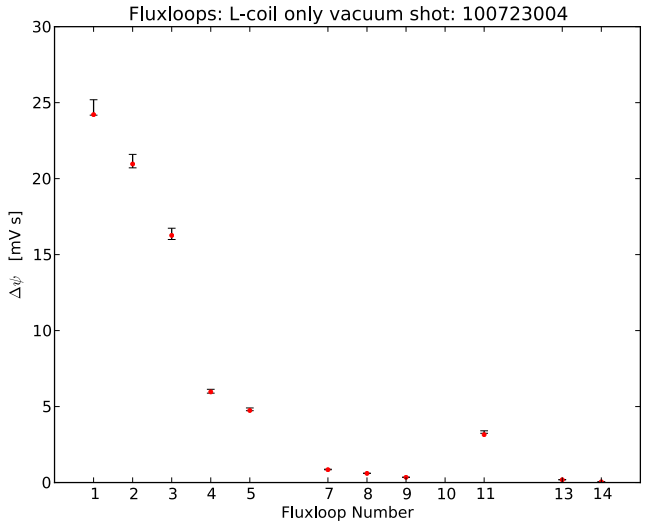

(a)

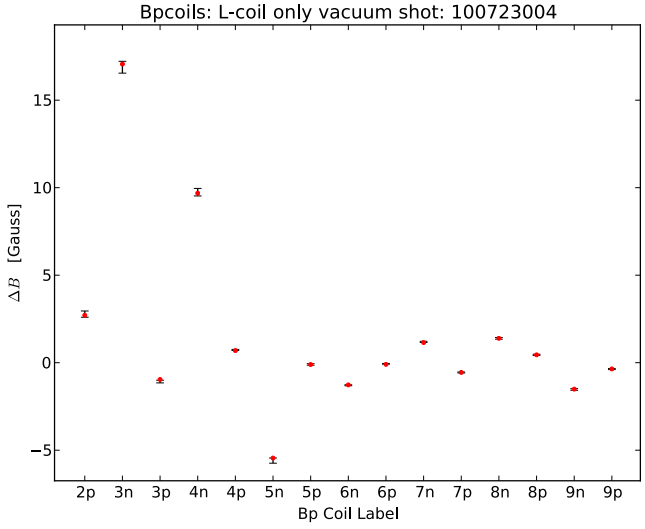

(b)

Figure 4.4: The magnetic measurements agree well with the model for a vacuum magnetics shot 100723004 in which the L-coil current is ramped up to a steady level and there is no F-coil: (a) the flux loops and (b) the poloidal field coils. B_p coils 1N, 1P, and 2N have been omitted because they are close to the L-coil so the assumption that the magnetic field is constant across the coil is not correct. Also, the integrator on flux loop 10 railed on this shot so it has been omitted.

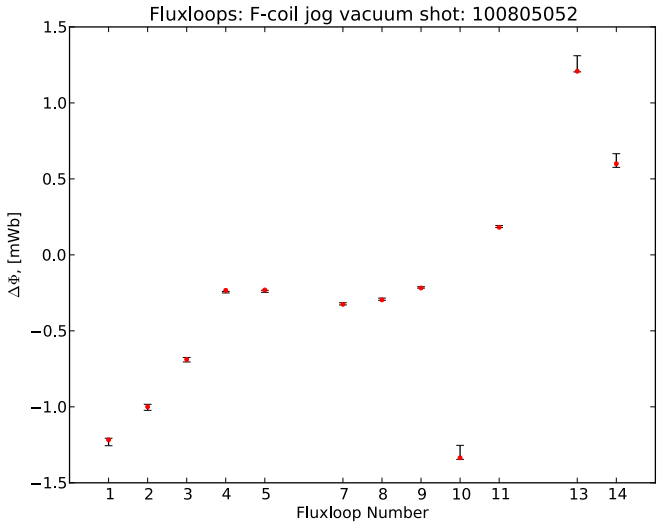

(a)

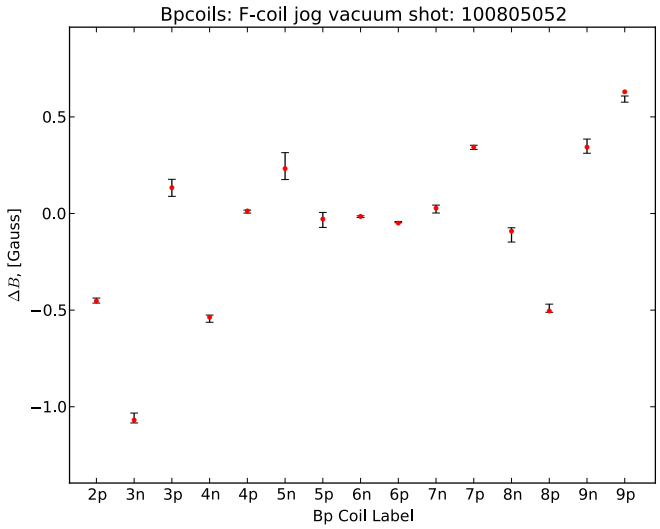

(b)

Figure 4.5: The magnetic measurements agree well with the model for a vacuum magnetics shot 100805052 in which the F-coil is vertically displaced (jogged) 4mm: (a) the flux loops and (b) the poloidal field coils. B_p coils 1N, 1P, and 2N have been omitted because they are close to the L-coil so the assumption that the magnetic field is constant across the coil is not correct.

4.5 Python based magnetic reconstruction code

4.5.1 The Finite Volume Method (FVM)

The FVM is a numerical technique that transforms a partial differential equation applied on a discrete domain into a set of algebraic equations. As an illustrative example the Poisson equation, which has structural similarity to the axisymmetric Ampere's equation shown in eq. (4.7), can be solved on a simple cartesian domain with the FVM. Begin with the Poisson equation:

$$\nabla^2 V = \nabla \cdot \nabla V = -\frac{\rho}{\epsilon_0}. \tag{4.25}$$

Integrate eq. (4.25) over a cell volume ($A = \Delta x \Delta y$) and apply the divergence theorem:

$$\int \nabla \cdot \nabla V dA = \int \nabla V \cdot \hat{n} dS = -\int \frac{\rho}{\epsilon_0} dA \tag{4.26}$$

where $\hat{n}$ is a vector normal to the cell surface and dS is a unit area of the surface. Figure 4.6 illustrates the computational domain. Referencing this illustration, an explicit form for the middle term in eq. (4.26) is

$$\int \nabla V \cdot \hat{n} dS \approx \left(\frac{\partial V}{\partial x}\right)_A \Delta y - \left(\frac{\partial V}{\partial x}\right)_B \Delta y + \left(\frac{\partial V}{\partial y}\right)_C \Delta x - \left(\frac{\partial V}{\partial y}\right)_D \Delta x. \tag{4.27}$$

The derivatives can be approximated from the volume averaged values of the adjacent cells:

$$\begin{aligned} \left(\frac{\partial V}{\partial x}\right)_A &= \frac{V_{i+1,j} - V_{i,j}}{\Delta x} \quad , \quad \left(\frac{\partial V}{\partial x}\right)_B = \frac{V_{i,j} - V_{i-1,j}}{\Delta x} \\ \left(\frac{\partial V}{\partial y}\right)_C &= \frac{V_{i,j+1} - V_{i,j}}{\Delta y} \quad , \quad \left(\frac{\partial V}{\partial y}\right)_D = \frac{V_{i,j} - V_{i,j-1}}{\Delta y}. \end{aligned} \tag{4.28}$$

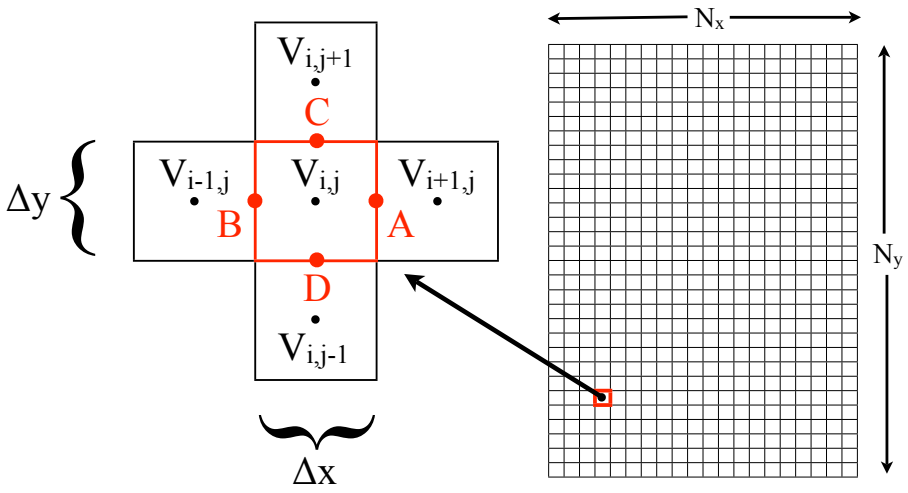

Figure 4.6: For the FVM the computational domain is broken into discrete volumes. Here the domain is broken into a cartesian grid with N_x cells in the x-direction and N_y cells in the y-direction. The volume averaged value of V in cell (i, j), which is named $V_{i,j}$, is calculated by using the values of the adjacent cells to calculate the flux through the edges of cell (i, j).

Combining eqs. (4.26) to (4.28) the equation for the value of the volume averaged electric potential in cell (i, j) can be written as

$$(V_{i+1,j} - 2Vi,j + V_{i-1,j})\left(\frac{\Delta y}{\Delta x}\right) + (V_{i,j+1} - 2Vi,j + V_{i,j-1})\left(\frac{\Delta x}{\Delta y}\right) = -\frac{\bar{\rho}\Delta x\Delta y}{\epsilon_0}. \quad (4.29)$$

where $\bar{\rho}$ is the volume averaged charge density. Equation (4.29) is a set of N_xN_y linear equations for the volume averaged electric potential in each the N_xN_y cells. Boundary terms that appear on the left side of eq. (4.29) can be moved to the right side and the equation can be cast as the linear algebra standard: $A\mathbf{x} = \mathbf{b}$.

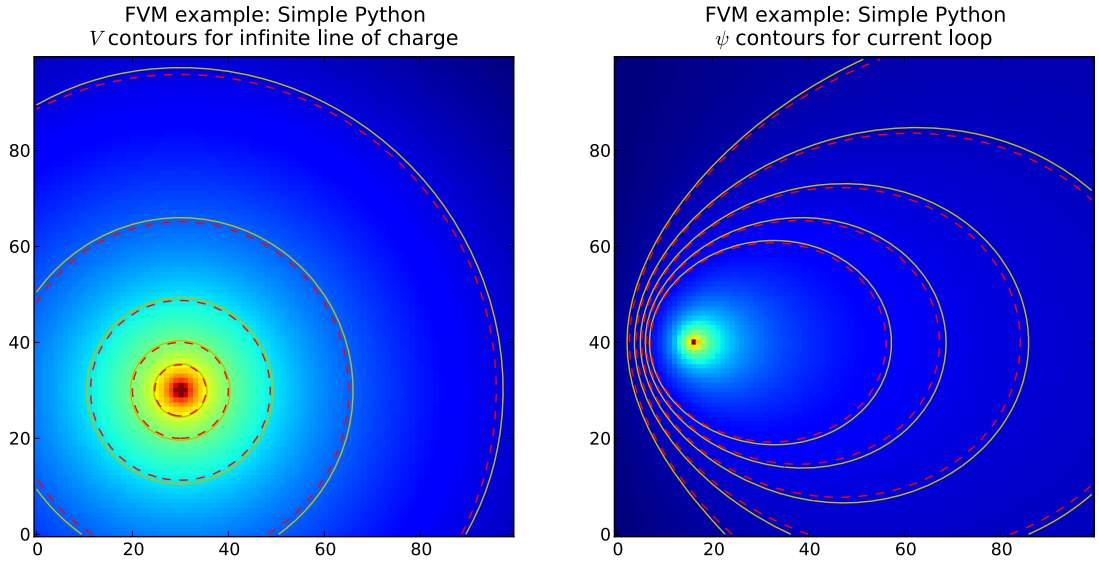

(a) (b)

Figure 4.7: A simple Python implementation of the finite volume method with a 100×100 grid to solve (a) the electric potential of an infinite line of charge and (b) solutions to the axis-symmetric Ampere's equation for a single loop of current. Solid yellow contours indicate solutions from the FVM; red dashed contours indicate solutions calculated directly from the analytic form. The FVM solver used for this figure was not used for the magnetic reconstructions in this thesis, instead, a more robust solver developed at NIST called FiPy was used for the magnetic reconstructions. FiPy is discussed in the next section.

4.5.2 FiPy

The finite volume solver used in this thesis to solve the axis-symmetric Ampere's equation on a computational domain is call FiPy and was developed at NIST. The developers describe FiPy as "an object oriented, partial differential equation (PDE) solver, written in Python, based on a standard finite volume (FV) approach" [66, 67].

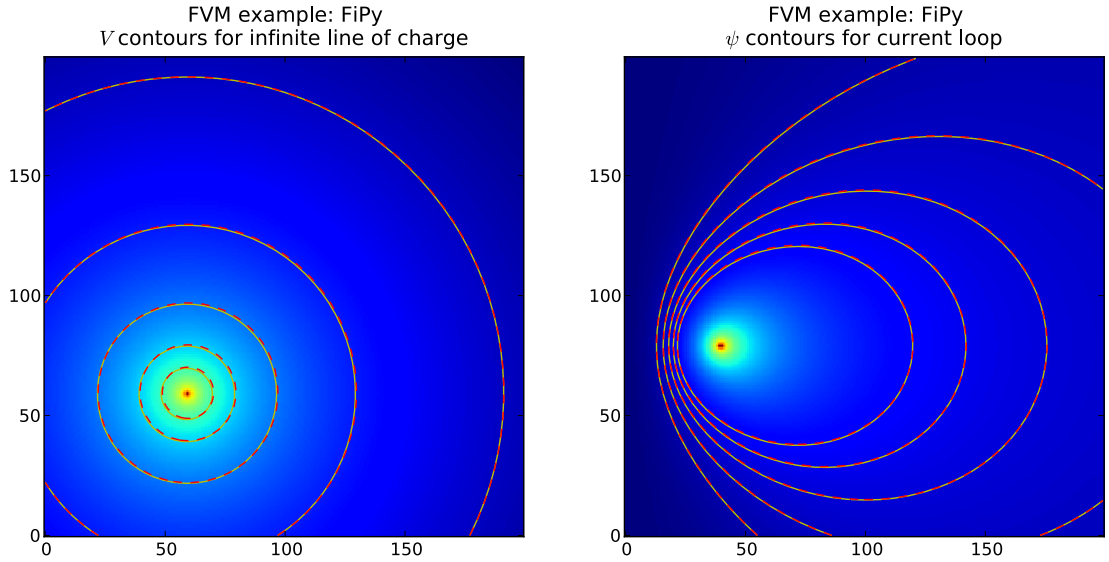

(a) (b)

Figure 4.8: Fipy implementation of the finite volume method with a 200×200 grid to solve (a) the electric potential of an infinite line of charge and (b) solutions to the axis-symmetric Ampere's equation for a single loop of current. Solid yellow contours indicate solutions from the FVM; red dashed contours indicate solutions calculated directly from the analytic form. There is strong agreement between the FVM solution and the analytic solution.

4.5.3 Magnetic reconstruction code overview

The magnetic reconstruction code is written in Python [66, 67, 68, 69]. Figure 4.9 is a block diagram describing the basic flow of the magnetic reconstruction code. The magnetic reconstruction of a shot begins with a sampling of the data. The data sampled includes the magnetic flux loop and poloidal field coil data and parts of the levitation control system data (namely, the levitation coil current and floating coil position information). The data is sampled at three times (before the shot, at the time of interest for the reconstruction, and after the shot) so that the data can be calibrated. The calibration of the magnetics signals involves removing known integrator gains from the raw signals, and removing calculated integrator drifts in such a manner as to account for a change in the position of the floating

coil between the beginning and end of the shot.

Figure 4.9 breaks the reconstruction into two blocks: χ^2 minimization and ldxgrid.py. The blocks interact as follows. The χ^2 minimization block passes a model and a set of parameters to the ldxgrid.py block. The ldxgrid.py block simulates a set of measurements using the received model and parameters and passes this model data back to the χ^2 minimization block. The χ^2 minimization block then compares the simulated measurements to the real, calibrated measurements to determine if the model and parameters were good. If the model is good, success is declared. If the model is not good, then the χ^2 minimization block selects another model and/or set of parameters and sends it to the ldxgrid.py block. Thus, the essential task of the χ^2 minimization block is to find the model and parameter set that brings the best agreement between the calibrated data and model data. The essential task of the ldxgrid.py block is to properly simulate the measurements when given a model and parameter set.

The details of the χ^2 minimization block (such as the definition of χ^2, the pressure model, the upper mirror plasma, and methods for finding the global minimum χ^2) are discussed in the following sections (see sections 4.6 to 4.8).

The details of the ldxgrid.py block distinguish the magnetic reconstruction of the pressure profile on LDX. A unique aspect of the magnetic reconstructions on LDX is that there is a flux conserving, superconducting, levitated magnetic dipole in the middle of the plasma. The current in the levitated dipole (alias, F-coil) is calculated at the beginning the shot before the creation of the plasma by force balance (i.e., the force between the F-coil and the L-coil needed to levitate the F-coil in the middle of the vacuum vessel). The current in the

F-coil at later times is calculated by conservation of the magnetic flux inside the F-coil:

$$I_{F0}L + I_{L0}M_{FL0} = I_{F1}L + I_{L1}M_{FL1} + \sum_{i}^{n^2} I_{Pi}M_{FPi} \tag{4.30}$$

where I_{F0} is the initial F-coil current (calculated from force balance), L is the self-inductance of the F-coil, I_{L0} is the initial current in the L-coil, M_{FL0} is the initial mutual inductance between the F-coil and the L-coil, I_{F1} is the new F-coil current (quantity to be solved for), I_{L1} the new L-coil current, M_{FL1} the new mutual inductance between the F-coil and L-coil (necessary if F-coil moves), I_{Pi} is the i^{th} of n^2 plasma currents (determined by pressure model where the model determines the currents on an $n \times n$ grid), and M_{FPi} is the mutual inductance between the i^{th} plasma current and the F-coil.

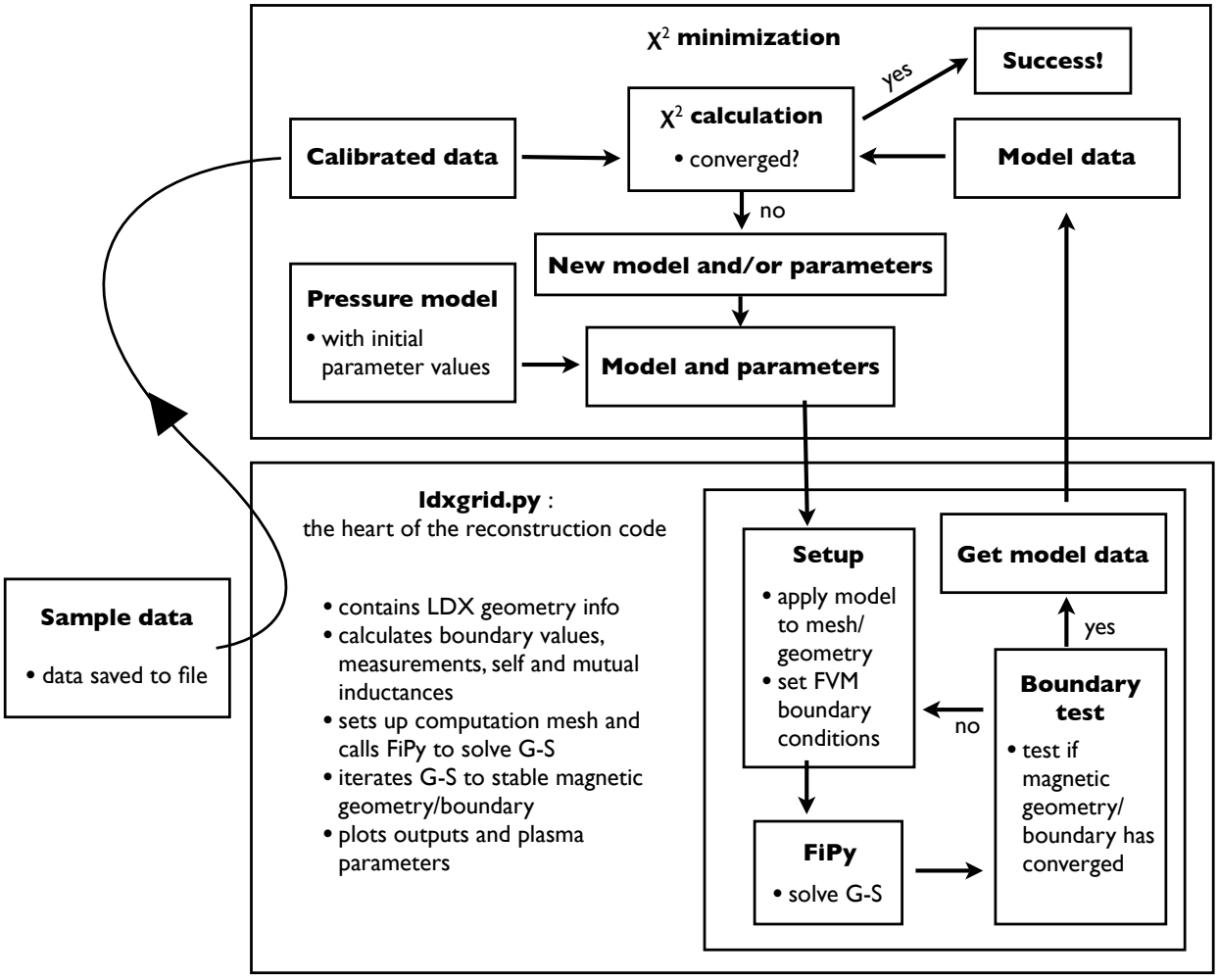

Figure 4.9: A block diagram depicting the basic magnetic reconstruction algorithm.

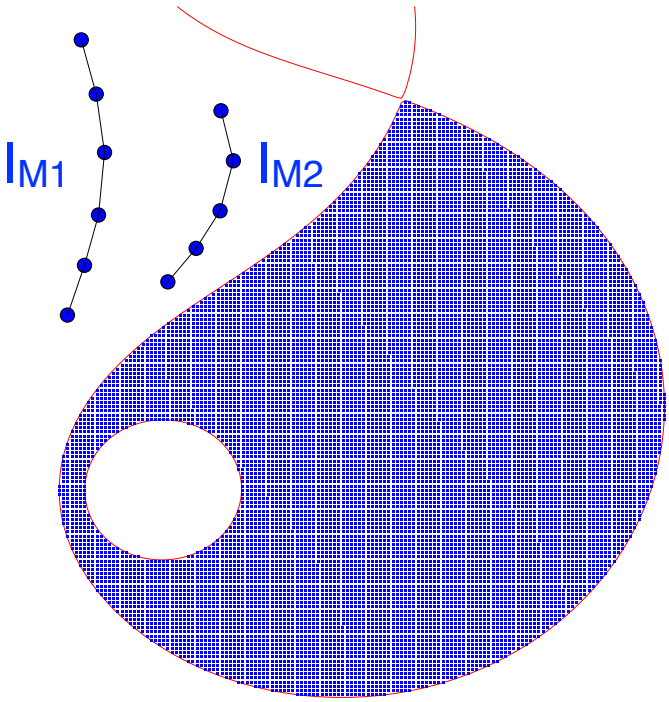

Figure 4.10: Plasma currents (shown as blue dots) are placed on grid nodes between the seperatrix (outer red contour) and the limited inner most flux surface (inner red contour) based on a pressure model. Additionally, currents are added in the upper mirror region. Two currents (I_{M1} and I_{M2}) are evenly distributed over a finite set of points in the upper mirror.

4.6 The upper mirror plasma

Magnetic measurements and images from a visible light camera show that often on LDX a plasma is confined in the a region referred to here as the upper mirror. The upper mirror is the magnetic mirror that exists between the F-coil and the L-coil. All magnetic field lines in this region are open so any plasma confined in the region must be trapped in the magnetic well. This thesis addresses the upper mirror plasma primarily to assess whether the currents in upper mirror plasma significantly effect the magnetic reconstructions. It is found that often there are significant currents in the upper mirror plasma thus requiring the upper mirror plasma to be incorporated into any current/pressure model. Figure 4.11 shows the upper mirror plasma seen on a visible light camera.

The upper mirror plasma is seperated by the mechanical upper catcher into an inner region (inside the catcher) and an outer region (outside the catcher). Figure 4.12 shows the electron cyclotron resonances zones for a typical magnetic configuration on LDX. The locations of the resonances indicate that the inner upper mirror plasma should only form when the 10.5 GHz and/or 6.4 GHz power sources are on (it should not form with just the 2.45 GHz power source). Figures 4.13(a) and 4.13(b) show that the inner plasma is seen on the visible light camera when all power sources are on but is not seen when only the 2.45 GHz source is on.

Instability, or some other unknown event, often causes the inner upper mirror plasma to be rapidly lost. When this loss occurs there is a rapid change in the flux measured by flux loop 11 that coincides with a simultaneous decrease in the visible light emitted from the region. Figure 4.14(b) shows this correlation between sudden changes in flux loop 11 and decreases in the visible light. A simple estimate of how much plasma current is in the inner upper mirror region can be made by looking at the change in flux loop 11. The inner upper

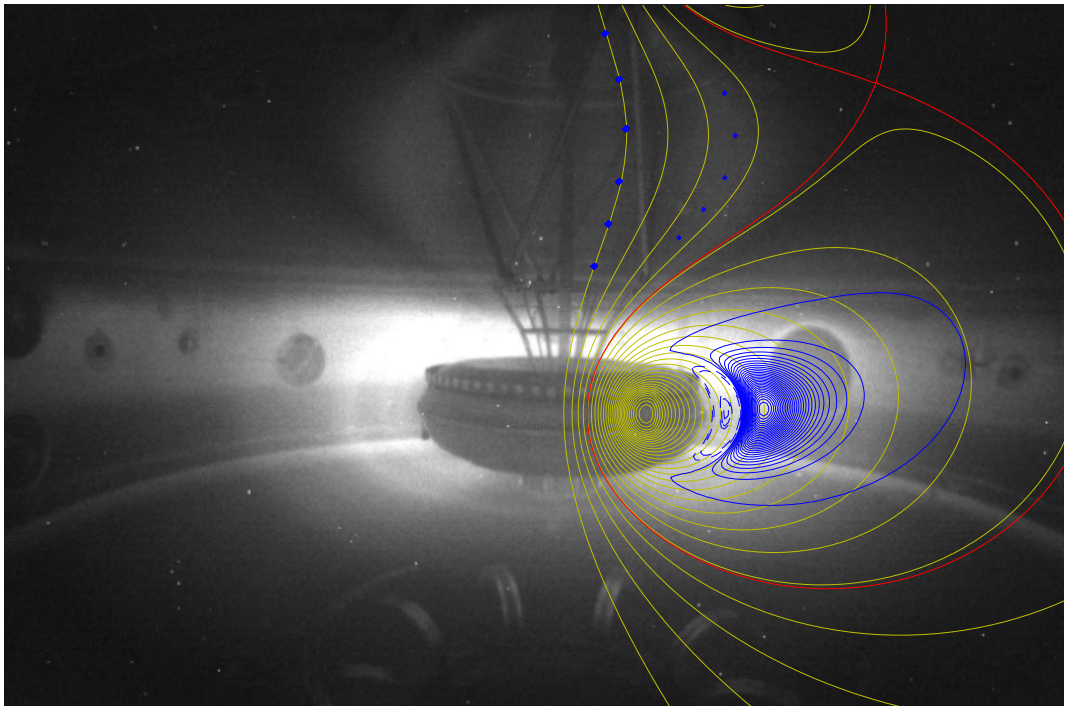

Figure 4.11: A grayscale visible light image of a plasma shot with magnetic field lines overlaid in yellow, separatrix in red, and current density contours in blue. The upper mirror plasma current is modeled as 2 currents (I_{M1} and I_{M2}) distributed over a finite set of points in the upper mirror.

mirror plasma can be modeled as a simple current ring concentric with flux loop 11 and with a diameter estimated from the visible light and the locations of the electron cyclotron resonances (see fig. 4.15). A further assumption is made that the sudden change in the flux at flux loop 11 is entirely due to the change in this ring current. Using this model the 0.3 mV s change in flux observed in the top panel of fig. 4.14(b) is a result of the loss of ~ 500 A of current. Thus there can be kiloamps of current in the inner upper mirror plasma which is an amount that cannot be neglected in magnetic reconstructions of current profile. In supported shot 100805045 a significant upper mirror plasma can be seen on the visible light camera and magnetic reconstructions estimate the inner upper mirror plasma to be 2.5 kA.

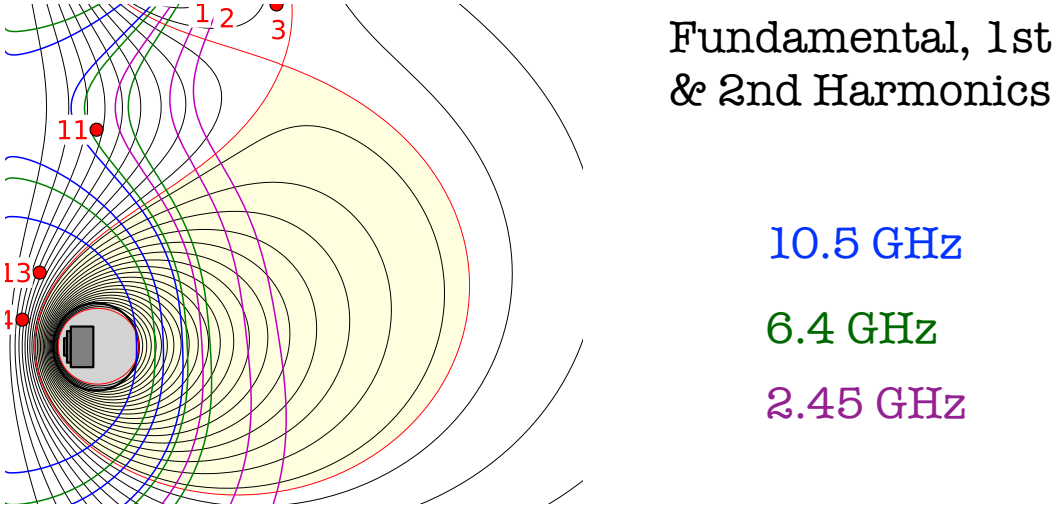

Figure 4.12: Electron cyclotron resonances for a typical magnetic configuration on LDX. The location of flux loop 11 is marked with a red dot and is located on the upper catcher and thus provides an indication of the inner and outer upper plasma regions.

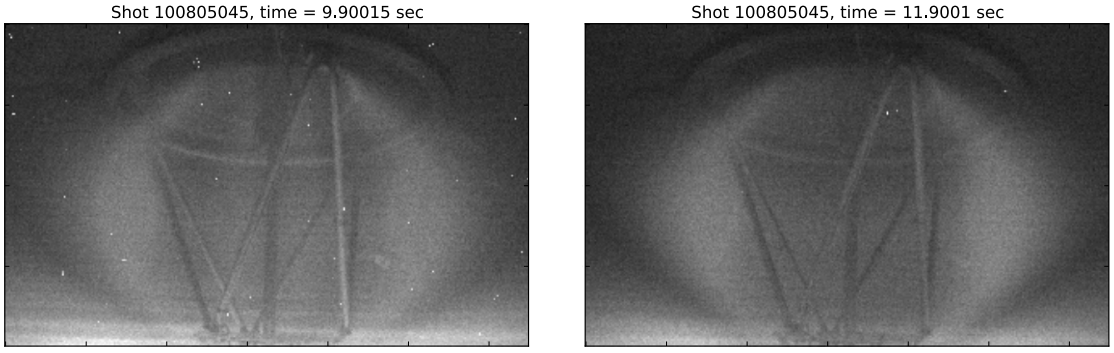

(a) (b)

Figure 4.13: Supported shot 100805045: (a) the inner upper mirror plasma is visible at time 9.9 sec when the 10.5 GHz, 6.4 GHz, and 2.45 GHz power sources are on, (b) the inner upper mirror plasma is not visible at time 11.9 sec when only the 2.45 GHz power sources are on.

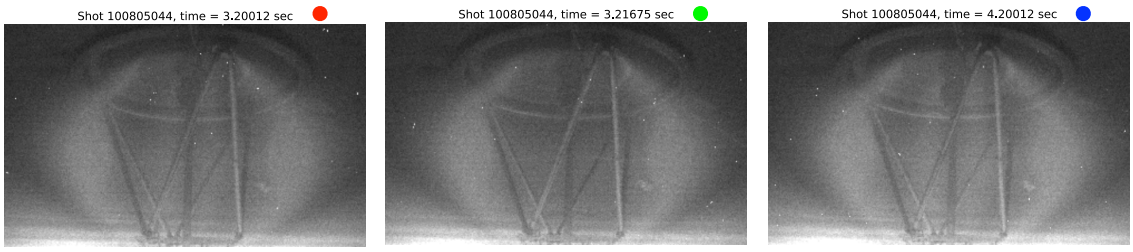

(a)

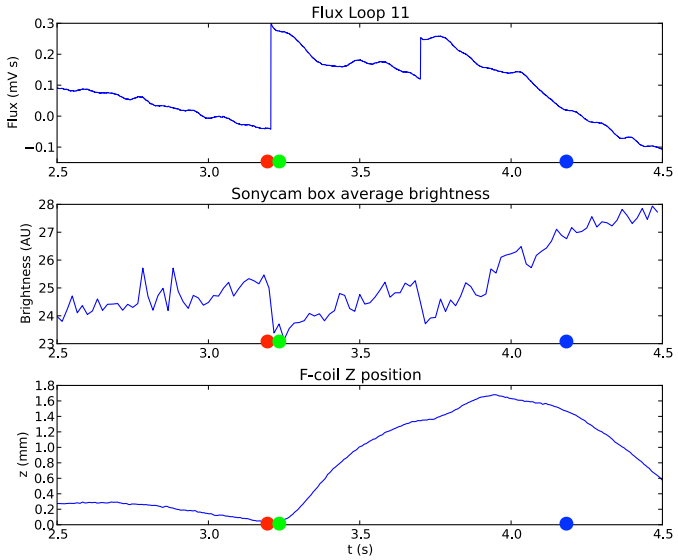

(b)

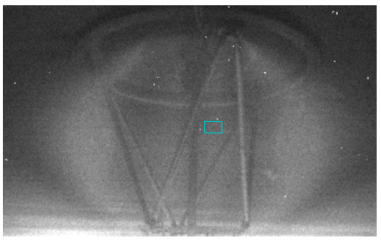

(c)

Figure 4.14: Observed instability of inner upper mirror plasma. (a) Visible light at three different times (indicated in (b) by red, green, and blue dots). (b) Time traces of the magnetic flux measured at flux loop 11, the intensity of the visible light emitted from the inner mirror region, and the position of the F-coil. (c) The cyan box marks the region of the visible camera view that was integrated to get the emitted light shown in the middle trace of (b).

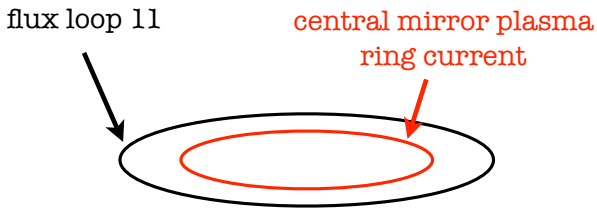

Figure 4.15: A very simple model for the inner upper mirror current shows that the inner upper mirror current can have kiloamps of current.

4.7 Pressure models

Magnetic reconstruction of the pressure profile in LDX is an inverse problem. With a finite number of measurements it is not possible to determine an arbitrary current distribution in the plasma so a model-based reconstruction is performed. The model constrains the number of possible current distributions. Because the current distribution is proportional to the gradient of the pressure distribution the model can be defined in terms of a continuous pressure profile. The boundary conditions of the pressure model are: the pressure goes to zero at the F-coil, the pressure has a positive peak between the F-coil and the separatrix, the pressure goes to a small value at the separatrix, and the pressure is azimuthally symmetric but can be anisotropic along the magnetic field. Also, as discussed in the previous section, the pressure model must account for the plasma current in the upper mirror region.

The model used in the magnetic reconstructions has 6 parameters: the pressure parameter (p_0), the radial location of the pressure peak (r_0), the profile steepness parameter (g), the anisotropy parameter (a), and the upper mirror currents (I_{M1} and I_{M2}). The focus of this thesis is the steepness parameter (g). This parameter quantifies how rapidly the pressure profile decreases between the pressure peak and the separatrix.

For an isotropic distribution the pressure is a flux function ($P_\perp = P_\parallel \equiv G(\psi)$). LDX plasmas tend to have anisotropic pressure distributions ($P_\perp \neq P_\parallel$) because electrons are heated with ECRH, which adds energy only the perpendicular component of the electron pressure, and the ratio of the trapped to passing particles can be very large (> 10).

The pressure anisotropy produces a variation of the pressure along the magnetic field so the pressure is no longer a flux function. Instead the pressure can be expressed as a function of two variables one across the field (ψ) and one along the field ($B(\psi, \chi)$, where χ is a coordinate marking the position on the field line) [70]. The anisotropic plasma equilib-

rium momentum equation implies $P_\perp = P_\perp(\psi, B)$ and $P_\parallel = P_\parallel(\psi, B)$ [71]. A simple model then defines the pressure as the product of two functions: $P_\perp(\psi, B) = G(\psi)H(\psi, B)$. The anisotropic pressure model employed here was introduced by Connor and Hastie [72] in their work on the stability of anisotropic plasmas confined in tokamaks. More recently the model was applied to the dipole geometry for equilibrium [73] and stability [71] studies. These studies make the simplifying assumption that the anisotropy is constant throughout the plasma and is parameterized as $P_\perp = (1 + 2a)P_\parallel$ where a is the anisotropy parameter mentioned in the previous paragraph. This simplification is implemented by defining $H(B) \equiv (B_0/B)^{2a}$, where B_0 is the minimum magnetic field strength on a field line. Thus, $H(B(\psi, \chi))$ can be viewed as an anisotropic modification to an isotropic distribution $G(\psi)$. The effect of $H(B)$ is that the pressure is highest at the minimum magnetic field regions where the ECRH can be most efficient, and the pressure decreases in regions of high magnetic field near the dipole poles.

The equilibrium diamagnetic current from an anisotropic distribution is found from the anisotropic momentum balance, eq. (4.2),

$$\mathbf{J} = \frac{\mathbf{B} \times \nabla \cdot \bar{\mathbf{P}}}{B^2} = \frac{\mathbf{B} \times \nabla \cdot P_\perp}{B^2} + \frac{\mathbf{B} \times \kappa}{B^2} \left(P_\parallel - P_\perp\right) \tag{4.31}$$

where $\kappa = \mathbf{b} \cdot \nabla \mathbf{b}$ is the magnetic curvature. By using the vacuum field approximation of the curvature vector, $\kappa \approx (\nabla_\perp B)/B$, the azimuthal component of the current density can be written in cylindrical coordinates as

$$J_\phi = -2\pi R \frac{\partial P_\perp}{\partial \psi} - 2\pi R \left(P_\parallel - P_\perp\right) \frac{\partial}{\partial \psi} (\ln B) \quad . \tag{4.32}$$

Using the definitions described above, $P_\perp = (1 + 2a)P_\parallel = GH$, the current density for the

pressure model is defined by

$$J_\phi = -2\pi RH\frac{dG}{d\psi} - 2\pi RGH\frac{2a}{1+2a}\left[2\left(1+a\right)\frac{\partial \ln\left(\frac{B_0}{B}\right)}{\partial\psi} - \frac{\partial \ln B_0}{\partial\psi}\right] . \tag{4.33}$$

where B_0 is the minimum value of the magnetic field strength along a field line, B is the magnetic field, and a is the anisotropy factor. The functions G and H define an isotropic pressure distribution and anisotropic modification to the pressure profile: $P_\perp = G(\psi)H(B(\psi,\chi))$. H is defined as:

$$H = \left(\frac{B_0}{B}\right)^{2a} \quad . \tag{4.34}$$

The isotropic pressure profile is trifurcated

$$G = P\left(\psi\right) = \begin{cases} p_0\left(\frac{\psi-\psi_{fcoil}}{\psi_0-\psi_{fcoil}}\right)^{\alpha} & , \quad \psi > \psi_0 + \delta\psi \\ A\psi^2 + B\psi + C & , \quad \psi_0 + \delta\psi > \psi\, \psi_0 - \delta\psi \\ p_0\left(\frac{\psi}{\psi_0}\right)^{4g} & , \quad \psi \leq \psi_0 - \delta\psi \end{cases} \tag{4.35}$$

where $\psi_0 = \psi(r_0)$, ψ_{fcoil} is the value of ψ at the F-coil, and $\alpha = 4g\left(|\psi_{fcoil}/\psi_0| - 1\right)$. The coefficients A, B, and C are defined such that G and $dG/d\psi$ are continuous. The width $\delta\psi$ is a fixed value that typically spans about a 5 cm radial distance at the mid-plane.

The upper mirror plasma currents are modeled as 2 currents distributed over a spatially distributed set of filaments. The location of these filaments was chosen based on light viewed from the region on a visible camera and the calculated locations of the heating resonances. Figure 4.11 illustrates the location of the upper mirror filaments.

The motivation for the trifurcated pressure profile chosen is that it satisfies the basic physical requirements (pressure is zero at the F-coil, etc.) and has a parameterization

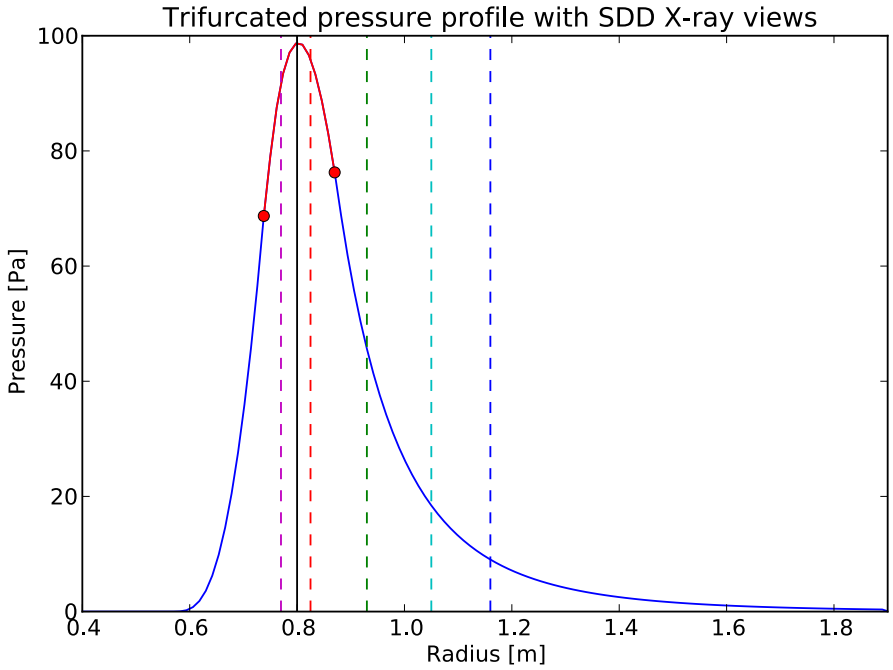

Figure 4.16: Illustration of the trifurcated pressure model at the mid-plane. The blue and red sections mark the different regions defined by eq. (4.35) (note: $\psi \sim 1/r$). The solid black line marks the pressure peak. The dashed lines mark the tangency radii of the SDD X-ray detector views.

that tests whether the plasma assumes an invariant profile outside of the pressure peak. In choosing a pressure profile there is a natural bifurcation between the regions inside and outside of the pressure peak. Inside the peak there is favorable magnetic field curvature thus the plasma may be stable even with a steep pressure gradient. Outside the pressure peak there is unfavorable magnetic field curvature and the steepness of the thermal pressure profile is limited by stability to the MHD interchange mode. A trifurcated model was chosen because it provides a smooth transition between the inside and outside regions. The parabolic pressure profile provides a linear transition between the negative azimuthal current density inside the pressure peak to the positive azimuthal current density outside the peak. The current profile is illustrated in fig. 4.17.

The trifurcated model is used in the reconstructions in this thesis but other models were examined [43]. Models that satisfied the basic physical requirements generally produced results that were qualitatively similar to the trifurcated model (i.e., supported shots had much steeper pressure profiles outside the peak than levitated shots); however, these models were less extensively examined.

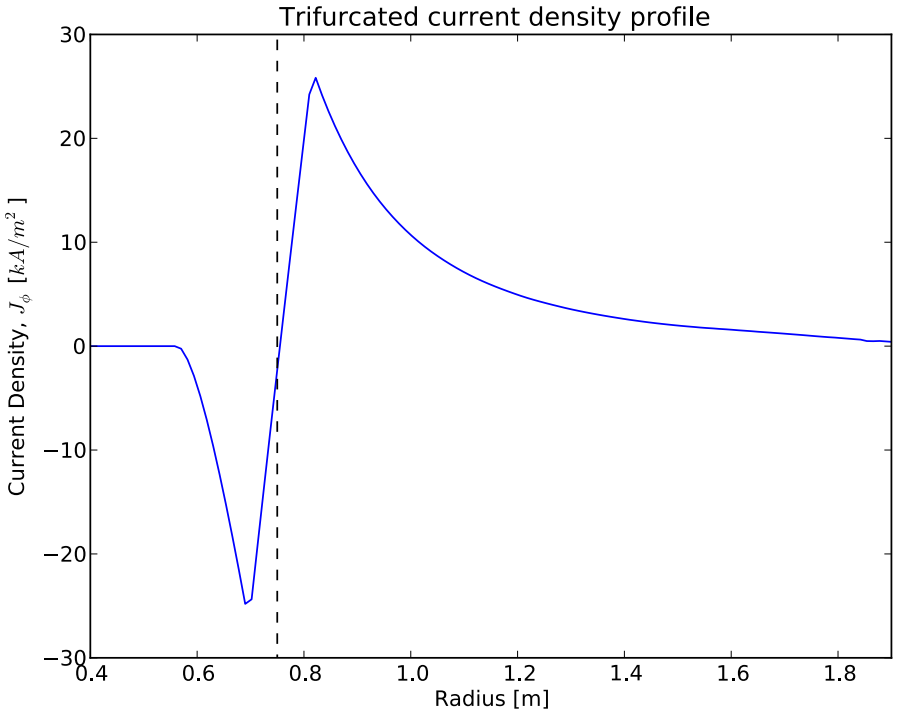

Figure 4.17: Illustration of the trifurcated current model at the mid-plane. The dashed black line marks the pressure peak.

The anisotropy factor constrains the pressure (and current) to the region near the minimum of the magnetic field strength along a magnetic field line. In supported operation the plasma is anisotropic in part because particles that are scattered into the loss cone are lost to the mechanical supports. In levitated operation the plasma is expected to be more isotropic because the mechanical supports are removed so a drive for the anisotropy

is removed; however, anisotropy drives still exist in levitated operation. The ECRH drives drives some anisotropy since it only heats the perpendicular component of the electron momentum. Additionally, some heating sources (6.4 GHz and 10.5 GHz) have their primary mid-plane heating resonance located on field lines that terminate on the F-coil itself, so levitation does not close these field lines and the populations created by these sources may be very anisotropic. Previous work on LDX supported plasmas used an X-ray camera to image the anisotropy by looking at the X-ray emission from the mirror-trapped, energetic electrons. The anisotropy calculated from those measurements corresponds to an anisotropy parameter of 2 ($P_\perp/P_\parallel = 5$). The X-ray camera was not operational for more recent levitated experiments but it is reasonable to assume that the anisotropy measured in supported operation provides an upper bound to the anisotropy that may be observed in levitated operation. Figure 4.18 illustrates the current distributions for several different anisotropy factors. Figure 4.19 shows the X-ray imaging of the anisotropy for a supported LDX plasma [74].

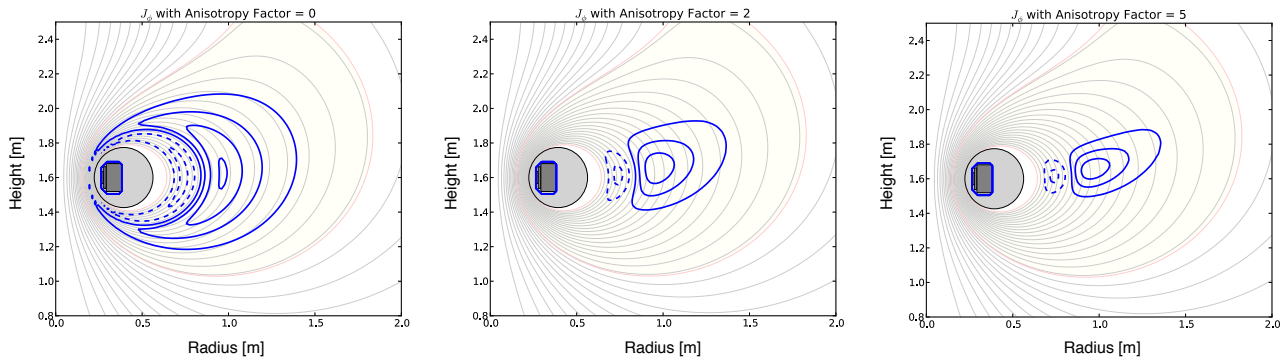

Figure 4.18: Illustration of current density for different anisotropy factors: 0, 2, and 5.

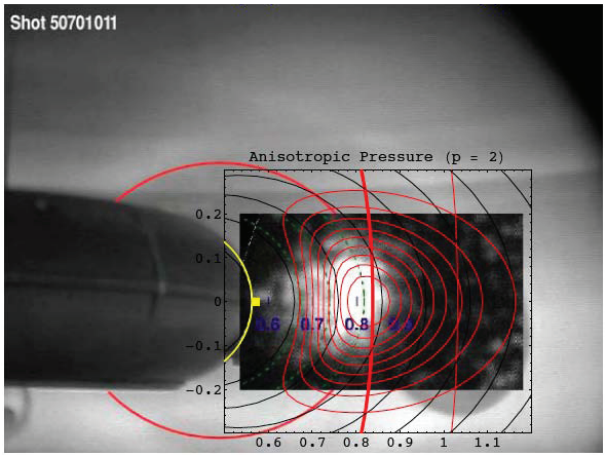

Figure 4.19: X-ray camera image showing the pressure anisotropy for a supported plasma without the L-coil current [74].

4.7.1 Relating the steepness parameter, g, to the profile stability

The thermal plasma pressure is marginally stable to the MHD interchange mode when $pV^{\gamma} = constant$. Thus, the MHD stability of a reconstructed pressure profile can be evaluated by multiplying it by the magnetic flux-tube volume taken to the power of γ. If the quantity $p(\psi)V(\psi)^{\gamma}$ increases with radius the pressure profile is MHD stable; if the quantity $p(\psi)V(\psi)^{\gamma}$ decreases with radius the pressure profile is MHD unstable (and the reconstructed pressure likely includes pressure from a gyrokinetically stablized hot electron population).

When evaluating $p(\psi)V(\psi)^{\gamma}$ an artifact of the pressure model described in the previous section should be noted. The model fits the pressure outside the pressure peak to a function that goes as $p(\psi) \propto \psi^{4g}$. For the geometry of a point dipole (in which $V \sim \psi^{-4}$) the steepness parameter is nearly (but not exactly) equal to the ratio of specific heats, γ, for a marginally MHD stable pressure profile. The actual flux-tube volume on LDX has a more complicated radial dependence with $V \sim \psi^{-4.5}$ at small radii and $V \sim \psi^{-5.5}$ for radii

nearer the separatrix. The effect of this variation in the flux-tube volume is that even for a marginally MHD stable reconstructed pressure profile the quantity $p(\psi)V(\psi)^\gamma$ will deviate some from a constant value, specifically, it will increase at large radius ($R > 1.5$ m). Figure 4.20 illustrates $p(\psi)V(\psi)^\gamma$ for a pressure profile that is marginally stable to the MHD interchange mode for both the ideal case and for a hypothetically reconstructed case.

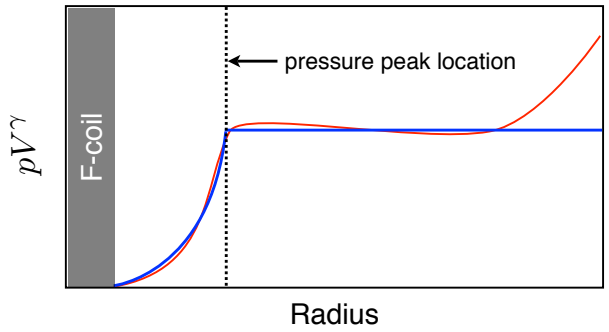

Figure 4.20: Illustration of $p(\psi)V(\psi)^\gamma$ for a marginally MHD stable pressure profile. The blue curve illustrates an ideal pressure profile for which the entropy density factor, $p(\psi)V(\psi)^\gamma$, is a constant outside the pressure peak. The red curve illustrates the entropy density factor as a function of radius for a hypothetical fit to the pressure profile. The entropy density factor is constant for much of the radial profile but increases at large radius because the flux-tube volume increases rapidly in a manner not accounted for in the pressure model.

4.8 Model fitting: χ^2 minimization

The plasma pressure profile on a shot is determined by comparing the magnetic flux loop and poloidal field coil measurements to the values predicted by the parameterized pressure model. This is done by a nonlinear χ^2 minimization where the figure of merit, χ^2, is defined

$$\chi^2 = \sum_{i=1}^{N} \frac{(M_i - C_i)^2}{\sigma_i^2} \tag{4.36}$$

where the summation is over the N measurements, M_i is the i^{th} measurement, C_i is the modeled i^{th} measurement, and σ_i^2 is the variance of the i^{th} measurement. Clearly, the closer the model matches the measurement the lower the value of χ^2; however, too low a value of χ^2 may indicate that the measurement error bars have been over estimated [75].

A number of methods have been implemented to gain a sense of the parameter space. The two most straight forward will be mentioned here: a parameter scan to map the variation of χ^2 in the parameter space and the Nelder-Mead downhill simplex method (alias, amoeba method) [76]. The two techniques have diametric advantages and disadvantages. The parameter scan gives a broad but coarse perspective of the parameter space. The simplex method finds a local minimum through many fine steps but is oblivious to the global features of the parameter space (i.e., there is no assurance that the local minimum found is a global minimum). By combining both methods the global minimum can be found with reasonable confidence.

4.9 Monte Carlo estimation of parameter errors

A Monte Carlo method is used to estimate the errors in the parameter values calculated by the magnetic reconstruction [75]. Analytically propagating the measurement errors to determine the errors in the calculated parameter values would be a cumbersome and potentially unfruitful task due to the iterative, nonlinear nature of the minimization algorithm. The Monte Carlo method provides a straightforward means of estimating the uncertainties in the parameter values due to the uncertainties in the measurements.

The method is performed by analyzing many synthetic datasets that are generated from the real dataset and knowledge of the model and measurement errors. In a fantastic world

the experimenter would know the true model parameters, $\mathbf{P}_{true}$. Synthetic datasets, $\mathbf{M}_i$, could then be generated by randomly sampling the measurement distribution appropriate for the true model parameters. Analyzing the datasets $\mathbf{M}_i$ would then lead to the sets of parameters $\mathbf{P}_i$. The distribution $\mathbf{P}_i - \mathbf{P}_{true}$ would then show the variation of the parameters due to the uncertainty in the measurements.

Alas, the experimenter is destined to never know $\mathbf{P}_{true}$! Only nature knows $\mathbf{P}_{true}$. The experimenter must settle for the set of parameters $\mathbf{P}_0$ that has been deduced from the set of real measurements $\mathbf{M}_0$. The key assumption of the Monte Carlo method is that $\mathbf{P}_0$ is similar enough to $\mathbf{P}_{true}$ that it can act as a surrogate. Specifically, the method assumes that the measurements are good enough that $\mathbf{P}_0$ is near $\mathbf{P}_{true}$, and that the way random errors propagate in the system is not a strong function of $\mathbf{P}_{true}$. Thus, when the procedure described in the previous paragraph is performed with $\mathbf{P}_0$ instead of $\mathbf{P}_{true}$ the distribution $\mathbf{P}_j - \mathbf{P}_0$ will have a distribution similar to $\mathbf{P}_i - \mathbf{P}_{true}$.

4.10 Magnetic reconstruction: A test case

In this section the magnetic reconstruction process is evaluated for an artificial test case. The measurement data for the test case is generated from the model profile with random measurement errors. Table 4.2 shows the model parameters used to generate the test case measurements. Figures 4.21 and 4.22 show that the magnetic reconstruction correctly calculates the the values of the measurement parameters. Figure 4.23(a) shows how the reconstructed steepness parameter and pressure peak location vary for different values of the anisotropy parameter. Figure 4.23(b) shows that the anisotropy parameter is resolved in the test case.

Test case	
Model Parameters	
Pressure parameter, p_0	500 Pa
Pressure peak location, r_0	0.75 m
Profile steepness parameter, g	1.7
Anisotropy parameter, a	0.5
Upper mirror inner current, I_{M1}	$0A$
Upper mirror outer current, I_{M2}	-150A
Plasma Parameters	
Peak pressure	361 Pa
Plasma energy	321 J
Beta at pressure peak	7.0 %
Total plasma current	3.4 kA
Plasma dipole moment	15.6 $kA \cdot m^2$

Table 4.2: Pressure profile parameters for magnetic reconstruction test case.

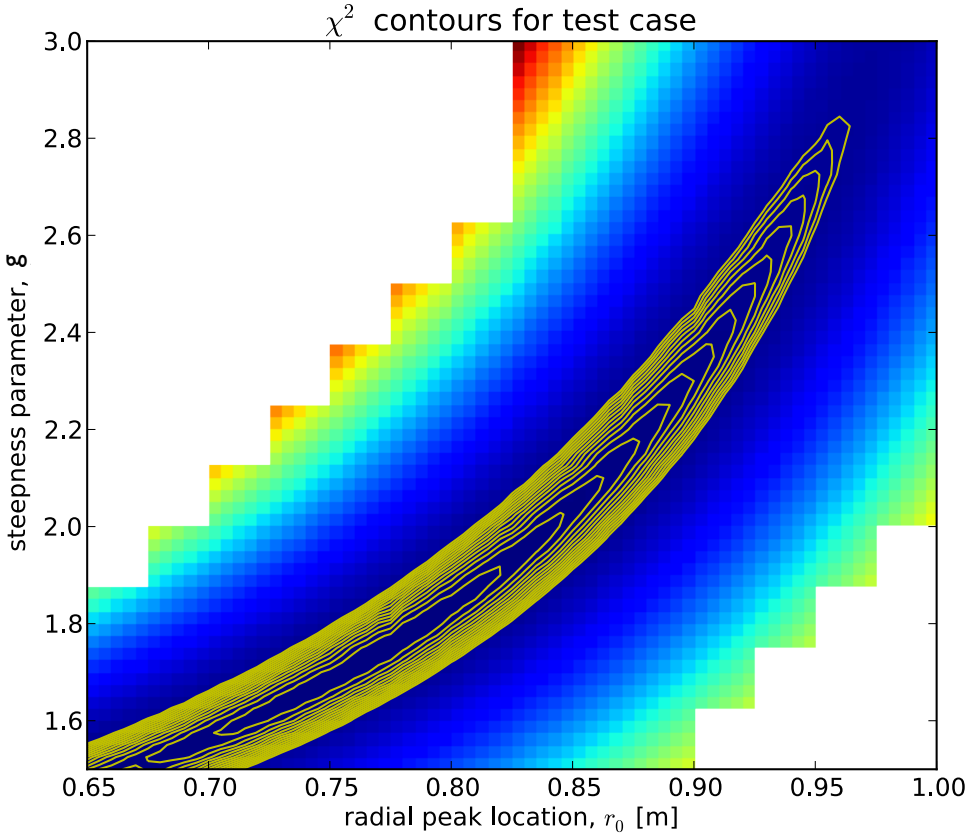

Figure 4.21: χ^2 contours in yellow for the test case. The underlaid image shows the χ^2 values with blue indicating small χ^2 and red indicating large χ^2. The contours of minimum χ^2 are closed and surround the model parameters showing that the magnetic reconstruction correctly determined the parameter values.

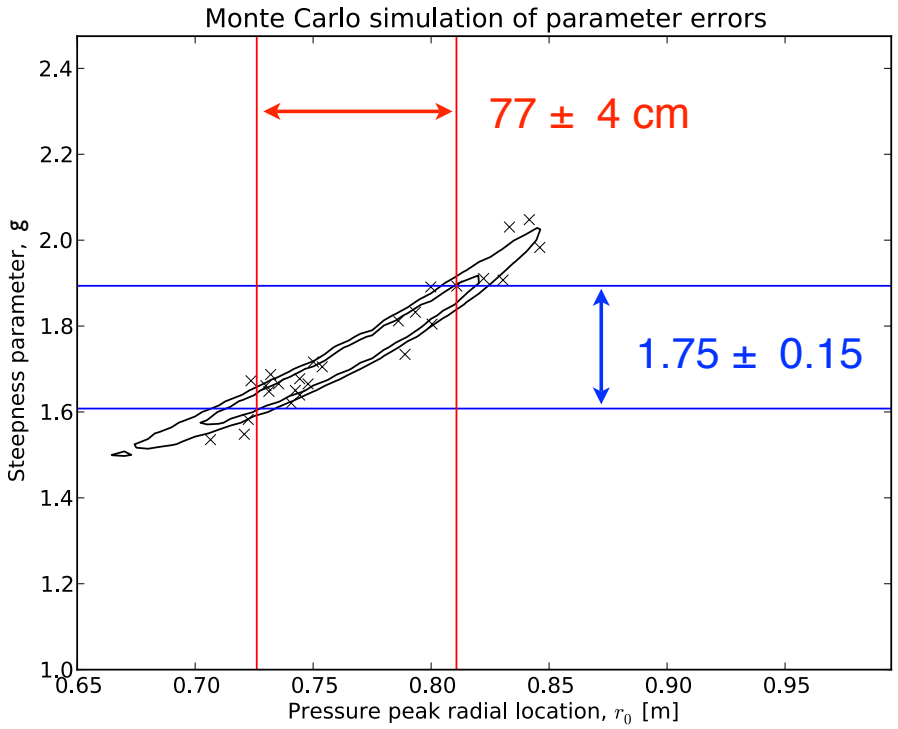

Figure 4.22: Monte Carlo estimation of parameter errors for levitated test case. The value of the steepness parameter is 1.75 with a standard deviation of about 0.15. The 'x' marks indicate the value of the steepness parameter, g, and the pressure peak location for χ^2 minima found for different synthetic data sets. The black contours are χ^2 contours from the initial synthetic data set. The inner contour is defined by $\chi^2 = \chi^2_{min} + \delta\chi^2$ where $\chi^2_{min} = 14$ and $\delta\chi^2 = 1$.

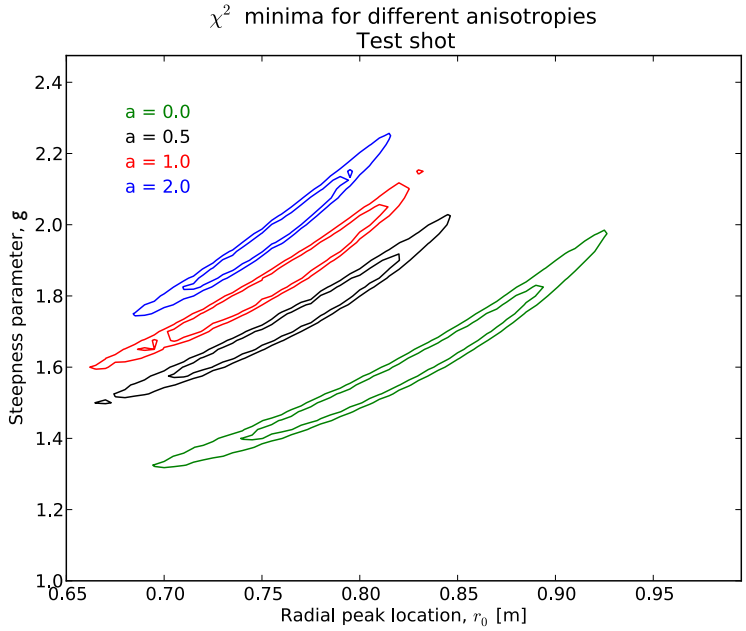

(a)

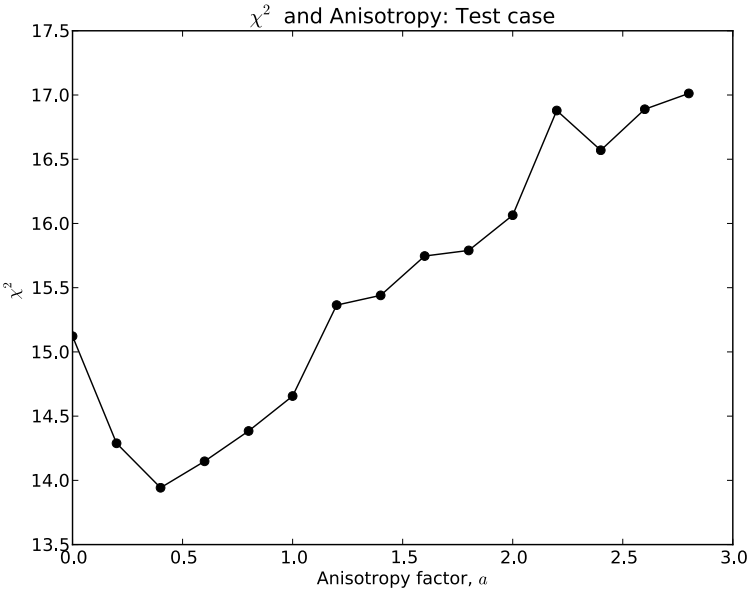

(b)

Figure 4.23: (a) Contours illustrating how the χ^2 minimum moves in the parameter space for different values of the anisotropy parameter. (b) A scan of the anisotropy parameter showing that the model and minimization algorithm find the correct anisotropy parameter ($a = 0.5$) for the test case. However, the sensitivity to the anisotropy parameter is low.

Chapter 5

Magnetic reconstructions: Results

This section presents results from magnetic reconstructions of the plasma pressure profile. One important aim of this thesis is to evaluate whether thermal plasmas confined in the magnetic field of a levitated dipole adopt invariant pressure profiles ($pV^{\gamma} = constant$). For this reason, the analysis here focuses on the steepness of the pressure profile gradient that best fits the measurements. This is quantified by the steepness parameter, g (see section 4.7). The relation between the steepness parameter and the thermal plasma MHD stability is shown by plotting the entropy density factor, $p(\psi)V(\psi)^{\gamma}$. If the entropy density factor increases with radius the plasma is MHD stable; if the entropy density factor decreases with radius the pressure gradient is steeper than the MHD limit. Pressure profiles with gradients steeper than the MHD limit for a thermal plasma are observed on LDX because of the presence of a gyrokinetically stabilized hot electron population that is created by the ECR heating sources.

Table 5.1 summarizes a variety of reconstructed shots. First a comparison is made between levitated and supported operation. It is found that during supported operation

the pressure profile is very peaked ($g > 3$). When the coil is levitated the pressure profile broadens ($g \sim 2$). The next reconstructed shots were examined to explore the conditions that produce broader pressure profiles. It is generally found that denser plasmas with fewer hot electrons have broader profiles.

Shot number	Power sources	Comment
100805046 (levitated) 100805045 (supported) [Deuterium]	2.45 GHz (5 kW) 6.40 GHz (3 kW) 10.5 GHz (10 kW)	Compare levitated and supported operation: *Pressure profile is broader when levitated ($g \sim 2$) than when supported ($g \sim 5$)*
100805046 (levitated) 100805045 (supported) [Deuterium]	2.45 GHz (5 kW)	Compare levitated and supported operation: *Pressure peak moves outward during levitation but pressure gradient is similar in levitated and supported operation ($g \sim 3.5$)*
100804017 (levitated) [Deuterium]	10.5 GHz (5 kW) ——————— 10.5 GHz (5 kW) 28 GHz (5 kW)	Compare with and without 28.0 GHz source: *Pressure profile is broader with 28.0 GHz source.*
100805028 (levitated) [Deuterium]	2.45 GHz (5 kW) 6.40 GHz (3 kW) 10.5 GHz (10 kW) ——————— 2.45 GHz (5 kW) 6.40 GHz (3 kW) 10.5 GHz (10 kW) 28.0 GHz (10 kW)	Compare with and without 28.0 GHz source: *Pressure profile is broader with 28.0 GHz source.*
100806016 (levitated) [Helium]	2.45 GHz (5 kW)	Pressure profiles with only 2.45 GHz source in helium gas: *Helium plasmas are the densest plasmas on LDX.*
100804018 (levitated) [Deuterium]	28.0 GHz (10 kW)	Pressure profiles with only 28.0 GHz source: *Pressure profile is very broad ($g \sim 1.2$) and has little stored energy.*

Table 5.1: A summary of the magnetically reconstructed shots.

5.1 Comparison of plasmas during levitated and supported operation

5.1.1 Overview of reconstructed shots

Supported shot number 100805045 and levitated shot number 100805046 are used to compare supported and levitated operation. For these shots the shot conditions were programmed to be identical with the exception that the dipole is supported in one case and levitated in the other. Because the shots occurred consecutively (within a number of minutes of each other) variations in uncontrolled parameters (i.e., vacuum wall conditioning) are minimal. Thus, these shots allow for a careful and systematic comparison between supported and levitated operation.

Figure 5.1 provides an overview of shots 100805045 and 100805046. The power and fueling are similar for the two shots; however, during levitation an outer flux loop measures twice the magnetic flux and the interferometer measures the density to be much higher and more centrally peaked. Here both shots are reconstructed at two different times: (1) with multiple ECRH sources on, and (2) with only the 2.45 GHz source on. The times with multiple ECRH sources on are are denser and likely to be more thermal, with less neutral penetration from the edge. The times with only the 2.45 GHz heating source are of interest because there is a more significant difference between supported and levitated operation with just this source (see fig. 5.7).

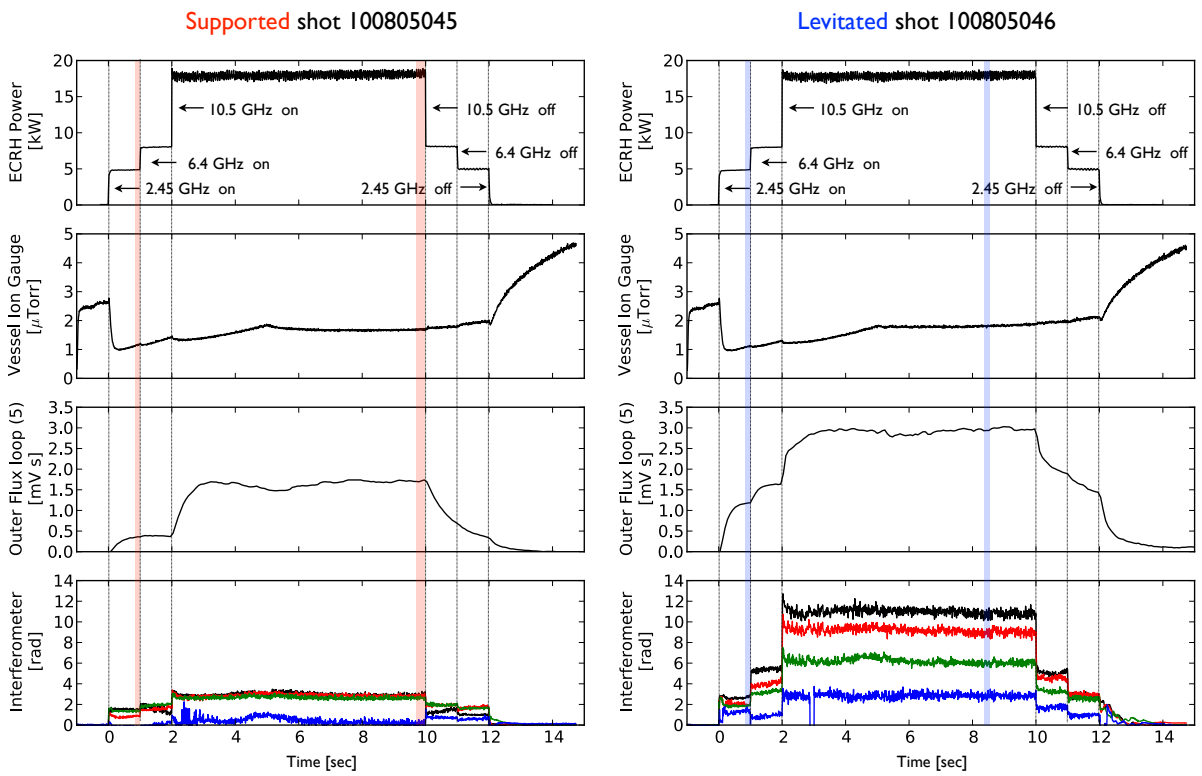

Figure 5.1: Overview of supported shot 100805045 and levitated shot 100805046. The top row shows that the heating power profile was the same in both shots. The second row shows that the vessel pressure was similar on both shots. The third row shows that during levitation the change in the magnetic flux measured by a flux loop at the outer mid-plane (diameter 5 m) is nearly a factor of two greater than during supported operation. The last row shows the phase measurement of the 4 chord interferometer: black (77 cm tangency radius), red (86 cm), green (96 cm), and blue (125 cm). The large phase change on the inner chords during levitation show that the electron density is much higher and centrally peaked during levitated operation. The light red and light blue vertical lines indicate the times used in the reconstructions described in the next sections. The vertical black lines mark times when the input power changes.

5.1.2 Pressure profiles with 2.45 GHz, 6.4 GHz, and 10.5 GHz ECRH sources (18 kW)

The electron pressure profile is broader when the F-coil is levitated than it is when the F-coil is supported. Figure 5.2 shows that the steepness parameter, g, is about 2 when the F-coil is levitated and multiple ECRH sources are on. The figure shows the value of χ^2 as a function of the parameters g and the location of the pressure peak for a fixed value of the pressure anisotropy ($a_0 = 0.5$). Small values of χ^2 (blue) indicate good agreement between the measurement and model. The yellow contours mark levels of constant χ^2 and show that there is a constrained minimum. Figure 5.3 shows that the estimated error in the measurement of g is about ± 0.2 based on a Monte Carlo simulation of the parameter errors. Thus, the estimated value of g for this shot is 2.1 ± 0.2. Figures 5.4(a) and 5.4(b) show that the magnetic reconstruction tends toward anisotropic pressure profiles; however, fig. 5.4(a) shows g does not vary strongly with the anisotropy factor and has a value between 2 and 2.2 for anisotropy factors from 0 to 2. Figure 5.5 shows that for a supported plasma with multiple ECRH sources $g > 5$ indicating a very steep pressure profile. Table 5.2 compares both the model and plasma parameters for supported and levitated operation. Figure 5.6 shows contour plots of the pressure and current density profiles for both levitated and supported operation.

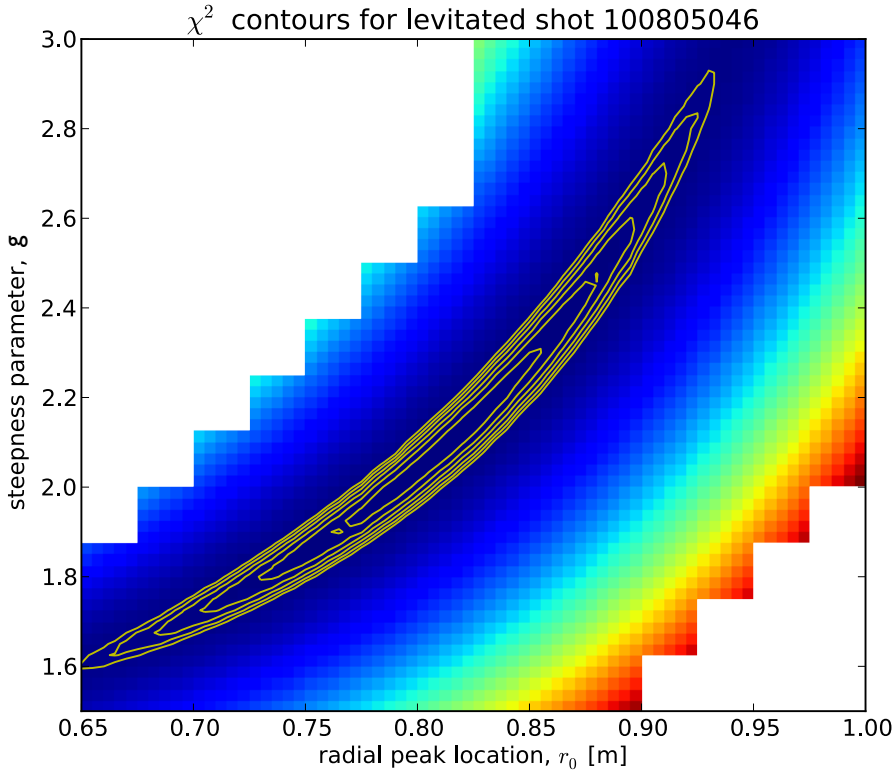

Figure 5.2: χ^2 contours for levitated shot 100805046 with multiple ECRH sources on. The underlaid image shows the χ^2 values with blue indicating small χ^2 and red indicating large χ^2. The contours of minimum χ^2 are closed and indicate a that the pressure profile has its peak at about 80 cm and has a steepness parameter, g, of about 2.

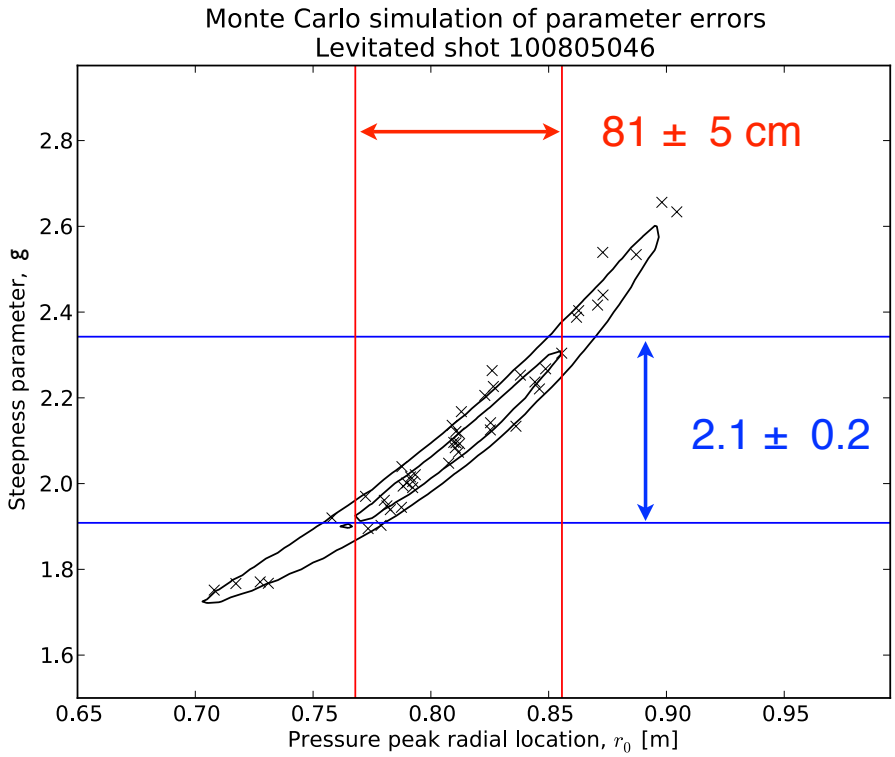

Figure 5.3: Monte Carlo simulation of parameter errors for levitated shot 100805046. The value of the steepness parameter is 2.1 with a standard deviation of about 0.2. The black contours mark values of constant χ^2. The inner contour is defined by $\chi^2 = \chi^2_{min} + \delta\chi^2$ where $\chi^2_{min} = 19.4$ and $\delta\chi^2 = 0.9$.

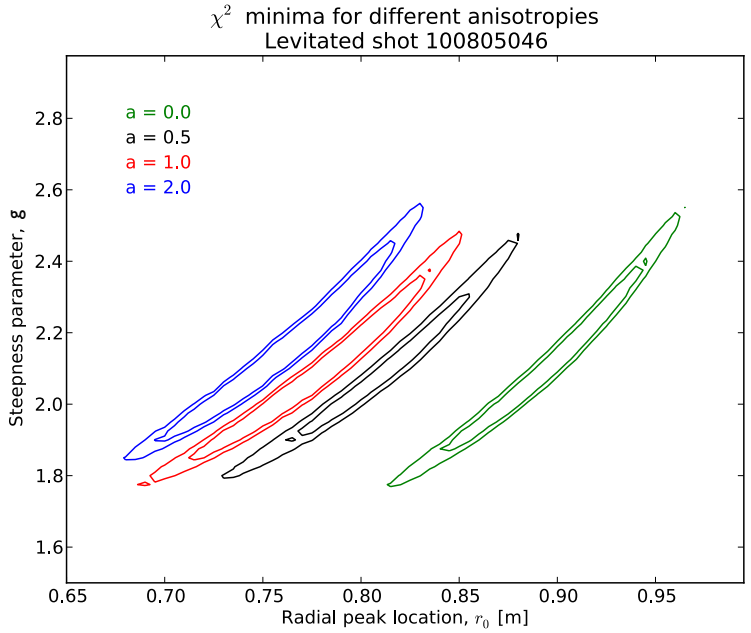

(a)

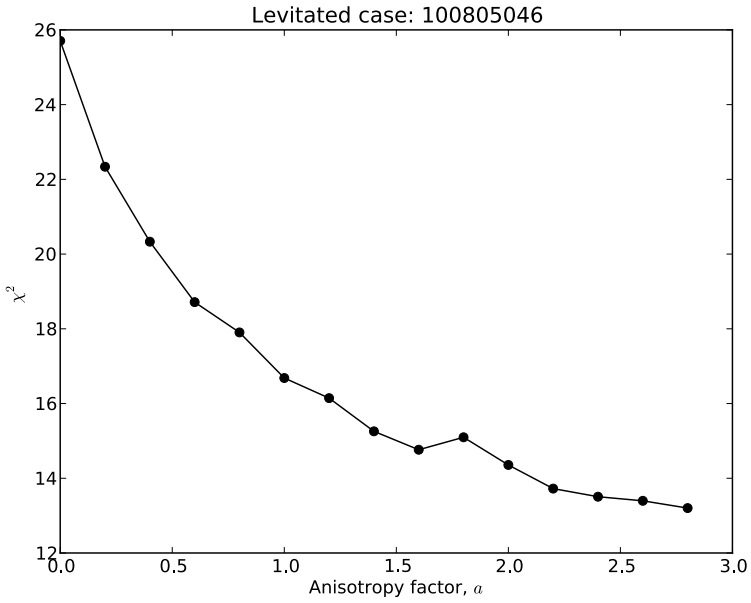

(b)

Figure 5.4: Variation of χ^2 minima with anisotropy factor for levitated plasma shot 100805046. (a) Contours illustrating how the χ^2 minimum moves in the parameter space for different values of the anisotropy parameter. (b) A scan of the anisotropy parameter showing that the model and minimization algorithm tend toward large anisotropy parameters.

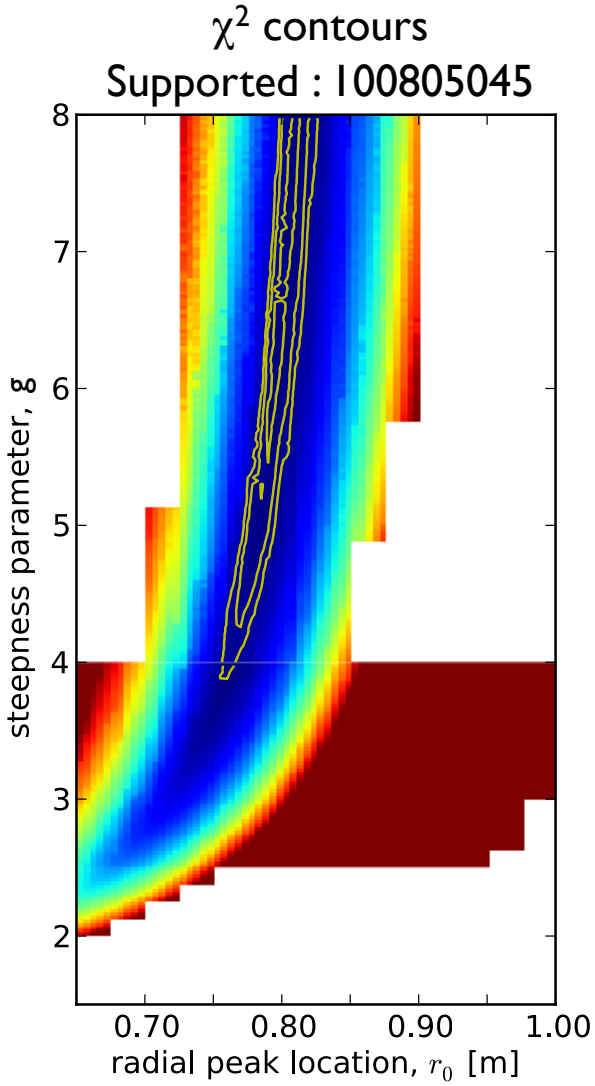

Figure 5.5: χ^2 contours for supported shot 100805045 with multiple ECRH sources on. The underlaid image shows the χ^2 values with blue indicating small χ^2 and red indicating large χ^2. The contours of minimum χ^2 indicate a steepness parameter of greater than 5. The anisotropy is fixed in the minimization to the value of 2.

Model Parameters	Levitated (100805046) t = 8.2 sec	Supported (100805045) t = 9.5 sec
Pressure parameter, p_0	426 Pa	4430 Pa
Pressure peak location, r_0	0.81 m	0.80 m
Profile steepness parameter, g	2.1	6.3
Anisotropy parameter, a	0.5†	2.0†
Upper mirror inner current, I_{M1}	-1 A	-2630 A
Upper mirror outer current, I_{M2}	-155 A	-6 A
Plasma Parameters	Levitated (100805046)	Supported (100805045)
Peak pressure	268 Pa	880 Pa
Plasma energy	250 J	196 J
Beta at pressure peak	8.6 %	27.2 %
Total plasma current	3.0 kA	2.4 kA
Plasma dipole moment	12.1 $kA \cdot m^2$	7.1 $kA \cdot m^2$
Global energy confinement	14 ms	11 ms

Table 5.2: Pressure profile parameters and plasma parameters for magnetic reconstructions of levitated shot 100805046 and supported 100805045 with multiple ECRH sources on (18 kW). The global energy confinement time is the plasma energy divided by the total microwave input power.
† Parameter held fixed during χ^2 minimization.

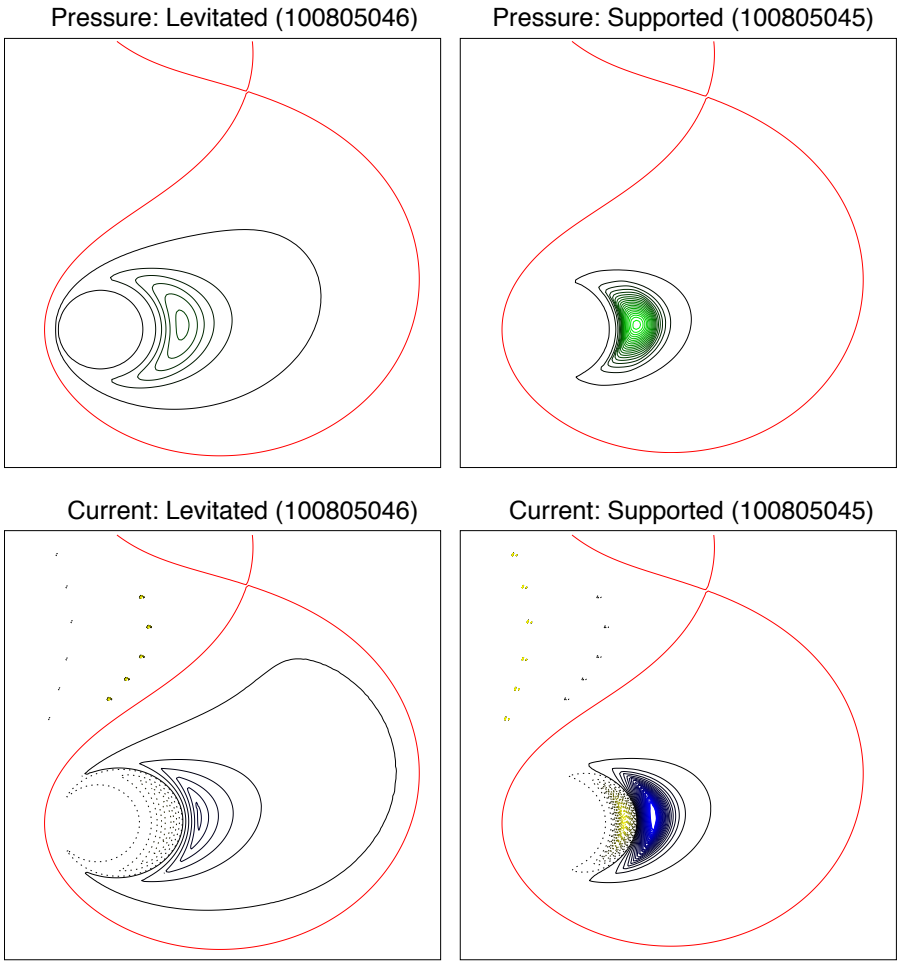

Figure 5.6: Pressure and current density contours for a supported (100805045) and a levitated (100805046) shot. In the top figures the pressure is shown with green contours indicating higher pressure and black contours indicating lower pressure (the same pressure contours levels are plotted for levitated and supported operation). The bottom figures show the current density with solid blue indicating high positive current density, solid black low positive current density, dotted black low negative current density, and dotted yellow high negative current density (the same current density contour levels are plotted in levitated and supported operation). The red contour marks the separatrix. During levitation the pressure and current density profiles are broader with lower maximum values.

5.1.3 Pressure profiles with only 2.45 GHz ECRH source (5 kW)

Magnetic reconstruction of the pressure profile during supported operation with only the 2.45 GHz source provides the opportunity to compare the new magnetic reconstruction code with previous work [43]. The reconstructed pressure profile is consistent with previous work. Figure 5.8(a) shows that the pressure profile is steep ($g \sim 3.5$) with its peak near the 2.45 GHz fundamental resonance located at 82 cm. Figure 5.8(b) shows that during levitation the pressure profile has a steepness parameter similar to that in supported operation but the pressure peak has moved out in radius.

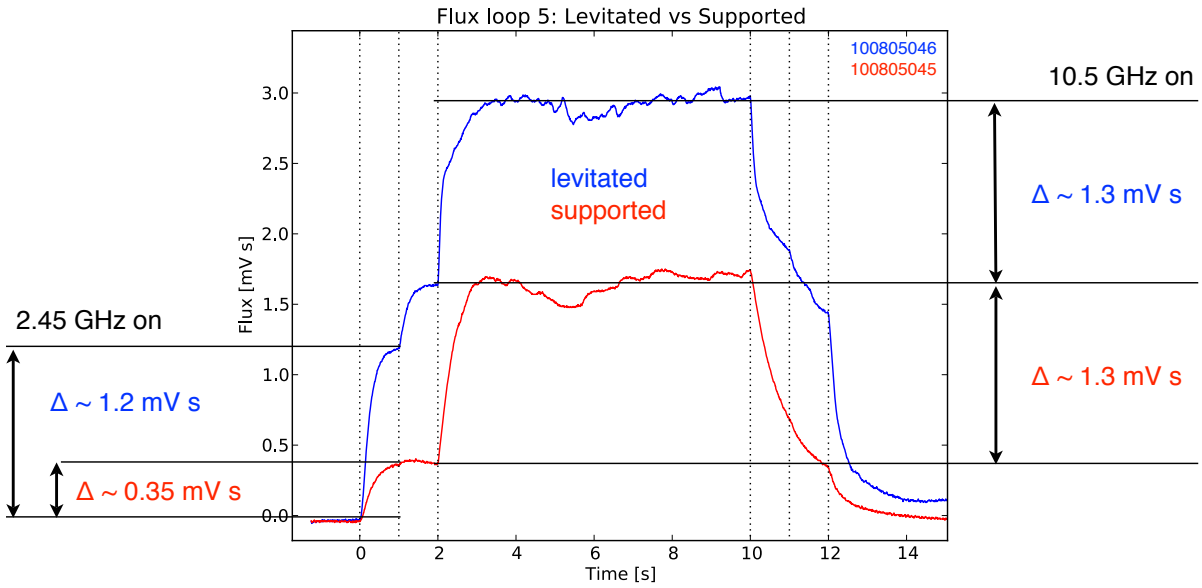

Figure 5.7: Comparison of the flux measured by flux loop 5 for a levitated and supported shot. Levitation makes a significant difference when the 2.45 GHz source is turned on at t = 0 s. By contrast levitation does not appear to make a significant difference when the 10.5 GHz source is turned on a t = 2 s. This is likely a result of the pressure peak moving out in radius as a result of the 2.45 GHz fundamental resonance being shielded by the increased density during levitation. Another factor maybe that the 2.45 GHz source has its first mid-plane resonance (its fundamental) on closed field lines during levitation while the 10.5 has its first mid-plane resonance (its 1st harmonic) on open field lines (field lines that connect to the F-coil).

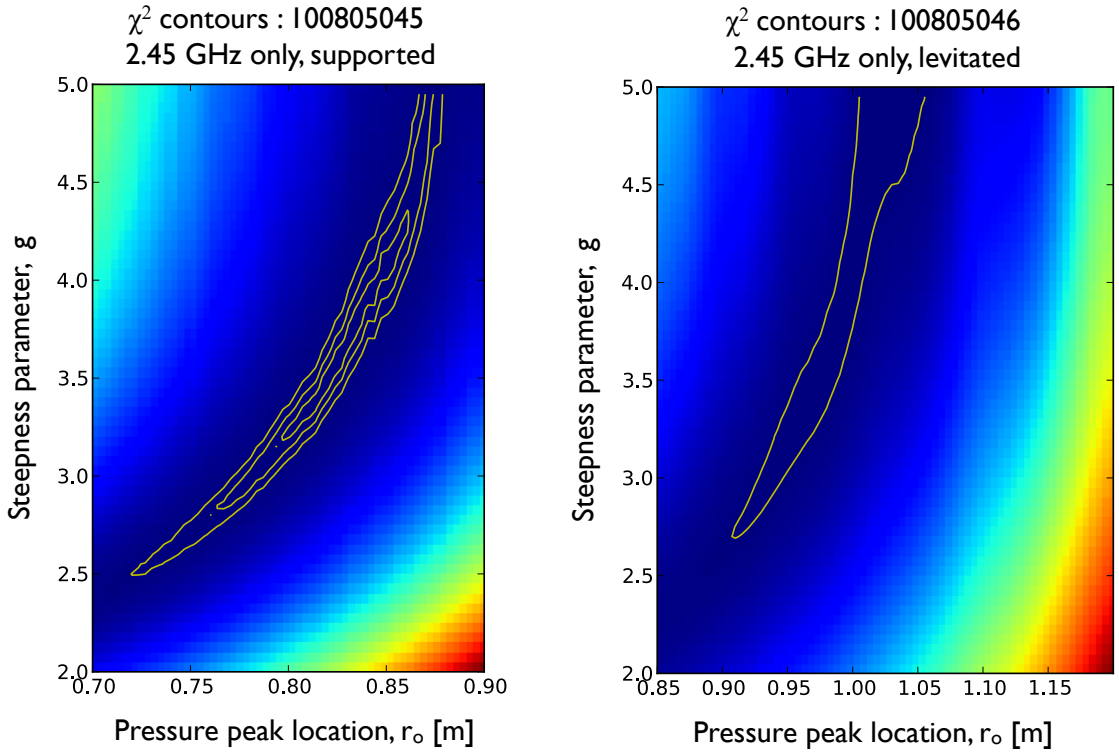

(a) (b)

Figure 5.8: Comparison of levitated and supported operation with only the 2.45 GHz source. (a) Supported shot 100805045. The pressure profile is steep and peaks near the fundamental resonance of the 2.45 GHz source. (b) Levitated shot 100805046. The pressure profile is broader and peaks at larger radius possibly because the increased density during levitation has cutoff access to the 2.45 GHz fundamental resonance.

5.2 Levitated, high density electron pressure profiles

5.2.1 10.5 GHz ECRH source with and without 28 GHz ECRH source (10 kW and 5 kW)

Figure 5.11 shows an overview of a shot with the 10.5 GHz heating source during which the 28 GHz source is turned on and off. The 28 GHz heating source increases the plasma density an amount similar to the 10.5 GHz heating source; however, it has a much smaller effect on the

magnetic flux measured by an outer flux loop (the large rise in the flux that peaks at about 2 seconds is due primarily to the movement of the F-coil). Figures 5.10(a) and 5.10(b) show magnetic reconstructions of the pressure profile at times with (6.25 seconds) and without (11.5 seconds) the 28 GHz heating source on. With the addition of the 28 GHz heating source the pressure peak moves slightly inward and the steepness parameter, g, decreases from about 3.5 to 2.5 indicating a broadening of the pressure profile.

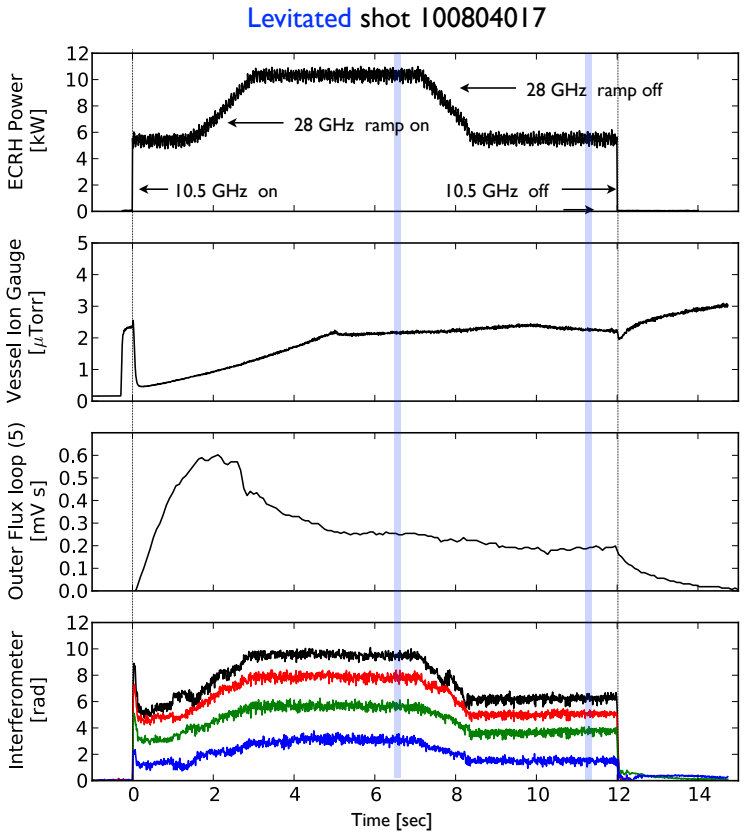

Figure 5.9: Overview of a 10.5 GHz shot (100804017) with and without the addition of the 28 GHz source. Magnetic reconstructions of the pressure profile at 6.25 seconds and 11.5 seconds (indicated by the light blue lines) show that the pressure profile is broader when the 28 GHz source is on in addition to the 10.5 GHz source.

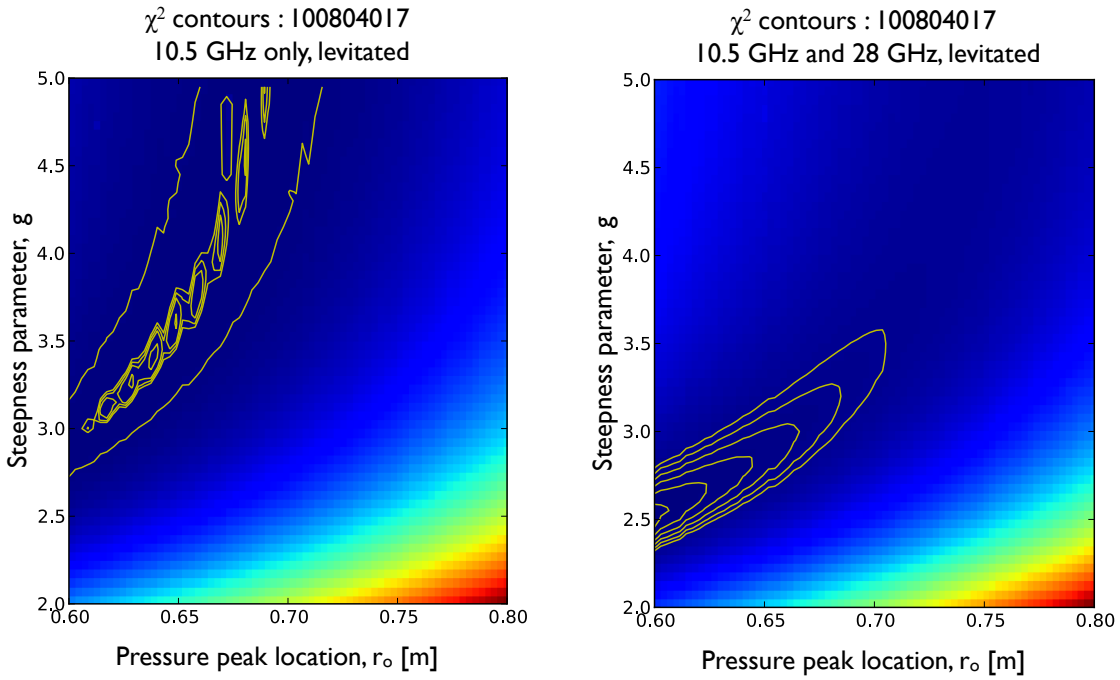

(a) (b)

Figure 5.10: Comparison of levitated plasmas with and without the 28 GHz. Levitated shot 100804017 with (a) 10.5 GHz source (5 kW) only and (b) 10.5 GHz source (5 kW) and 28 GHz source (5 kW)

Model Parameters	with 28 GHz source t = 6.25 sec	without 28 GHz source t = 11.5 sec
Pressure parameter, p_0	854 Pa	967 Pa
Pressure peak location, r_0	0.60 m	0.64 m
Profile steepness parameter, g	2.5	3.5
Anisotropy parameter, a	2.0†	2.0†
Upper mirror inner current, I_{M1}	-404 A	-160 A
Upper mirror outer current, I_{M2}	0† A	0† A
Plasma Parameters	with 28 GHz source	without 28 GHz source
Peak pressure	530 Pa	515 Pa
Plasma energy	56 J	55 J
Beta at pressure peak	2 %	3%
Total plasma current	0.44 kA	0.45 kA
Plasma dipole moment	1.1 $kA \cdot m^2$	1.0 $kA \cdot m^2$
Global energy confinement	6 ms	11 ms

Table 5.3: Pressure profile parameters and plasma parameters for magnetic reconstructions of levitated shot 100804017 for times with (10 kW total ECRH power) and without (5 kW total ECRH power) the 28 GHz source.
† Parameter held fixed during χ^2 minimization.

5.2.2 Full ECRH power (28 kW)

Full power shots on LDX have 28 kW of power distributed over 4 frequencies ranging from 2.45 GHz to 28 GHz. The density during levitated full power shots can exceed 1×10^{12} cm^{-3}. Figure 5.11 shows shot 100805028 in which the 28 GHz source is abruptly turned off (typically the 28 GHz source must be slowly ramped up and down). Shutting off the 28 GHz source causes an abrupt decrease in the plasma density, although, as in shown in fig. 5.12 the invariant density profile is maintained. Notably, the diamagnetic flux actually increases when the the 28 GHz source is shut off though a closer look at the shut off reveals that the diamagnetic flux initially decreases briefly before increasing.

Magnetic reconstructions of the pressure profile before and after the shut off of the 28 GHz heating source show that the pressure profile is broader when all power sources are on; the pressure profile becomes steeper after the 28 GHz source is turned off (see table 5.4 and fig. 5.14). Figures 5.15(a) and 5.15(b) show the time evolution of the pressure profile around the shut off as the pressure profile smoothly transitions from a broad pressure profile ($g \sim 1.6$) to a steeper pressure profile ($g > 2$).

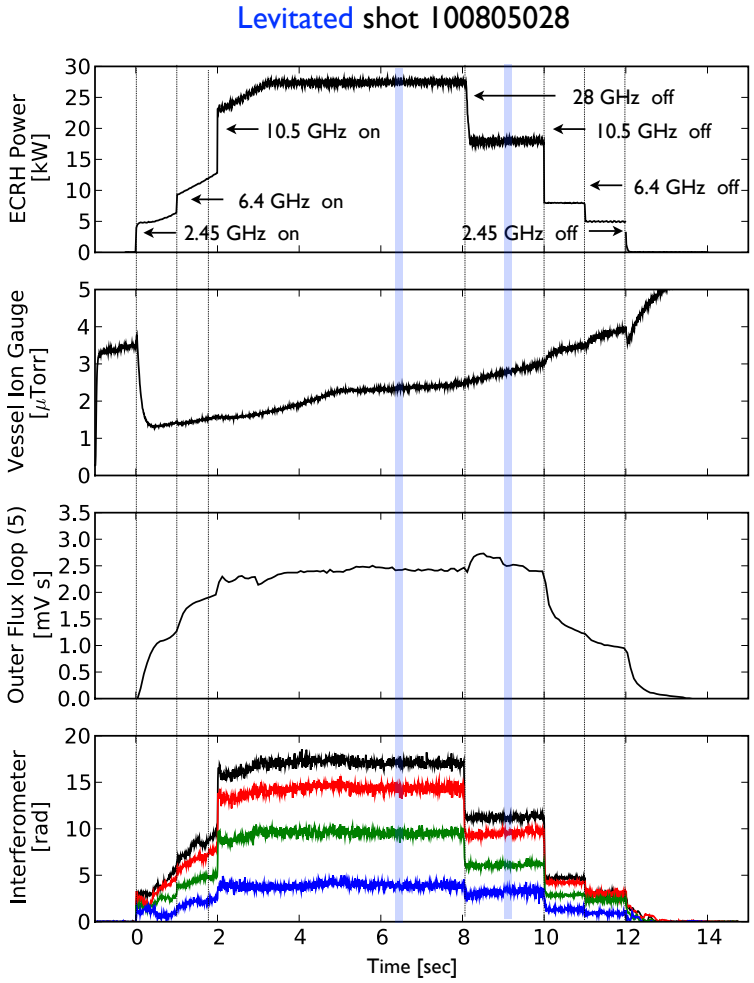

Figure 5.11: Overview of full power shot 100805028. At 8 seconds the 28 GHz source is turned off. Magnetic reconstructions of the pressure profile at 6.25 seconds and 9.1 seconds (indicated by the light blue lines) show that the pressure profile is much broader ($g = 5/3$) when the 28 GHz source is on in addition to the other sources.

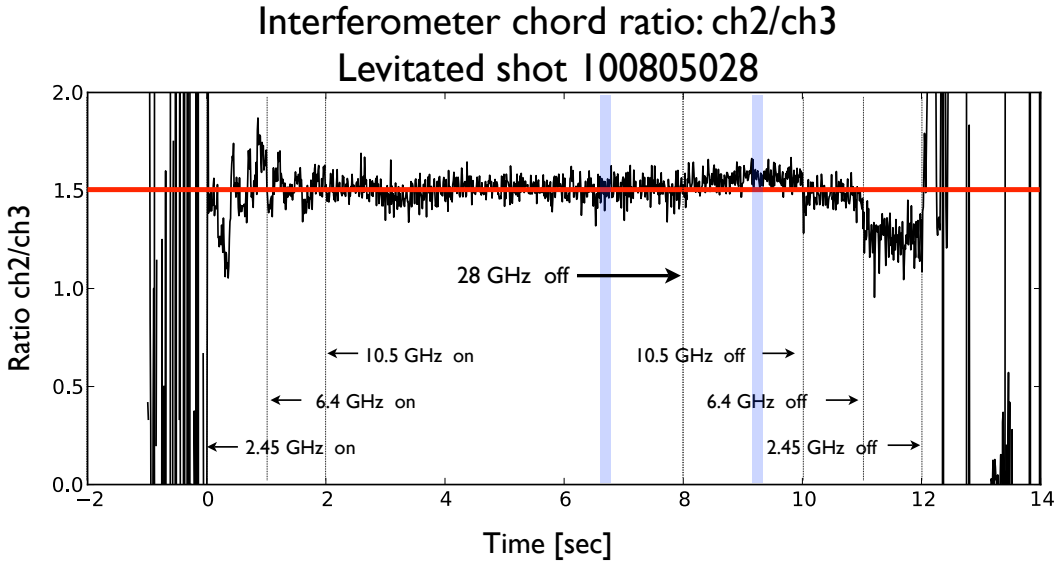

Figure 5.12: For an invariant density profile on LDX the ratio of 2^{nd} and 3^{rd} interferometer chord phase measurement is approximately 1.5. The plasma maintains a chord ratio consistent with an invariant density profile even when a sudden turn off of the 28 GHz source (10 kW) causes a dramatic reduction in the the absolute density (see fig. 5.11 bottom panel).

Model Parameters	with 28 GHz source t = 6.25 sec	without 28 GHz source t = 9.1 sec
Pressure parameter, p_0	200 Pa	222 Pa
Pressure peak location, r_0	0.83 m	0.95 m
Profile steepness parameter, g	1.55	2.45
Anisotropy parameter, a	2.0†	2.0†
Upper mirror inner current, I_{M1}	-2042 A	-1786 A
Upper mirror outer current, I_{M2}	-397 A	-408 A
Plasma Parameters	with 28 GHz source	without 28 GHz source
Peak pressure	178 Pa	185 Pa
Plasma energy	116 J	109 J
Beta at pressure peak	7.0 %	19.5%
Total plasma current	1.5 kA	1.7 kA
Plasma dipole moment	7.9 $kA \cdot m^2$	9.2 $kA \cdot m^2$
Global energy confinement	4 ms	6 ms

Table 5.4: Pressure profile parameters and plasma parameters for magnetic reconstructions of levitated shot 100805028 for times with and without the 28 GHz source.
† Parameter held fixed during χ^2 minimization.

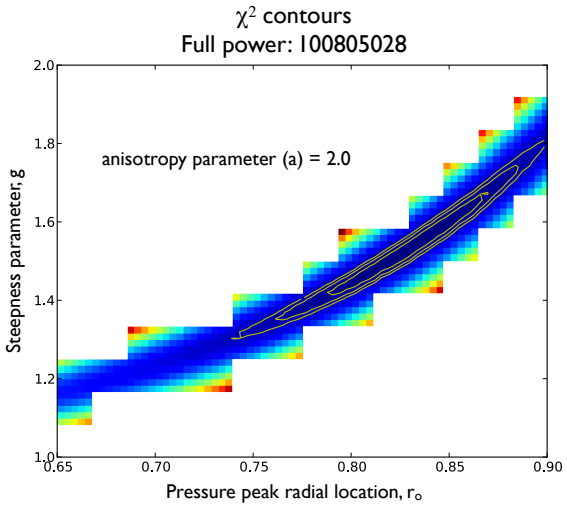

(a)

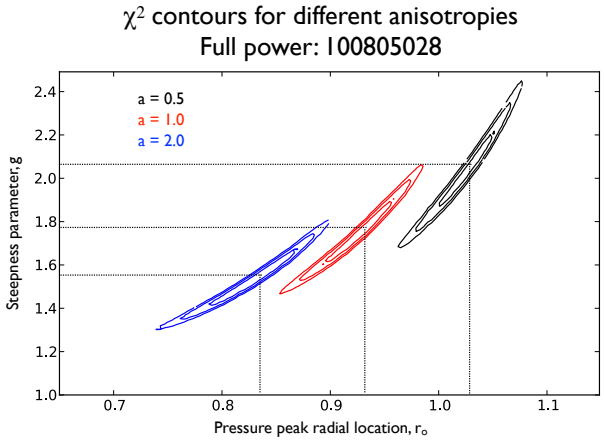

(b)

Figure 5.13: (a) χ^2 contours for magnetic reconstruction of a shot (100805028) with full ECRH power (28 kW) and with the anisotropy factor fixed at a value of 2. (b) χ^2 contours for different anisotropy factors. The magnetics agree best with the larger anisotropy factor ($a_o = 2.0, \chi^2 \sim 25$ whereas $a_o = 0.5, \chi^2 \sim 41$) indicating that even when levitated LDX plasmas are anisotropic. Comparing this shot (100805028) to the shot in a previous section (100805046, fig. 5.2) the addition of the 10 kW at 28 GHz increases the plasma density and causes the pressure profile to broaden toward the invariant profile.

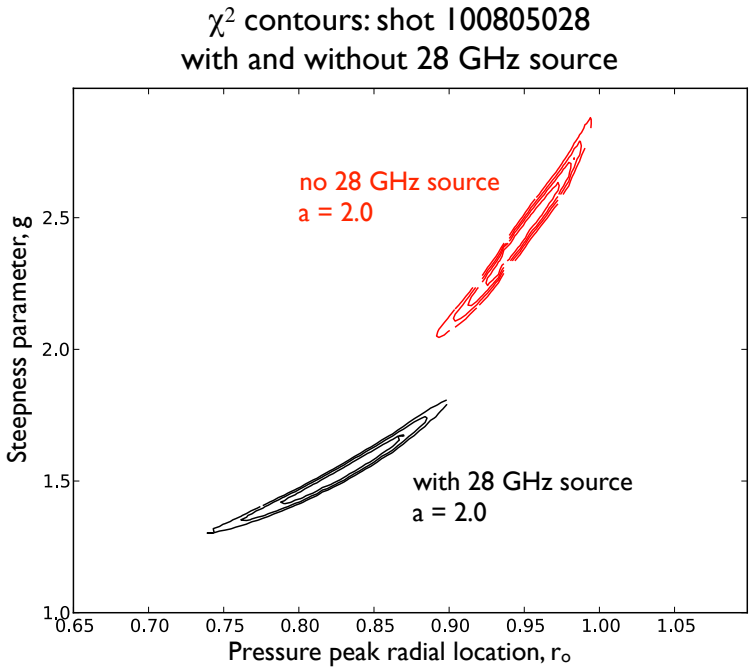

Figure 5.14: χ^2 contours comparing levitated plasmas with and without the 28 GHz source (10 kW). The 28 GHz source (10 kW) significantly increases the plasma density. Magnetic reconstructions indicate that the pressure profile is broader with the 28 GHz source on. This is shown by the smaller value of the steepness parameter determined by the magnetic reconstructions when the 28 GHz source is on.

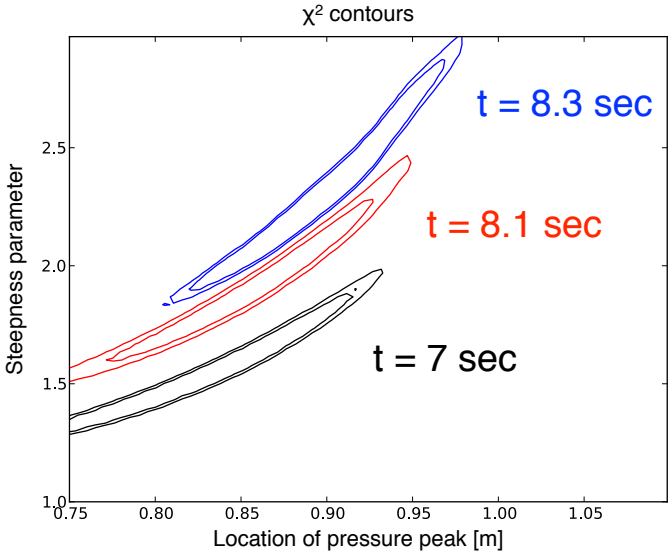

(a)

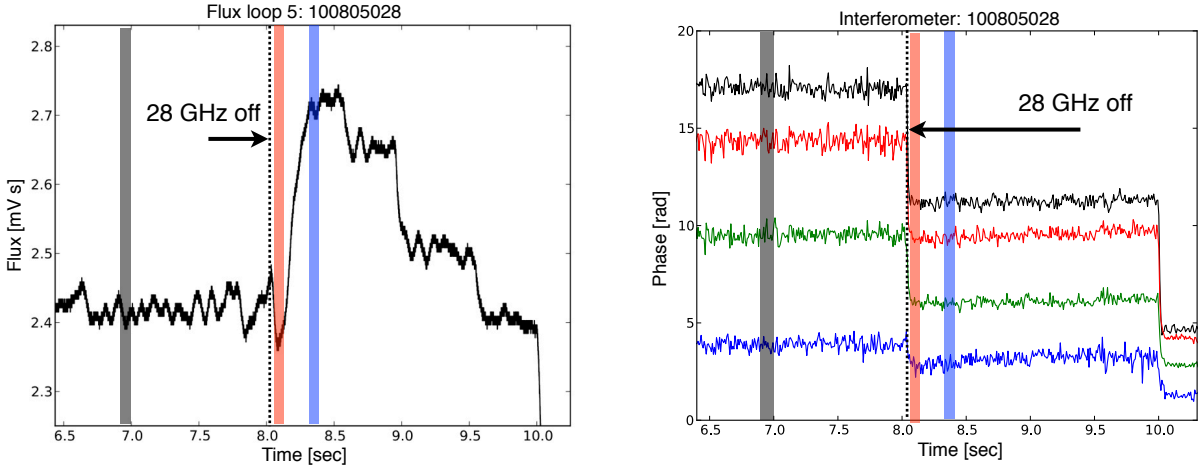

(b)

Figure 5.15: (a) χ^2 contours showing time evolution of the pressure profile with the 28 GHz source shutoff. (a) Time traces showing the magnetic flux measured at and outside flux loop and the phase measurement made by the interferometer. At 8 seconds the 28 GHz source shuts off causing a rapid decrease in the density measured by the interferometer. The grey, red, and blue vertical bars indicate times when the magnetic reconstructions where done. With the 28 GHz source on the pressure profile is near the invariant profile. When the 28 GHz source is turned off the pressure profile steepens, which would be consistent with a building hot electron population.

5.2.3 Helium plasma (2.45 GHz ECRH only, 5 kW)

Helium plasmas on LDX are typically denser (by about a factor of 2) than deuterium plasmas. Magnetic reconstruction of the pressure profile for a helium shot with just the 2.45 GHz source shows that the pressure profile steepness parameter, g, is approximately 1.5 (see fig. 5.16). Additionally, the plasma is very isotropic as indicated by the anisotropy factor ($a = 0$, see fig. 5.17). Table 5.5 shows the model and plasma parameters for the magnetic reconstruction of the helium shot for both the isotropic and anisotropic cases.

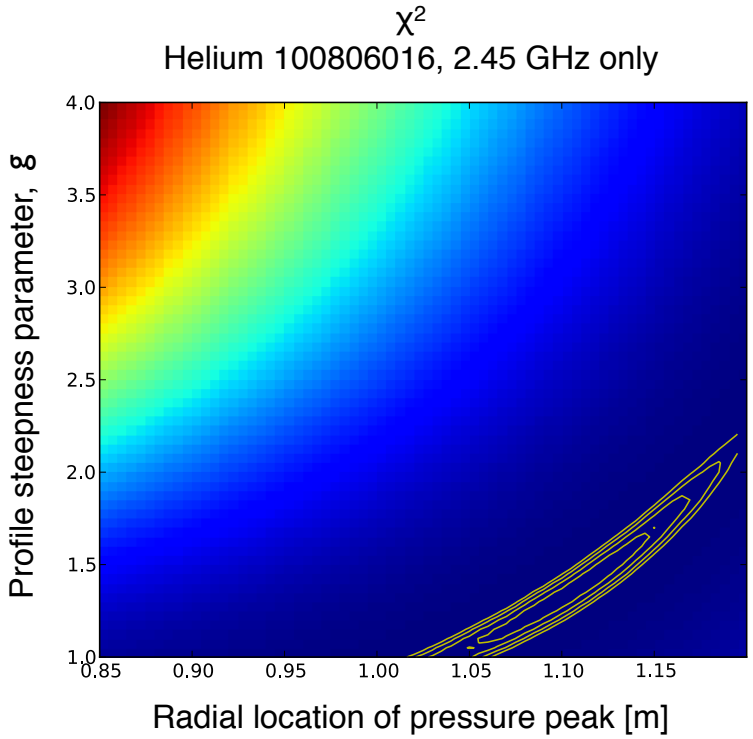

Figure 5.16: χ^2 contours indicating the best fit pressure profile parameters for a helium shot with just the 2.45 GHz source. The steepness parameter, g, is about 1.5.

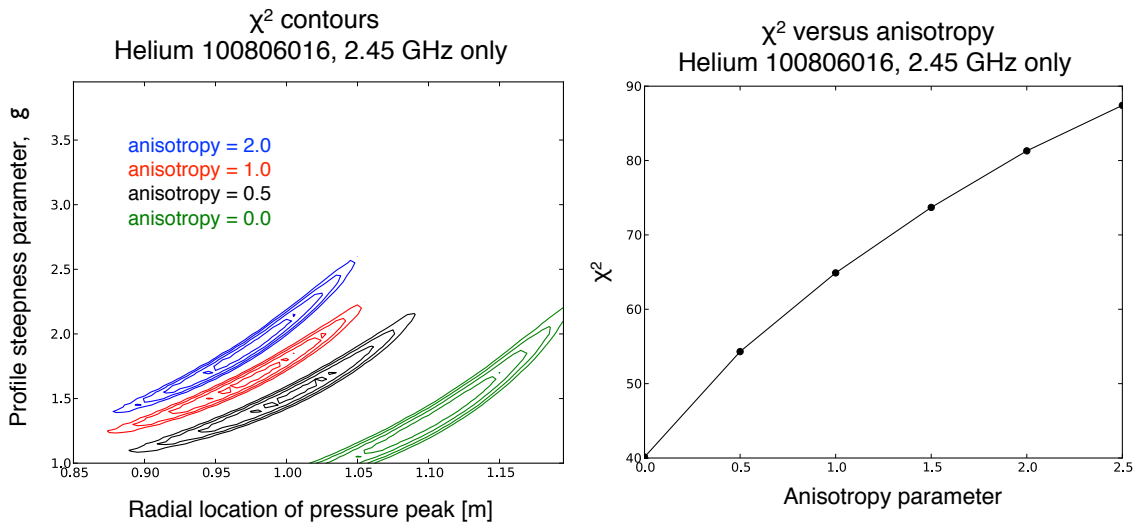

Figure 5.17: χ^2 contours indicating the best fit pressure profile parameters for a helium shot with just the 2.45 GHz source for different values of the anisotropy factor. The best fit is for $a = 0$ which indicates an isotropic pressure.

Model Parameters	Isotropic ($a = 0$) t = 11.9 sec	Anisotropic ($a = 0.5$) t = 11.9 sec
Pressure parameter, p_0	9 Pa	20 Pa
Pressure peak location, r_0	1.10 m	1.01 m
Profile steepness parameter, g	1.4	1.55
Anisotropy parameter, a	0.0†	0.5†
Upper mirror inner current, I_{M1}	0 A†	0 A†
Upper mirror outer current, I_{M2}	-159 A	-161 A
Plasma Parameters	**Isotropic ($a = 0$)**	**Anisotropic ($a = 0.5$)**
Peak pressure	9 Pa	18 Pa
Plasma energy	50 J	42 J
Beta at pressure peak	2.4 %	2.8 %
Total plasma current	0.53 kA	0.55 kA
Plasma dipole moment	3.2 $kA \cdot m^2$	3.2 $kA \cdot m^2$
Global energy confinement	10 ms	8 ms

Table 5.5: Pressure profile parameters and plasma parameters for magnetic reconstructions of levitated helium shot 100806016 with only the 2.45 GHz ECRH source on.
† Parameter held fixed during χ^2 minimization.

5.2.4 28 GHz ECRH source only (10 kW)

Figure 5.18 shows that the 28 GHz heating source creates a peaked density profile (similar to other ECRH sources) but little diamagnetic flux (compared to other ECRH sources). Figure 5.19 shows that the density profile is near the invariant profile for most of the shot. Magnetic reconstructions of the pressure profile show that the pressure profile is very broad with $g < 1.5$. Figure 5.20(a) shows that for an isotropic pressure the steepness parameter is very broad ($g \sim 1.2$) with a pressure peak near the F-coil. Figure 5.20(b) shows that for a more anisotropic pressure the profile is steeper ($g \sim 1.5$). Importantly, table 5.6 shows that there is less plasma stored energy per heating power during levitation with only the 28 GHz heating source.

Model Parameters	28 GHz only, ($a = 0.0$) t = 8.5 sec	28 GHz only, ($a = 2.0$) t = 8.5 sec
Pressure parameter, p_0	15 Pa	67 Pa
Pressure peak location, r_0	0.6 m	0.6 m
Profile steepness parameter, g	1.2	1.5
Anisotropy parameter, a	0.0†	2.0†
Upper mirror inner current, I_{M1}	65 A	63 A
Upper mirror outer current, I_{M2}	0† A	0† A
Plasma Parameters	28 GHz only, ($a = 0.0$)	28 GHz only, ($a = 2.0$)
Peak pressure	13 Pa	56 Pa
Plasma energy	13 J	11 J
Beta at pressure peak	0.05 %	0.2 %
Total plasma current	0.12 kA	0.12 kA
Plasma dipole moment	0.4 $kA \cdot m^2$	0.4 $kA \cdot m^2$
Global energy confinement	1 ms	1 ms

Table 5.6: Pressure profile parameters and plasma parameters for magnetic reconstructions of levitated shot 100804018 for times with only the 28 GHz source.
† Parameter held fixed during χ^2 minimization.

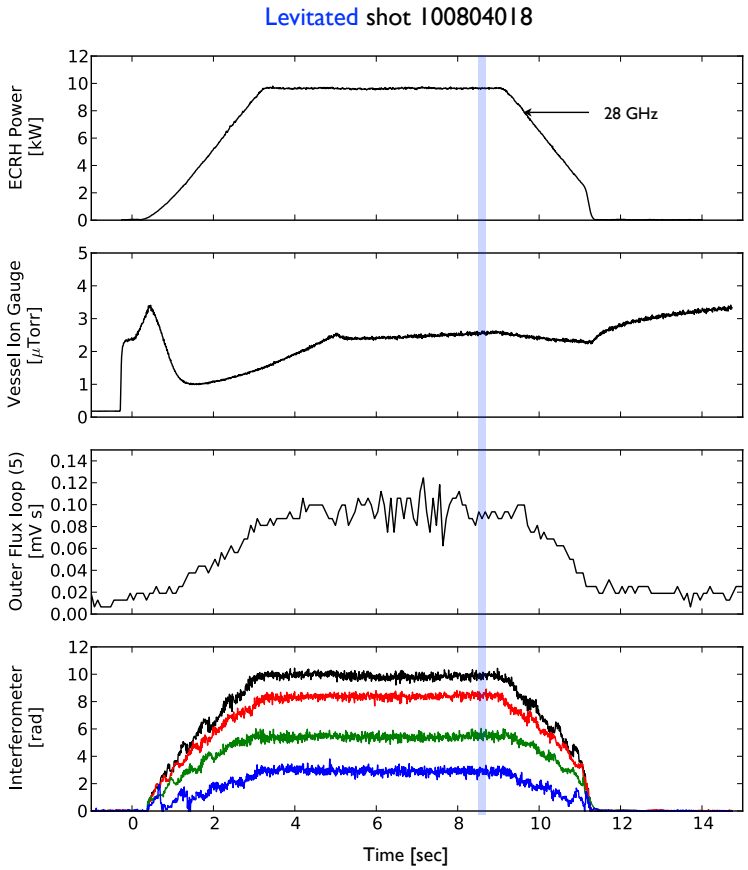

Figure 5.18: Overview of 28 GHz source only shot 100804018. The interferometer shows that the 28 GHz source creates significant density and the density adopts an invariant profile. However, flux loop measurements show little change in the magnetic flux indicating little plasma current. Magnetic reconstruction of the pressure profile at 8.5 seconds (indicated by the light blue line) shows that there is little plasma pressure though the pressure adopts a profile with a gradient slightly more shallow than the invariant profile.

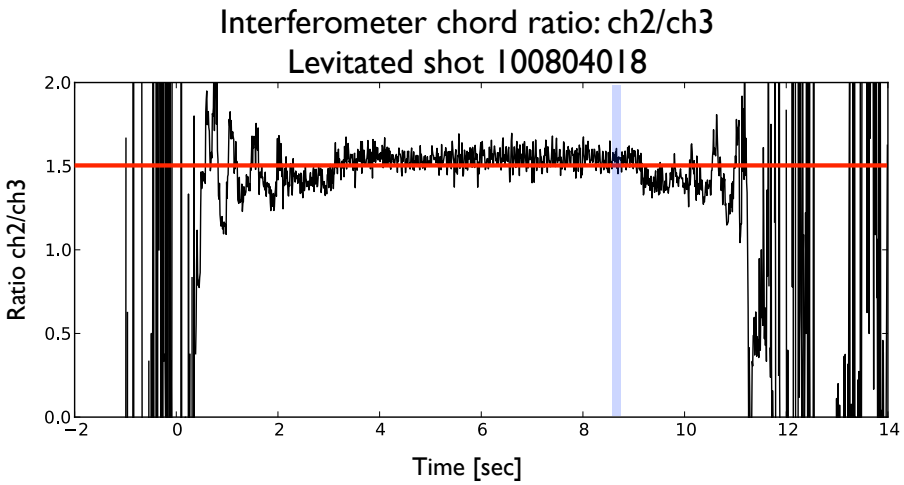

Figure 5.19: For an invariant density profile ($n \propto 1/V$) on LDX the ratio of 2^{nd} and 3^{rd} interferometer chord phase measurement is approximately 1.5. This ratio shows that with only the 28 GHz source on (shot 100804018) the density profile adopts the invariant profile.

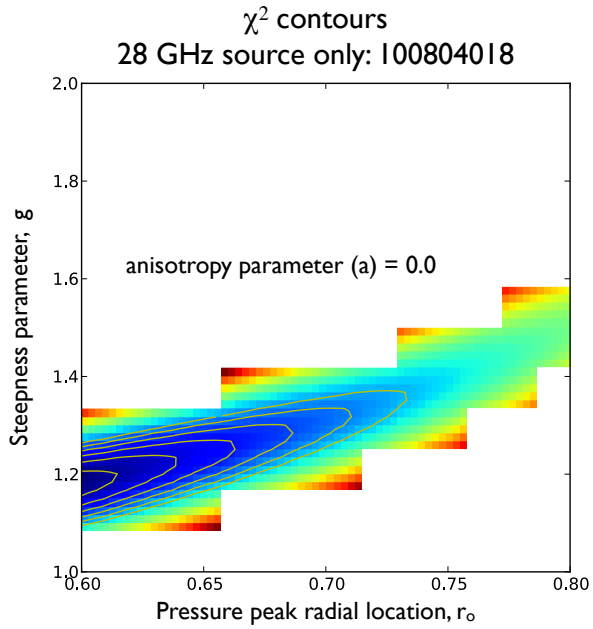

(a)

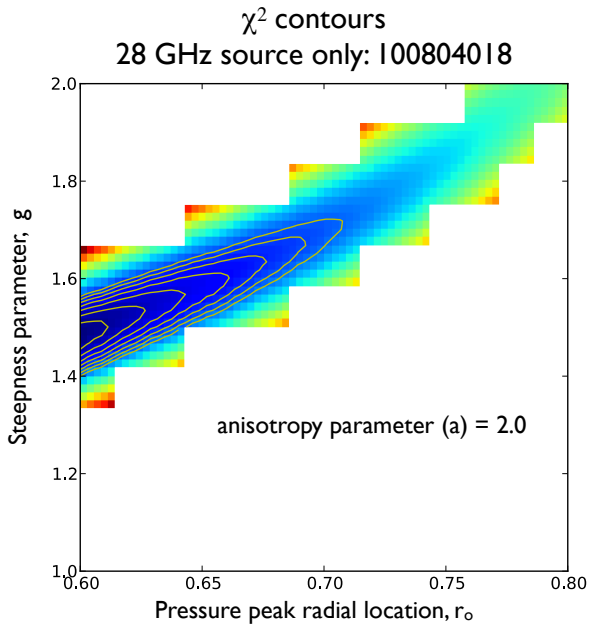

(b)

Figure 5.20: χ^2 contours for levitated shot 100804018 with only the 28 GHz source on. The underlaid image shows the χ^2 values with blue indicating small χ^2 and red indicating large χ^2 for (a) an anisotropy factor of 0.0 and (b) an anisotropy factor of 2.0. For both cases the contours of minimum χ^2 indicate a broad profile.

Chapter 6

X-ray measurements

On LDX the X-rays appear to come primarily from a minority hot electron population. The X-ray measurements indicate that the hot electrons can be described by a log-linear energy distribution in the range 50-100 keV. Additionally, the X-ray measurements provide information about the radial location of the hot electron peak and provide a means for estimating the hot electron fraction (n_{eh}/n_e, where n_{eh} is the hot electron density and n_e is the total electron density). On LDX the X-ray spectrum from 2-20 keV (often called soft X-rays in contrast hard X-rays which have greater energy) is observed with a silicon drift detector. Higher energy X-rays (10-650 keV) are observed with several cadmium-zinc-telluride detectors.

6.1 Thermal bremsstrahlung

Bremsstrahlung, which is German for 'braking radiation', most commonly refers to the radiation emitted when electrons are slowed down in matter, such as in the X-ray tubes first discovered by Wilhelm Röntgen. However, it technically refers to all radiation emitted by ac-

celerated charged particles including cyclotron radiation and thermal bremsstrahlung. Thermal bremsstrahlung, sometimes referred to as free-free radiation, occurs in plasmas where collisions between free electrons and ions produce radiation. The thermal bremsstrahlung spectrum is a continuum

$$P_{brem}(\omega) \propto \frac{n_e n_i}{\sqrt{T_e}}\, e^{-\hbar\omega/T_e} \tag{6.1}$$

where n_e is the electron density, n_i is the ion density, T_e is the electron temperature, $\hbar$ is the reduced Planck's constant ($h/2\pi$), and ω is the light frequency. The intensity of the bremsstrahlung emission has an exponential dependence on the electron temperature. When $\hbar\omega > T_e$, the electron temperature can be deduced by fitting a line to the logarithm of the bremsstrahlung intensity spectrum [77, 78].

6.2 Spectral lines

The soft X-ray spectrum has several prominent impurity lines (see fig. 6.1(a)). The chromium (5.4 keV) and iron (6.5 keV) are commonly seen in X-ray spectra since most vacuum chambers are made of stainless steel which contains both chromium and iron. The xenon impurity is less common but it was identified by multiple lines in the soft X-ray spectra (4.1 keV,4.4 keV, and 29.5 keV) and multiple lines viewed with a visible spectrometer. The presence of xenon in the machine was traced back to a experiment run in July 2009 by looking at visible spectrometer data. In July 2009, xenon plasmas were being created and a valve stuck releasing a large amount of xenon into the vacuum chamber. The argon line ($\sim$3 keV) is the least confidently identified line as there is no expected source. Another possibility for that line is silver. There is a silver strip on the F-coil that is used by the levitation lasers. However, corroborating silver lines were not identified.

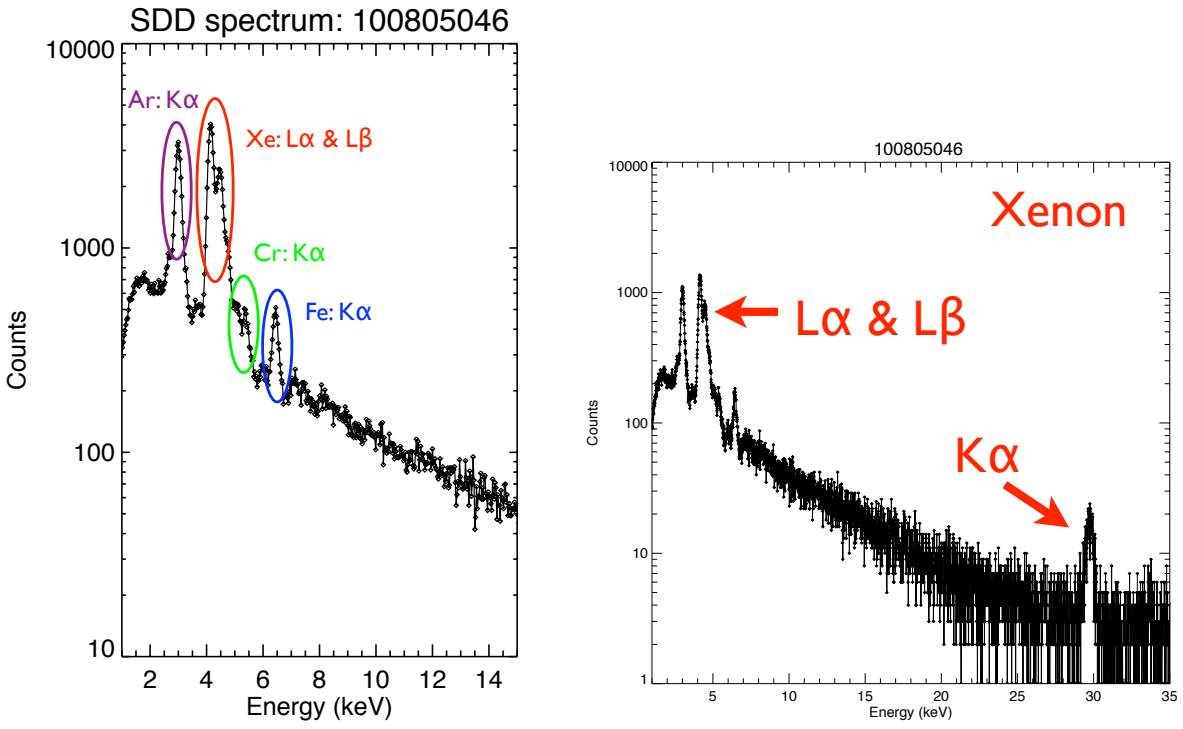

(a) (b)

Figure 6.1: (a) Impurity lines seen on LDX with SDD include xenon, chromium, iron, and argon. (b) The xenon K_α line corroborates the identification of the xenon lines seen near 4 keV.

6.3 Support versus levitated operation

The X-ray spectra in supported and levitated operation are similar. In both cases the spectra indicate the presence of a high energy electrons. Figures 6.2(a) and 6.2(b) show that this population can be fit to a pseudo-temperature in the range 50-100 keV.

Figures 6.3(a), 6.3(b) and 6.4 show that there is a variation of the X-ray spectra with the detector view's tangency radius. Specifically, fig. 6.4 shows that with just 2.45 GHz souce on the X-ray signal slightly peaks at larger radius (solid lines) during both levitated and supported operation. When higher frequency sources are turned on the X-ray signal

peaks at smaller radius (dotted lines). This is either due to the X-ray detector observing the hot electron peak in the plasma or observing target X-rays that are emitted when lost hot electrons hit the dipole magnet or its supports. The X-ray views were adjusted to get a high photon flux, rather than a narrow view (see section 3.3.2). The X-rays provide information about the energy distribution of the hot electrons, and, perhaps more importantly indicate whether there are relatively many or few hot electrons in a given plasma shot.

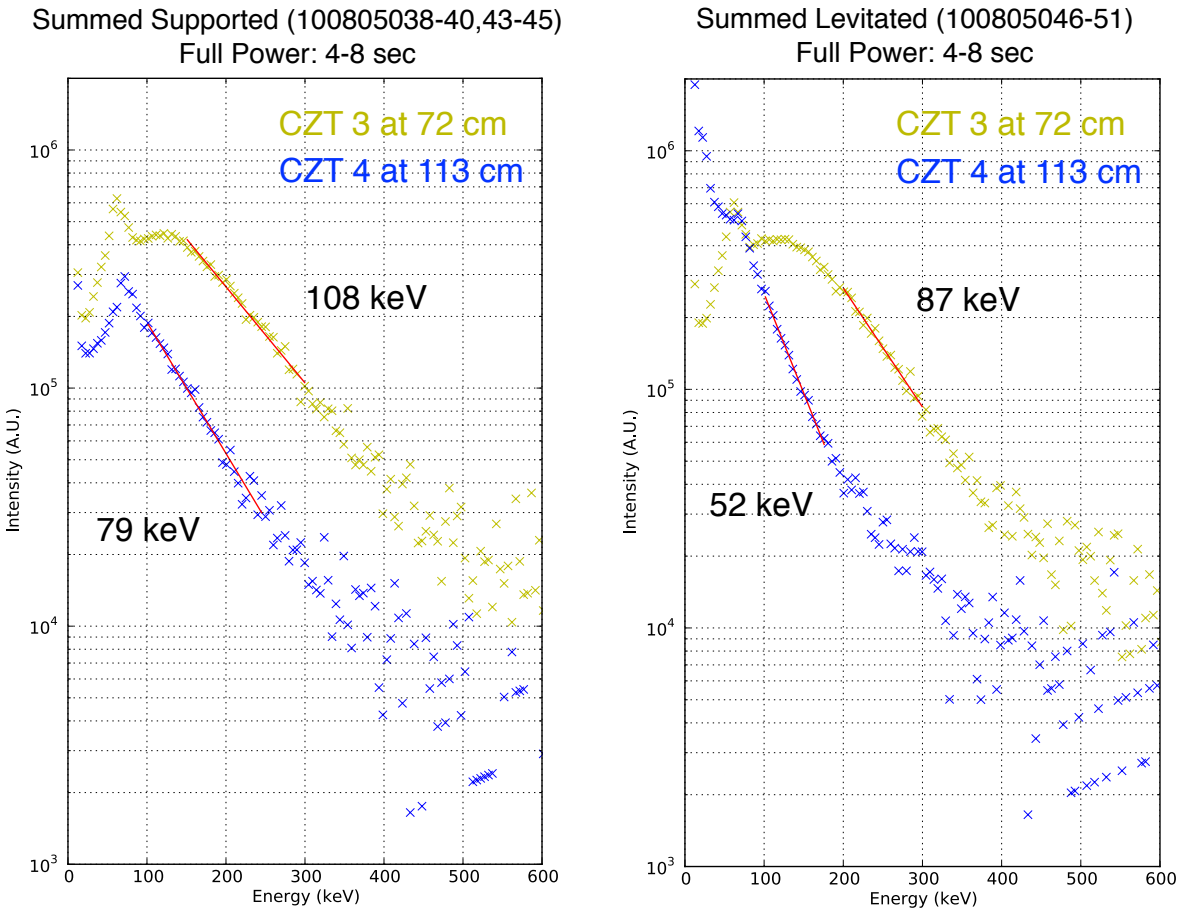

Figure 6.2: Summed spectra from CZT detectors with tangency radii 72 cm (CZT 3) and 113 cm (CZT 4). Spectra are corrected for the transmission efficiency and sensitivity of the CZT detectors. (a) supported shots, (b) levitated shots.

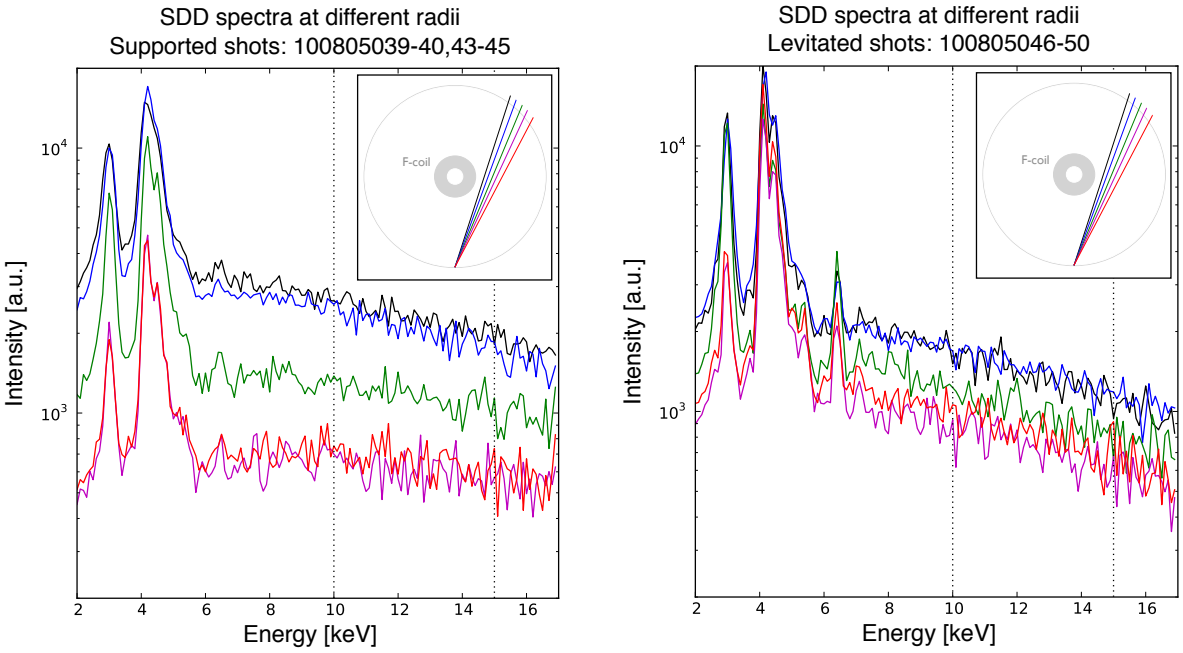

(a) (b)

Figure 6.3: Spectra from SDD detector with tangency radii 77 cm, 83 cm, 93 cm, 105 cm, and 116 cm (the detector's view angle was changed between shots). Signals are integrated during the stable, full power period from 4 to 8 seconds. (a) supported shots (100805038-40,43-45), (b) levitated shots (100805046-50).

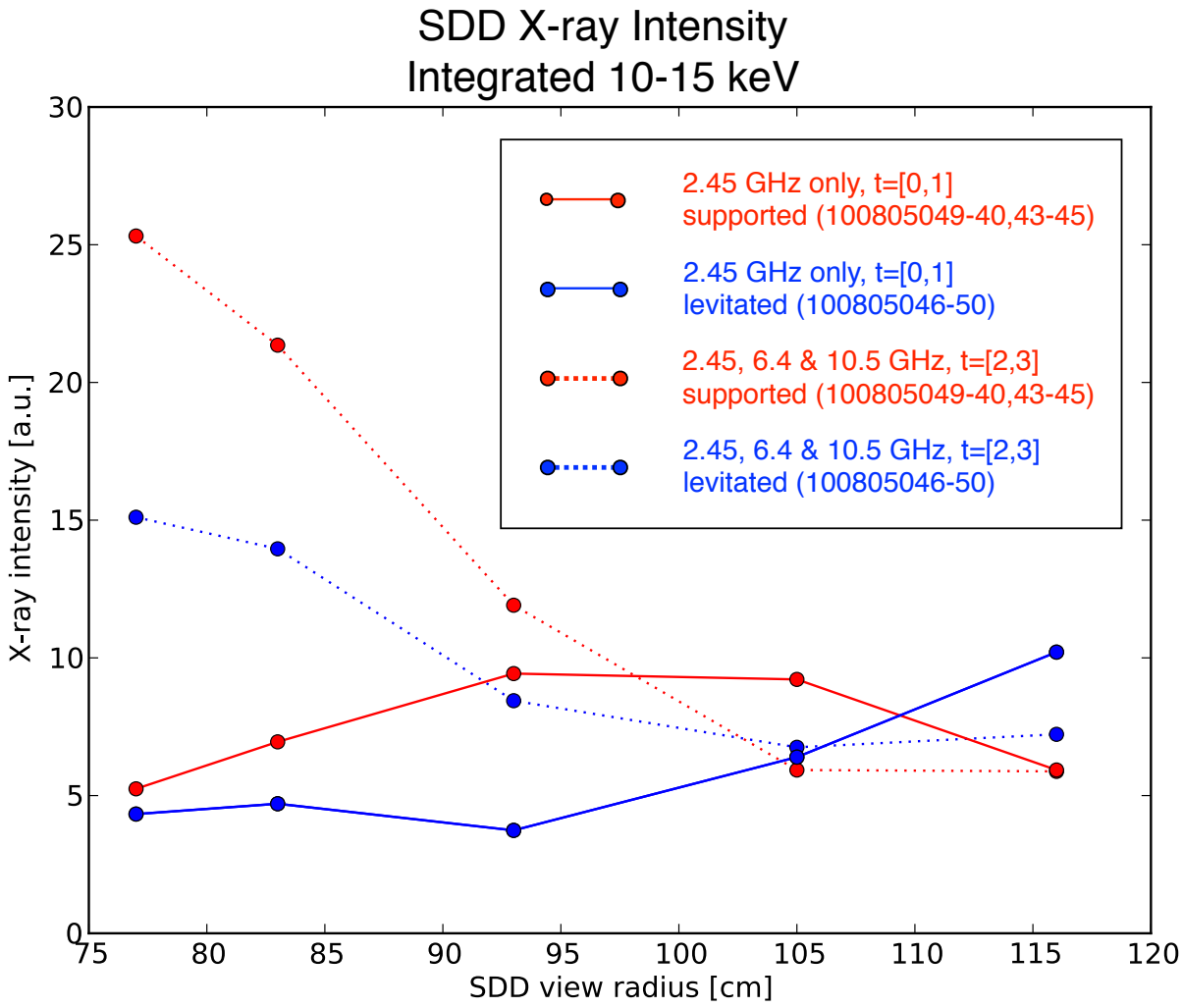

Figure 6.4: Continuum X-ray intensity measured by the SDD as a function of radius in supported and levitated operation. Intensity values at each radial point are calculated by integrating the X-ray spectrum between 10 and 15 keV (the region marked by the vertical dotted lines in figs. 6.3(a) and 6.3(b))

6.4 Spectra for higher density plasmas

Fewer X-rays are observed during plasmas created with only the 28 GHz heating source. Additionally, a fewer number of X-rays are observed during high density, helium plasmas. Figure 6.6 shows the decreased X-ray flux observed with a plasma generated with only the 28 GHz ECRH source (10 kW) compared to a plasma created with both the 28 GHz ECRH source (5 kW) and the 10.5 GHz ECRH source (5 kW). Figure 6.5 shows the decreased X-ray flux observed for a helium plasma compared to deuterium plasmas.

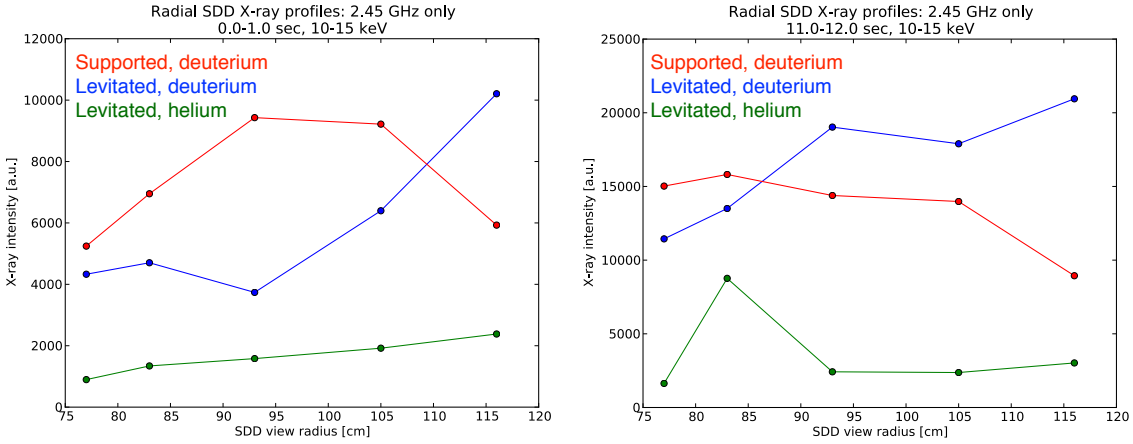

Figure 6.5: Few X-rays are observed during helium plasmas indicating that there are few hot electrons. Radial intensity profiles are constructed by integrating a section of the continuum spectrum for shots with different radial views (see fig. 6.4).

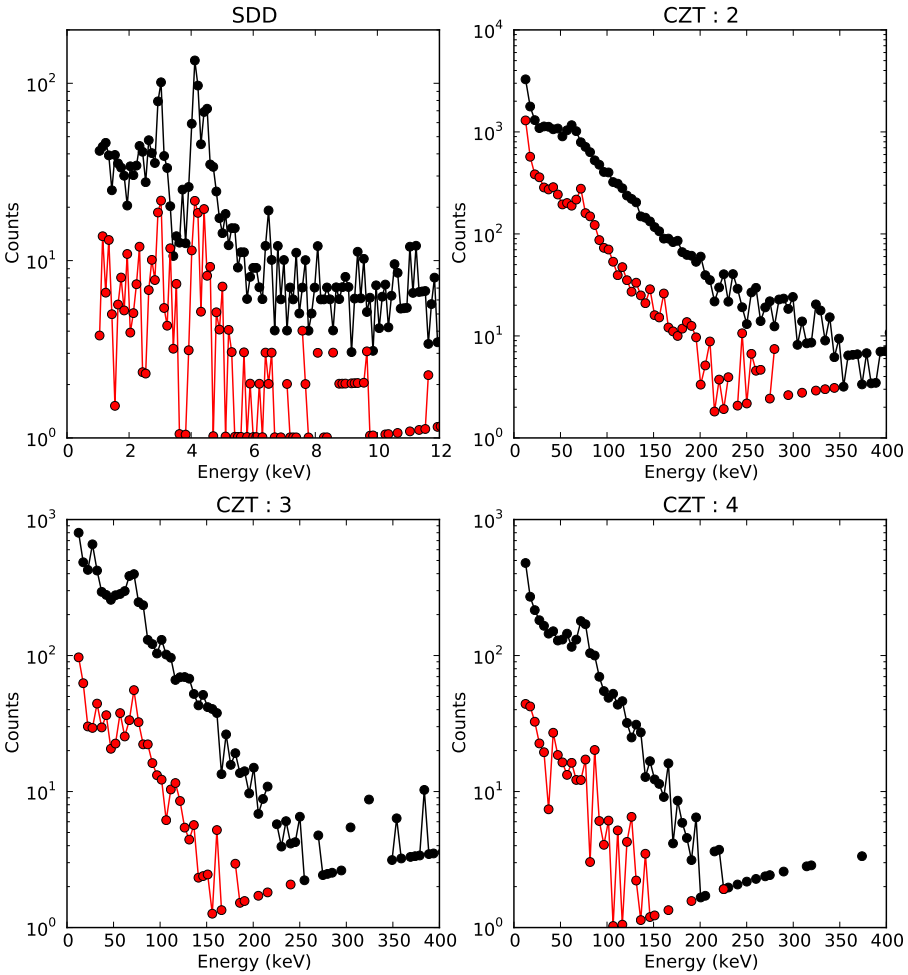

Figure 6.6: During the 28 GHz ECRH source only shot there is a significantly reduced amount of X-ray emission compared with other sources indicating fewer hot electrons; however, there is still some X-ray emission indicating some hot electrons. The panels show the X-ray spectra for the SDD and CZT detectors. The red traces are for a 28 GHz ECRH source only (10 kW) shot (100804018) and the black traces are for a shot (100804017) with both the 28 GHz ECRH source (5 kW) and the 10.5 GHz ECRH source (5 kW).

6.5 Estimation of the hot electron fraction

An estimate of the hot electron fraction (the ratio of the hot electron density over the total electron density) can be made using the pressure profiles calculated from the magnetic

reconstructions and the pseudo-temperature calculated for the hot electron population from the X-ray spectra. Comparing supported (100805045) and levitated (100805046) shots with multiple ECRH sources (see table 5.2) it is found that levitation decreases the hot electron fraction. This is believed to be due to both an increase in the thermal electron density (because levitation removes losses to supports) and a decrease of the hot electron number (because the greater density causes more scattering, which reduces the energetic population). For the supported shot, the hot electron energy is approximated as 100 keV. The maximum hot electron density is calculated by dividing the peak pressure by the hot electron energy. The interferometer measures the total electron density, which for supported operation is quite flat. The hot electron fraction is $\sim$ 35% for supported operation. For levitated operation, the partition of the plasma pressure between the hot electrons and a cooler, thermal population is not known so the extreme case is evaluated where all the pressure is in the hot electrons. Again the hot electron energy is taken to be 100 keV and the peak of the total electron density is obtained by inverting the interferometer measurements. The maximum hot electron fraction during levitated operation is $\sim$ 3%. However, magnetic measurements indicate that as much as half of the plasma pressure is in the thermal plasma [26]. Furthermore, the X-ray intensity (from energetic electrons) is lower during levitated operation (see fig. 6.4) although the plasma energy is greater (see table 5.2). Thus, the hot electron fraction during levitated operation is less than 3 %.

6.6 Soft X-ray conclusions

The X-rays detected by the Silicon Drift Detector and the CZT detectors are from a hot electron population and indicate that the hot electron population can be described by a

log-linear energy distribution in the range 50-100 keV. Because the X-rays come from a hot electron population, the X-ray signal provides a good indicator as to whether a plasma shot has relatively many or few hot electrons.

Measurements of the X-ray intensity for different radial sight lines show that the hot electron population is much more centrally peaked during supported operation than it is during levitated operation.

Combining information from the magnetic reconstruction of the pressure profile, interferometry, and the X-ray spectroscopic measurement of the hot electron energy shows that the fraction of hot electrons can reach 35% of the total electron density during supported operation. The hot electron fraction during levitated operation is at least an order of magnitude smaller (i.e., $< 3\%$) than the fraction during supported operation.

Chapter 7

Analysis and interpretation

This chapter collects and interprets the observations described in the preceding two chapters. The magnetic reconstructions presented in Chapter 5 provide a measurement of the total pressure profile. The total pressure may include contributions from multiple populations. A simple model that is used here is that the total pressure is a combination of the pressure from a small, hot electron population and a larger, thermal electron population. As discussed in Chapter 2, the hot electron population is subject to different stability criteria than the thermal electron population. Provided that there is a sufficient density of cooler plasma present, the hot population can be stable with a pressure gradient that is steeper than the maximum pressure gradient for stability to the MHD interchange mode, $\delta(pV^{\gamma}) \geq 0$. The internally heated thermal electron population is predicted to relax to a profile that is marginally stable to MHD interchange. As such, plasmas with fewer hot electrons are of particular interest because in those plasmas the pressure measured by the magnetics is composed primarily of pressure contained in a thermal population. The X-ray measurements presented in Chapter 6 were found to come from the hot electrons and thus provide a

qualitative measure of the relative size of the hot electron population for a particular plasma. In this chapter, an analysis of a variety of plasma shots is presented to better understand the steepness of the thermal plasma pressure.

7.1 Turbulent diffusion

As discussed in section 2.2.5, random fluctuations of the azimuthal electric field cause the plasma to take random $\mathbf{E} \times \mathbf{B}$ steps in the radial direction, and the diffusion coefficient of this process is $D_{\psi\psi} = R^2 \langle E_\phi^2 \rangle \tau_{cor}$ where R is the radial cylindrical coordinate, $\langle E_\phi^2 \rangle$ is the mean-square of the azimuthal electric field fluctuations, and τ_{cor} is the correlation time of the fluctuations [9].

For μ and J (the 1^{st} and 2^{nd} adiabatic invariants) and for $D_{\psi\psi}$ independent of μ, J, and ψ (the 3^{rd} adiabatic invariant), the time evolution of the density and pressure profiles (due to this turbulent process) are given by the turbulent diffusion equations:

$$\frac{d}{dt}(nV) = \frac{\partial}{\partial\psi}\left[D_{\psi\psi}\frac{\partial}{\partial\psi}(nV)\right] + \langle S \rangle \tag{7.1}$$

$$\frac{d}{dt}(pV^\gamma) = \frac{\partial}{\partial\psi}\left[D_{\psi\psi}\frac{\partial}{\partial\psi}(pV^\gamma)\right] + \langle H \rangle \tag{7.2}$$

where n is the plasma density, p is the plasma pressure, V is the differential flux-tube volume, γ is the ratio of specific heats, $D_{\psi\psi}$ is the turbulent diffusion coefficent, and $\langle S \rangle$ and $\langle H \rangle$ are flux-tube averaged source/sink terms.

The invariant density and pressure profiles are steady state solutions to the turbulent diffusion equations for a specific set of sources, sinks, and boundary conditions. In the ideal model of LDX, turbulent diffusion is driven in the region outside the pressure peak (in the

region of unfavorable magnetic curvature) by internal ECR heating. Inside the pressure peak (in the region of favorable magnetic curvature) transport may be slower. Thus, invariant profiles are only expected to form in the region between the pressure peak and the plasma separatrix. From eqs. (7.1) and (7.2) it can be seen that the invariant profiles make several assumptions: (1) there are no sources or sinks, (2) the diffusion coefficient is a constant, and (3) suitable boundary conditions are used (e.g., $(nV)_A = (nV)_B$). Baker, et al. [79] derive eqs. (7.1) and (7.2) for a more general form of the diffusion coefficient (which is expected in a tokamak).

Observations of invariant density profiles with the interferometer [23] suggest that the latter two assumptions are probably true for many levitated plasmas on LDX. However, it is likely that the ECR heating deposits energy throughout the plasma volume in a complex manner such that $\langle H \rangle \neq 0$. Additionally, charge exchange losses may provide further sink terms to eq. (7.2).

7.2 Levitated versus supported operation

During supported operation all the plasma pressure is contained in the mirror trapped hot electron population because thermal (more collisional) plasma is more rapidly lost along the magnetic field lines to the mechanical supports. Magnetic reconstructions confirm this picture by showing the pressure profile to be extremely peaked (see fig. 5.5). X-ray measurements indicate the presence of an electron population that can be described by a log-linear energy distribution in the range 50-100 keV. When the dipole is magnetically levitated the X-ray spectra remain similar to the spectra observed in supported operation indicating that the X-ray source is still a hot electron population. However, magnetic reconstructions of the

plasma pressure during levitation with multiple ECRH sources show that the total pressure profile is much broader than it is during supported operation (see figs. 5.2 and 5.3). This indicates that a portion of the total plasma pressure represents a thermal population.

To evaluate whether the reconstructed total pressure profile is MHD stable the entropy density factor, $p(\psi)V(\psi)^{\gamma}$, is plotted as a function of radius (see fig. 7.1). If the entropy density factor increases with radius the pressure profile is MHD stable. If the entropy density factor decreases with radius the pressure profile is steeper than the MHD limit. Because the plasma is observed to be in a stable steady-state, a pressure profile that exceeds the MHD limit indicates a portion of the pressure is in a gyrokinetically stabilized hot electron population.

The blue trace in fig. 7.1 shows that for $\gamma = 5/3$ the reconstructed pressure profile describes a profile with a constant entropy density factor outside the pressure peak. This pressure profile is near the marginal stability point to the MHD interchange mode. This profile is consistent with a turbulent adiabatic mixing of flux-tubes driven by an internal heating source. In contrast, the red trace in fig. 7.1 shows that in supported operation the pressure profile is much steeper than the MHD limit. This indicates that during supported operation a majority of the plasma pressure is contained in a hot electron population. Stability of the plasma to the hot electron interchange mode (HEI) is determined by the hot electron density profile (see eq. (2.18)). An estimate of the hot electron density profile can be made by combining X-ray measurements of the hot electron energy distribution with the supported pressure profile. The supported pressure profile is qualitatively consistent with HEI stability, which is consistent with other diagnostic observations on LDX.

Figures 7.2(a) and 7.2(b) compare the density and temperature profiles during supported and levitated operation. The density profiles are deduced from the interferometer measure-

ments. The inner most view of the interferometer has a tangency radius of 77 cm so no information about the density profile inside 77 cm is known. The density profile during supported operation is relatively flat. During levitation the density profile is centrally peaked though it is less peaked than an invariant density profile. The temperature profile is obtained by dividing the pressure profile deduced from the magnetics by the density profile. Thus, it is an average or effective temperature profile. In supported operation the temperature is highly peaked with peak electron energies of about 40 keV (this is consistent with X-ray measurements of the hot electron population). During levitation the temperature profile is much broader and the peak electron energy is much lower (about 4 keV). This indicates that there is a portion of the plasma pressure in a hot or warm electron population, but the broadening of the profile shows that there is also a portion of the plasma pressure in a thermal population.

Magnetic reconstructions of the pressure profile with only the 2.45 GHz ECRH source indicate that the pressure profile in supported and levitated operation is similarly steep ($g \sim 3.5$, this steepness parameter corresponds to a pressure profile steeper than the MHD limit). In supported operation the pressure peak is near the 2.45 GHz mid-plane heating resonance at 82 cm, but during levitation the pressure peak moves out in radius to 95-100 cm (see figs. 5.8(a) and 5.8(b)). A possible reason for the pressure peak moving out is that the increased density is shielding the fundamental 2.45 GHz resonance (located at 82 cm). If the density is too high electromagnetic waves will reflect off the plasma rather than propagate through it. The density at which waves will no longer propagate in a plasma is called the cutoff density and for 2.45 GHz waves the cutoff density is 7.4×10^{10} cm^{-3}. An inversion of the 4 chord interferometer measurements indicates that the plasma density inside of 90 cm is greater than 10^{11} cm^{-3}. Therefore, with the fundamental resonance cutoff

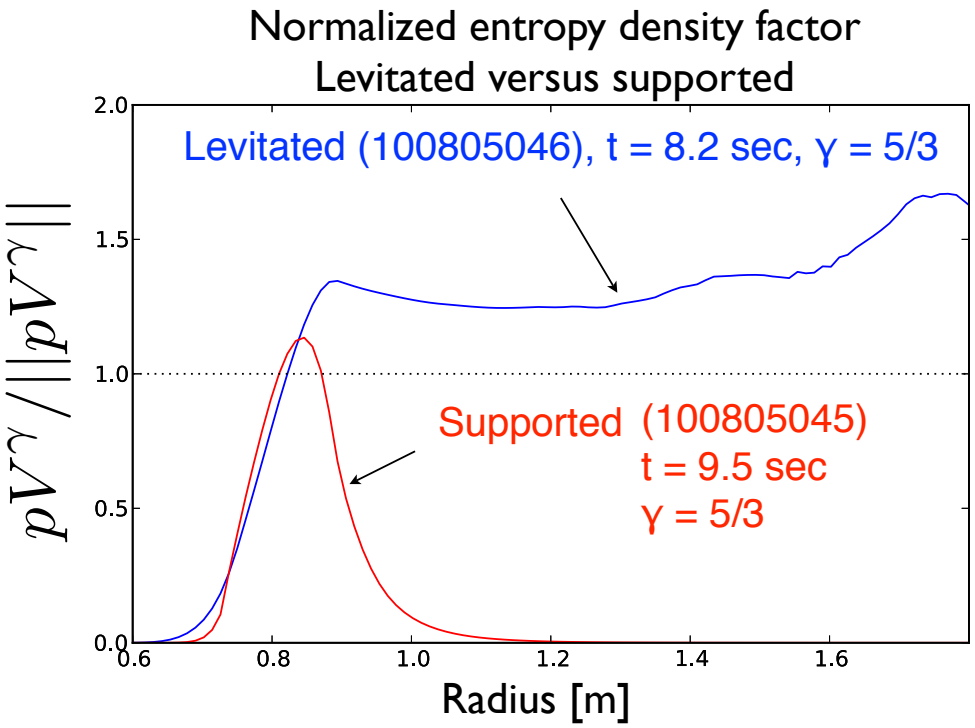

Figure 7.1: For levitated shot 100805046 with multiple ECRH sources on the entropy density factor is constant with radius outside the pressure peak (at radius 81 cm). This is consistent with a pressure profile that is marginally stable to the MHD interchange mode. For supported shot 100805045 with multiple ECRH sources on the entropy density factor decreases with radius outside of the pressure peak (at radius 80 cm) indicating a pressure profile that is steeper than the MHD limit.

more heating may be occurring at the mid-plane 1^{st} harmonic of the 2.45 GHz heating source (see fig. 3.2) at about 1 m or at the upper hybrid resonance.

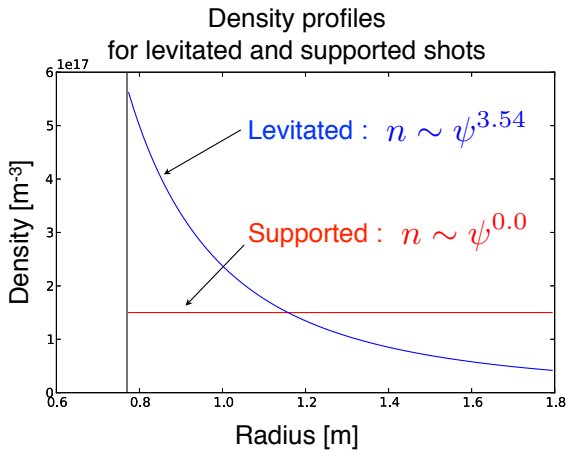

(a)

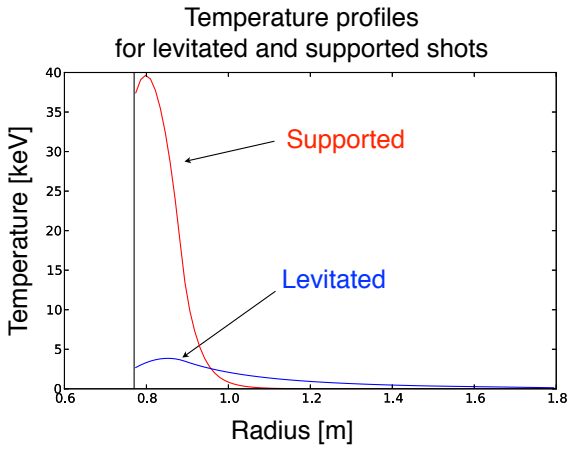

(b)

Figure 7.2: Density and temperature profiles for a levitated (100805046) and a supported (100805045) shot. (a) Reconstructed density profile from the interferometer measurements. (b) Temperature profile deduced from the magnetically reconstructed pressure profile and the density profile.

7.3 Levitated, high density plasmas

The comparison of levitated and supported plasmas shows that during levitation a portion of the plasma pressure is contained in a thermal population but a portion is also contained in a mirror trapped hot population. For the shots analyzed in this section it is generally found

that higher density shots correlate with fewer X-rays and broader pressure profiles. This is interpreted to mean that higher density plasmas are more thermal with a smaller fraction of the plasma pressure contained in a gyrokinetically stabilized hot electron population. To compare high and low density plasmas the 28 GHz ECRH source is used. The 28 GHz heating source is unique from the other power sources on LDX in that it creates density (similar to other ECRH sources) but little diamagnetic flux (compared to other ECRH sources). This is likely because its lowest mid-plane resonances are at its $3rd$ and $4th$ harmonics and very little power should be deposited at these high harmonic resonances.

7.3.1 10.5 GHz ECRH source with and without the 28 GHz ECRH source

The 10.5 GHz heating source has a higher cutoff density than the 2.45 GHz heating source so in most plasma shots the primary mid-plane resonance is not shielded during levitation and the pressure peak remains near the resonance. The effect of the 28 GHz heating source, which increases the plasma density, but not beyond the 10.5 GHz cutoff density, is to broaden the pressure profile. Figures 5.10(a) and 5.10(b) show the pressure profile is broader with the 28 GHz ECRH source on than it is with the 28 GHz ECRH source off. Figure 7.3 shows the normalized entropy density factor as a function of radius at a time with both the 10.5 GHz heating source and the 28 GHz heating source, and at a time with just the 10.5 GHz heating source. In both cases the entropy density factor decreases with radius indicating that the profile is steeper than the limit set by stability to the MHD interchange mode; however, with the 28 GHz heating source on the profile is broader. Figures 7.4(a) and 7.4(b) show the density and temperature profiles for both cases. With the 28 GHz heating source on the density is higher and density profile is broader, and the temperature

is lower and temperature profile is broader.

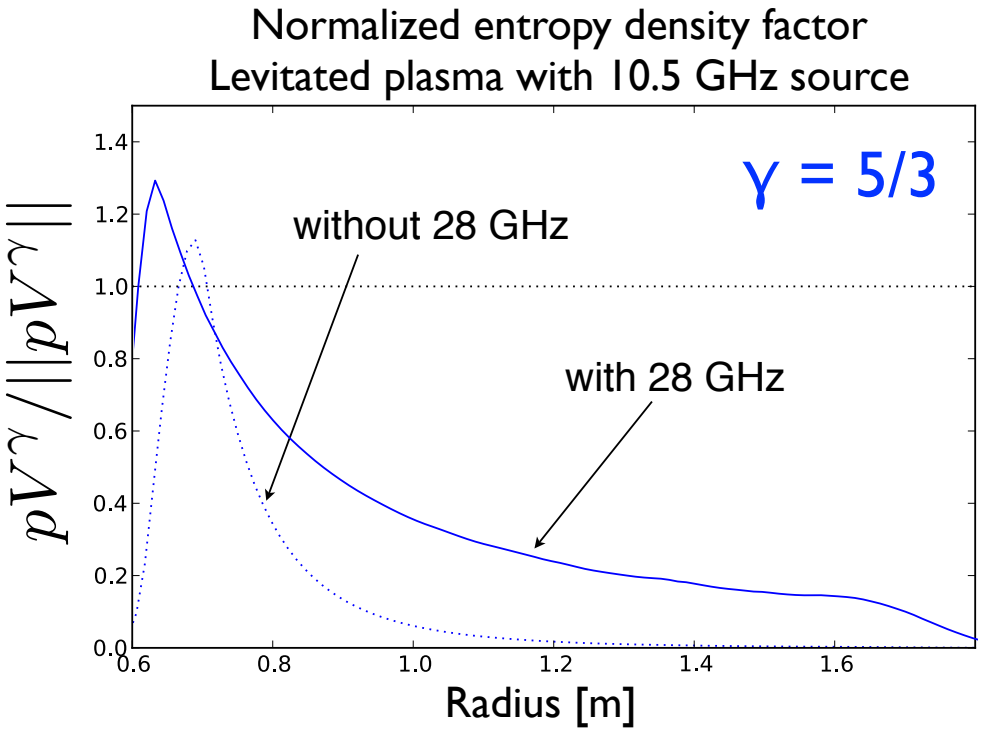

Figure 7.3: For levitated shot 100804017 with just the 10.5 GHz ECRH source on the entropy density factor decreases with radius indicating a pressure profile that is steeper than the MHD limit. On the same shot during a time with additional heating from the 28 GHz ECRH source the entropy density factor decreases less rapidly with radius but still indicates a pressure profile that is steeper than the MHD limit.

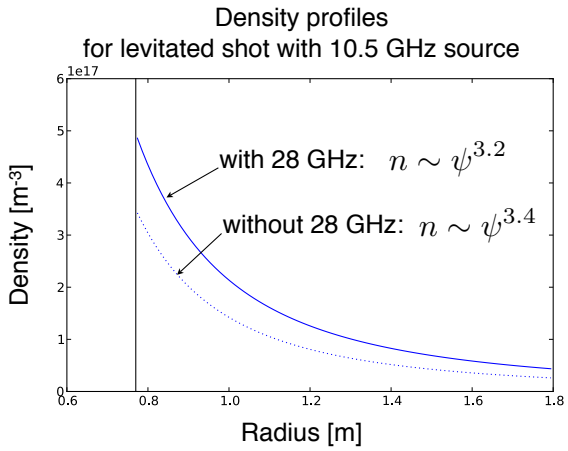

(a)

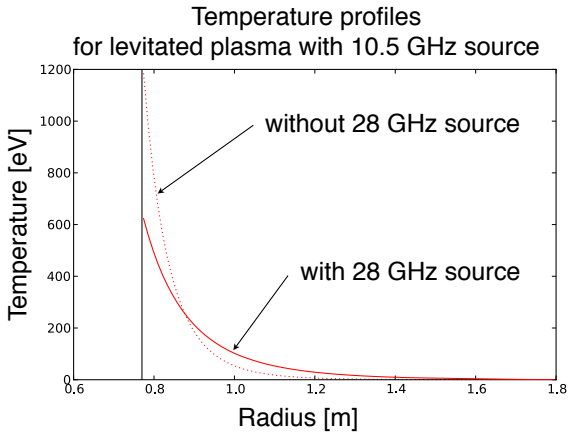

(b)

Figure 7.4: Density and temperature profiles for a levitated plasma with the 10.5 GHz source. (a) Reconstructed density profiles from the interferometer measurements. (b) Temperature profiles deduced from the magnetically reconstructed pressure profile and the density profile.

7.3.2 Full ECRH power, 28 GHz ECRH source shutoff

Shot 100805028 offers a particularly clear view of the effect of 28 GHz heating source on the pressure profile. On this shot the 28 GHz heating source was abruptly turned off at 8 seconds (normally the 28 GHz heating source is slowly ramped up and down over several

seconds). Interferometer measurements show an immediate decrease in density when the 28 GHz heating source is shutoff while the magnetics show a slower evolution of the pressure profile. Figure 5.14 shows that after the shutoff the pressure profile is steeper than before the shutoff when the density was higher. Figures 5.15(a) and 5.15(b) show a series of magnetic reconstructions performed at times around the shutoff. After the shutoff the pressure profile smoothly transitions from a broad profile ($g \sim 1.55$) to a steeper profile ($g > 2$). Figure 7.5 shows the normalized entropy density factor before and after the shutoff of the 28 GHz heating source. With the 28 GHz heating source on (t = 7 seconds) the entropy density factor increases with radius indicating that the pressure profile is less steep than the limit set by stability to the MHD interchange mode. After the shutoff of the 28 GHz heating source (t = 9 seconds) the entropy density decreases with radius indicating that the pressure profile is steeper than the MHD limit. This suggests that at the time without the 28 GHz heating source a larger portion of the plasma pressure is stored in a hot electron population. The presence of this population after the shutoff is shown by the increase in hot electron interchanges (HEIs) that reveal themselves as abrupt changes in the magnetic signals coupled with bursts of X-rays. Figures 7.6(a) and 7.6(b) show the density and temperature profiles. With the 28 GHz heating source on the density is higher and the temperature is lower.

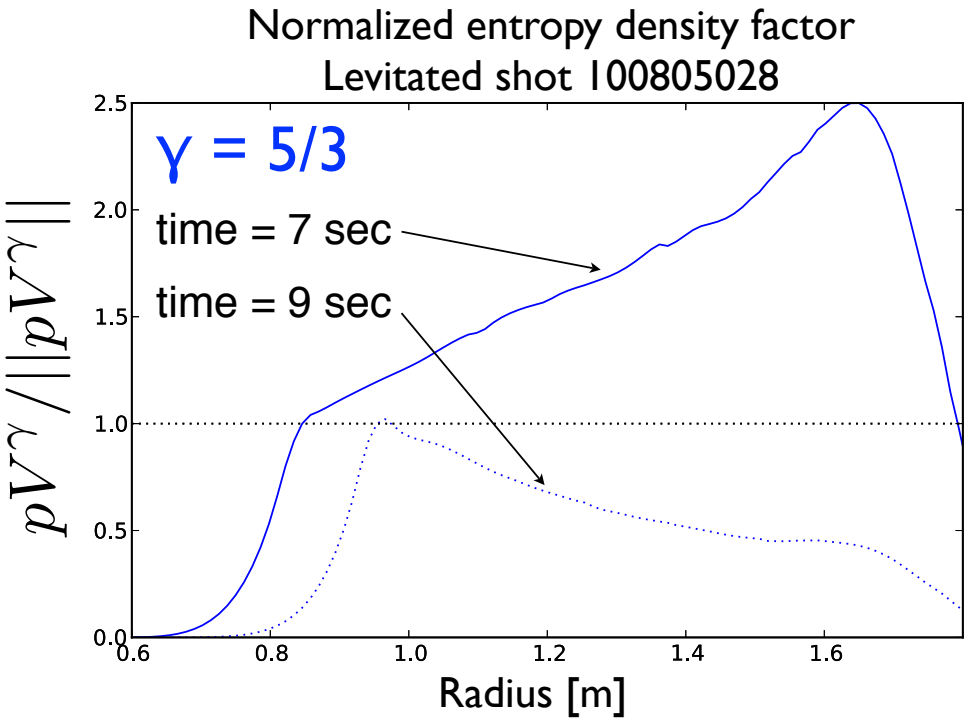

Figure 7.5: For levitated shot 100805028 with the 28 GHz source (and all other sources at time = 7 seconds) the entropy density factor increases with radius indicating a pressure profile that is stable to the MHD interchange mode. At time = 9 seconds the 28 GHz source is off (all other sources are still on) and the entropy density factor decreases with radius indicating a pressure profile that is steeper than the MHD limit.

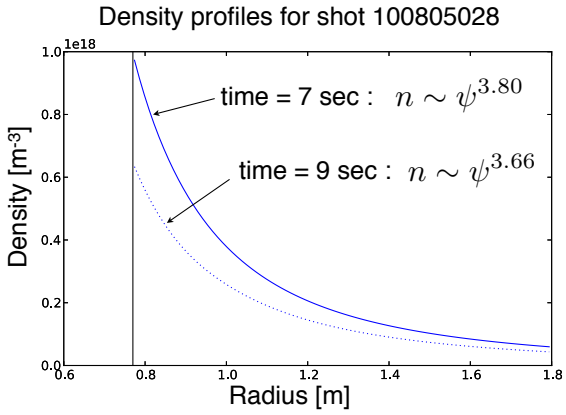

(a)

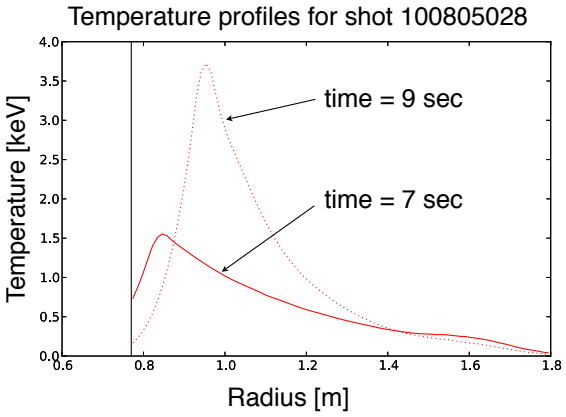

(b)

Figure 7.6: Density and temperature profiles for shot 100805028 with (time = 7 sec) and without (time = 9 sec) the 28 GHz source. (a) Reconstructed density profile from the interferometer measurements. (b) Temperature profile deduced from the magnetically reconstructed pressure profile and the density profile.

7.3.3 Helium plasma

Helium plasmas on LDX are typically denser (by about a factor of 2) than deuterium plasmas. The peak density is often well over $10^{18}\ m^{-3}$ which is sufficient to reduce transmission of interferometer microwave signal to receiver horn and distort the interferometer measurements. Also, there are typically many fewer measured X-rays with helium plasmas (see fig. 6.5) which indicates that there are fewer hot electrons.

Additionally, the time evolution of the diamagnetic current suggests that helium plasmas do not contain many hot electrons. During levitated plasmas the decay of the diamagnetic current after all the ECRH power is shut off, as measured by an outer magnetic flux loop, often shows two distinct decay times that have been attributed to the decay of the hot electron population (slow) and the decay of a warmer population (fast) [26]. During supported operation only the hot electron decay is observed. Figure 7.7 shows that for the helium plasma only the fast decay is observed. This suggests that the total plasma pressure consists primarily of a thermal population and there is little pressure in the hot electron population.

Magnetic reconstructions indicate that the total plasma pressure profile has a steepness parameter, g, of about 1.5. Figure 7.8 shows that the normalized entropy density factor increases with radius indicating that the steepness of the pressure profile is below the stability limit set by the MHD interchange mode. Figures 7.9(a) and 7.9(b) show the density and temperature profiles. The mild peaking of the density may indicate the presence of a weak particle pinch caused by relatively weak (entropy mode [18, 80]) turbulence but not an MHD driven turbulent pinch. This interpretation is consistent with the $p(\psi)V(\psi)^{\gamma}$ profile (see fig. 7.8).

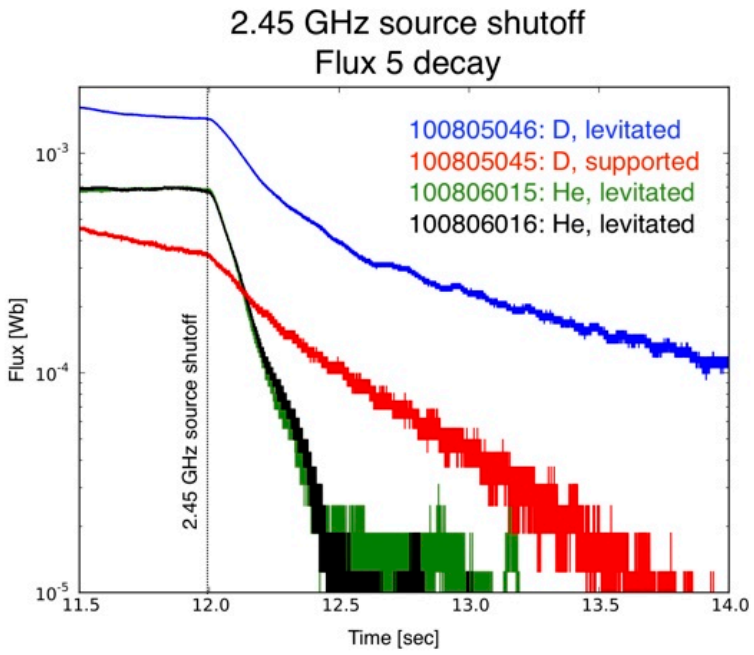

Figure 7.7: After the all power is shut off the decay of the diamagnetic current is observed by an outer flux loop. During supported operation a single decay time is observed and is attributed to the decay of the hot electron population. During levitated deuterium plasma two decay times are frequently observed [26] and are attributed to the decay of the hot electron population (slow) and a cooler, thermal population (fast). During levitated helium plasmas only the fast decay is observed suggesting most the pressure is in a cooler, thermal population and there is little pressure in the hot electrons.

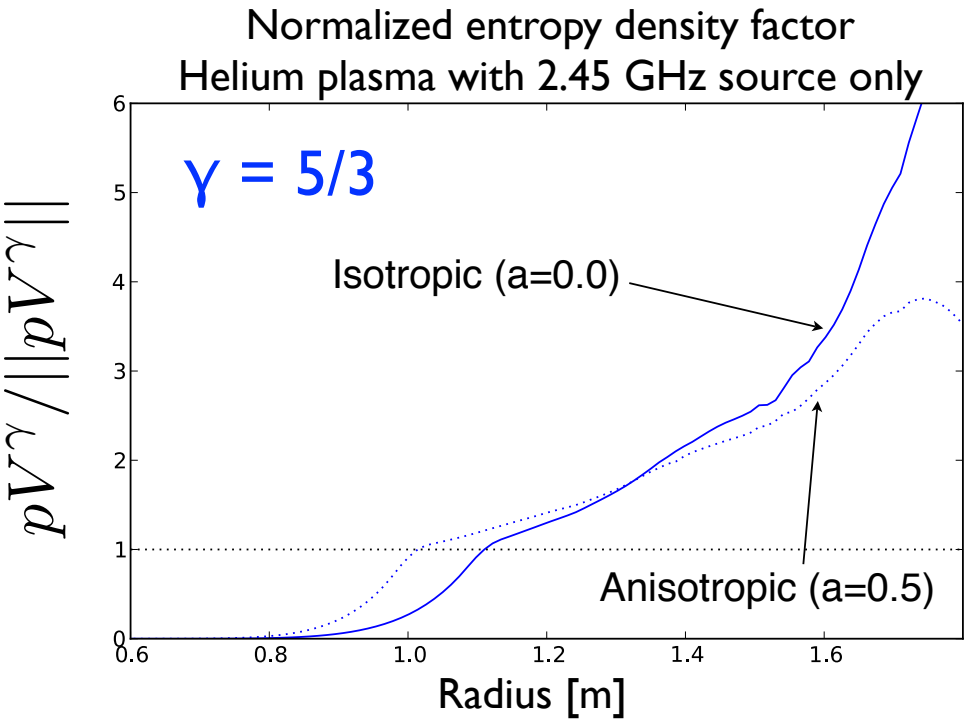

Figure 7.8: For helium shot 100806016 with just the 2.45 GHz ECRH source on the entropy density factor increases with radius for both an isotropic and isotropic pressure indicating a pressure profile that is MHD stable.

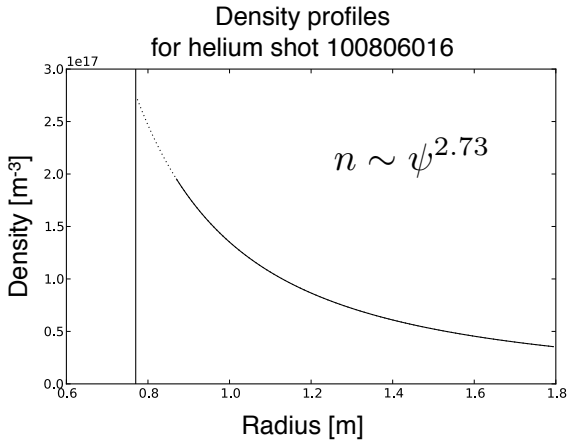

(a)

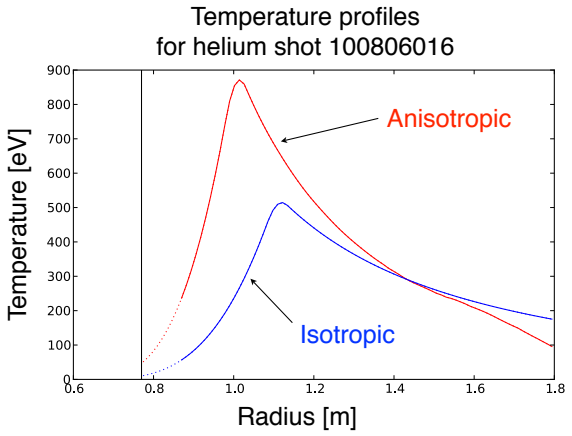

(b)

Figure 7.9: Density and temperature profiles for a helium plasma. (a) Reconstructed density profile from the interferometer measurements. Inside of 86 cm the density rolls over (has a lower value) so the density profile is fit to the outer interferometer chords. The dashed line indicates the projection of the fit inside of 86 cm. (b) Temperature profile deduced from the magnetically reconstructed pressure profile and the density profile.

7.3.4 28 GHz ECRH source only

The 28 GHz heating source tends to create plasma density without creating a large hot electron population (see fig. 6.6). As such, 28 GHz heating source only shots are the coolest plasmas created on LDX. These plasmas are likely to have the smallest hot electron pressure. Magnetic reconstructions (see figs. 5.20(a) and 5.20(b)) indicate that pressure profile for the 28 GHz heating source only plasma is broad ($g = 1.2 - 1.5$). Table 5.6 shows that the reconstructed pressure contains relatively less plasma energy ($10 - 15\ J$). Figure 7.10 shows that the normalized entropy density factor increases with radius indicating that the steepness of the pressure profile is below the stability limit set by the MHD interchange mode. Figures 7.11(a) and 7.11(b) show the density and temperature profiles. The reconstructed pressure profile is in reasonable agreement with measurements of the bulk temperature and density made with probes at the plasma edge (see figs. 7.12(a) and 7.12(b)). Similar to the helium plasma described in the previous section, the mild peaking of the density with an MHD stable $p(\psi)V(\psi)^{\gamma}$ profile may indicate the presence of a weak particle pinch caused by relatively weak (entropy mode [18, 80]) turbulence, but not an MHD driven turbulent pinch.

Edge probe analysis

Edge probe sweeps on plasmas heated with only the 28 GHz heating source are generally relatively easy to interpret (see figs. 7.12(a) and 7.12(b)). The temperature and density measured by the edge probe during the middle of the heating at about 8.5 seconds are $4.4\,eV$ and $3.1 \times 10^{16}\,m^{-3}$. The probe edge density measurement agrees with the edge density from the density profile reconstructed from the interferometer measurement to within a factor of 2 (see fig. 7.11(a)). The probe edge temperature measurement agrees with the edge

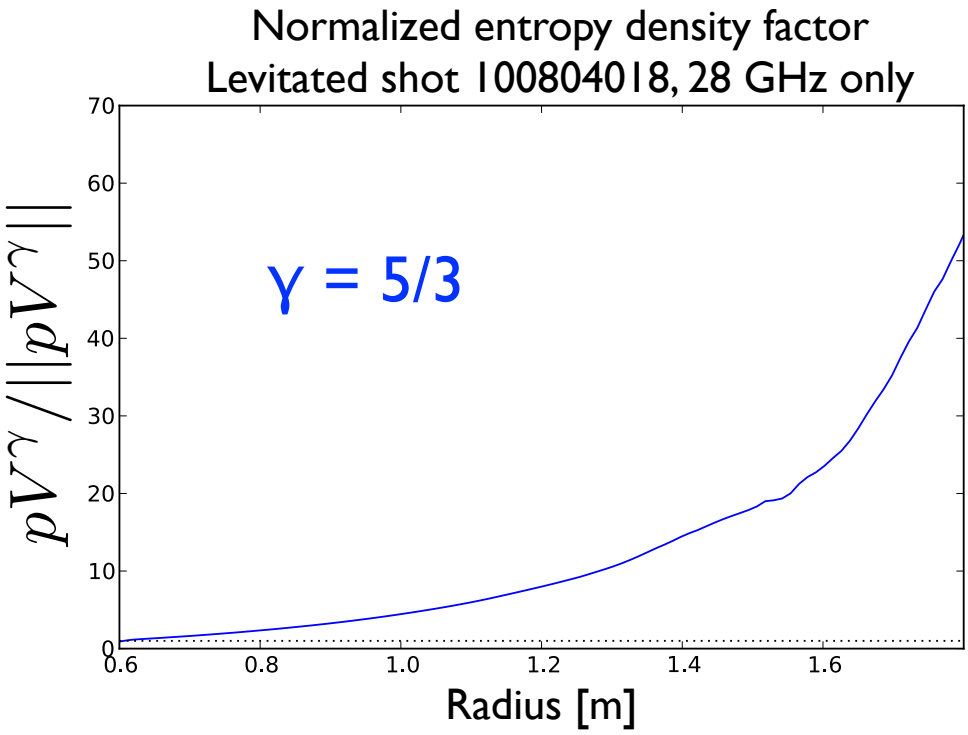

Figure 7.10: For levitated shot 100804018 with only the 28 GHz heating source the entropy density factor increases with radius indicating a pressure profile that is stable to the MHD interchange mode.

temperature from the temperature profile deduced from the magnetic reconstruction of the pressure and interferometer density profile to within a factor of 3 or 4 (see fig. 7.11(b)).

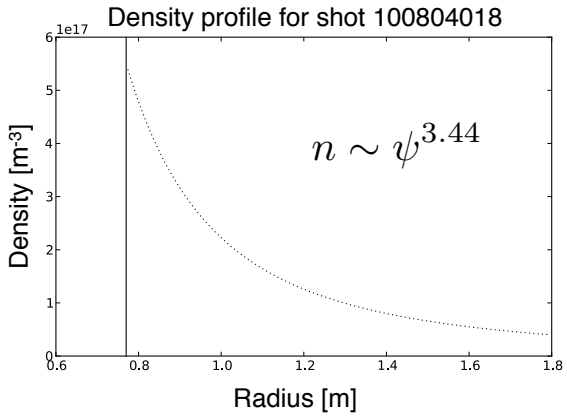

(a)

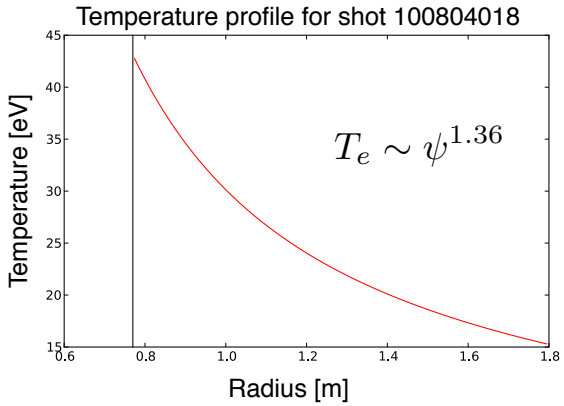

(b)

Figure 7.11: (a) Reconstructed density profile from the interferometer measurements. (b) Temperature profile deduced from the magnetically reconstructed pressure profile and the density profile.

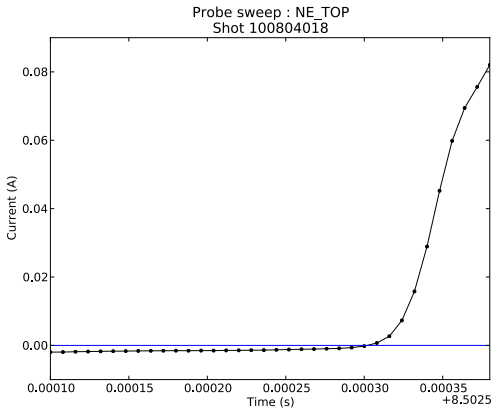

(a)

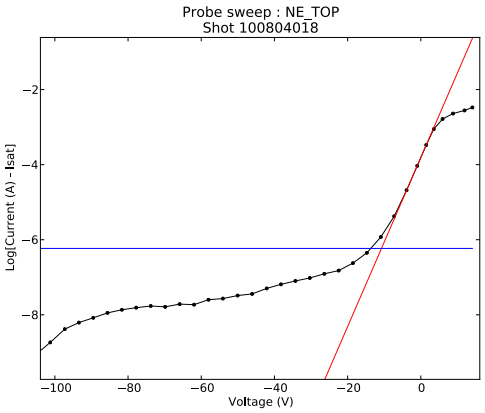

(b)

Figure 7.12: (a) Time trace of the swept NE_TOP probe. (b) I-V curve of the NE_TOP probe at about 8.5 sec. The temperature from the fit shown by the red line is $4.4\,eV$ and the density is $3.1 \times 10^{16}\,m^{-3}$.

Visible light

Figures 7.13(a) to 7.13(c) show that on shots with single frequency ECRH the visible light camera observes light around magnetic flux surfaces that contain the lowest harmonic, mid-plane resonance of the heating source. One interpretation of this is that because heating is most efficient at the mid-plane resonance the flux-surface containing this resonance becomes completely ionized (so the flux surface appears darker on the visible camera). The bright regions around the resonance surfaces are ionization edges. This suggests that with only the 28 GHz heating source some hot electrons may form at the 4th harmonic mid-plane resonance despite the lower efficiency of heating at that high harmonic.

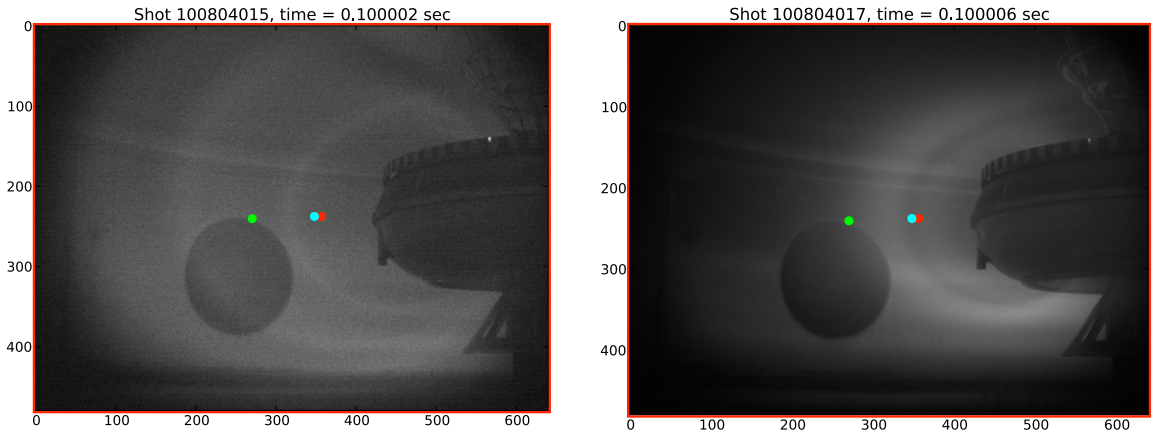

(a) (b)

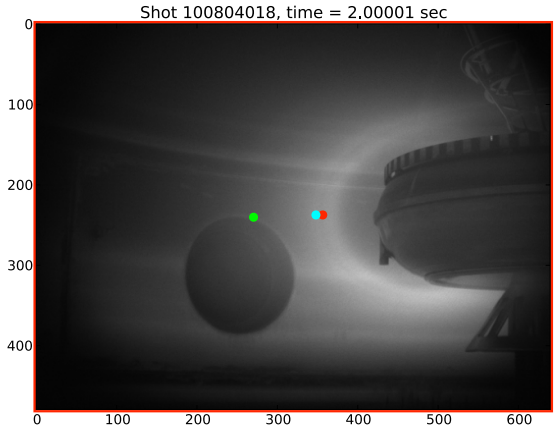

(c)

Figure 7.13: (a) 2.45 GHz only, (b) 10.5 GHz only, (c) 28 GHz only. The green, cyan, and red dots indicate the approximate locations of the 2.45 GHz fundamental resonance, the 10.5 GHz 1st harmonic resonance, and the 28 GHz 4th harmonic resonance, respectively. The color scale is adjusted to show the resonances and is not the same between the different heating cases.

Chapter 8

Conclusion

One of the research goals of LDX is to determine whether a laboratory plasma confined in the field of a levitated dipole magnet can adopt a specific type of centrally peaked pressure profile, called an invariant pressure profile, in which an exchange of plasma flux-tubes does not change the profile. Interest in the invariant pressure profile is twofold: (1) there is fundamental interest in a system that develops an averaged peaked profile, rather than a flat profile, when it undergoes a turbulent mixing process, and (2) the peaked profile is a requirement for a magnetic dipole confinement system, in which a hot, dense plasma is used for the production of fusion energy.

The work done in this thesis has shown that for microwave heated plasmas confined in the field of a dipole magnet the pressure profiles can be well described by centrally peaked pressure profiles. These dipole-confined plasmas can have peaked pressure profiles that are (i) steeper than, (ii) shallower than, or (iii) near the invariant profile dependent on plasma conditions. The variability is attributed to the presence of an energetic electron population created by ECRH and the complex heating profile of the ECRH.

In this work, magnetic and X-ray measurements have been used to (1) reconstruct the plasma pressure profile on the Levitated Dipole Experiment (LDX), (2) examine variations of the plasma pressure for different plasma conditions, and (3) analyze the plasma pressure gradient and its relation to both the invariant pressure profile and the MHD marginal stability point: $\delta(pV^{\gamma}) = 0$. In particular, the pressure profiles that corresponded to the configuration of a mechanically supported dipole and a magnetically levitated dipole were compared.

It was found that during supported operation the plasma pressure was highly peaked. X-ray measurements showed that high plasma pressures developed in supported shots due to the formation of a hot, mirror trapped electron population that was created by the electron cyclotron resonance heating. These hot electrons are known to be gyrokinetically stabilized by the background plasma and can adopt pressure profiles steeper than the MHD limit. X-ray measurements indicated that this hot electron population could be described by a log-linear energy distribution in the range 50-100 keV. Combining information from the magnetic reconstruction of the pressure profile, interferometer measurements of the electron density profile, and X-ray measurements of the hot electron energy distribution, the hot electron fraction at the pressure peak was estimated to be $\sim 35\%$ of the total electron population.

When the superconducting dipole magnet was magnetically levitated the plasma pressure profile was broader than it was during supported operation, and the pressure appeared to be contained in both a thermal population and an energetic electron population. X-ray spectra were similar during levitated and supported operation indicating that the X-ray source in both cases was a hot electron population. However, in levitated operation the hot electron fraction at the pressure peak was estimated to be less than $\sim 3\%$ of the total electron

population. Because the X-rays came from the hot electron population, the X-ray signal provided a good qualitative indicator as to whether a plasma shot had relatively many or few hot electrons. It was found that plasmas with fewer hot electrons (i.e., fewer X-rays) had broader pressure profiles.

To compare the magnetically reconstructed pressure profiles to the MHD stability limit the entropy density factor, $p(\psi)V(\psi)^{\gamma}$, was plotted as a function of radius. Dependent on shot conditions the pressure gradients of levitated plasmas were observed to be either MHD stable or unstable. Those profiles that exceeded the MHD limit were observed to have larger fractions of energetic electrons. When the dipole magnet was supported, high pressure plasmas always had profiles that exceeded the MHD interchange stability limit, and the high pressure in these plasmas appeared to arise entirely from a population of energetic trapped electrons.

8.1 Future work

The work done in this thesis suggests several future experiments that can be done on LDX. Experiments that can be done given the current funding constraints:

1. **Baffle the upper mirror plasma.** A mechanical baffle placed in the vacuum chamber between the F-coil and the L-coil would remove the upper mirror plasma discussed in section 4.6. Removal of this plasma would simplify and improve the magnetic reconstructions and potentially improve the levitation system. Additionally, this should reduce the microwave heating power deposited outside the dipole confinement region.

2. **Create high density plasmas to limit the hot electron population.** Observation of the thermal pressure profile is complicated by the presence of a gyrokinetically

stabilized hot electron population. Thus, plasmas with fewer hot electrons may provide better measurements of the thermal pressure profile, which is predicted to adopt the invariant pressure profile and be subject to the MHD stability limit. In this thesis it was observed that high density plasmas with few hot electrons were created when helium gas was used and/or when the only the 28 GHz heating source was used. Several potential experiments with the 28 GHz heating source include (1) levitated/supported comparison with a crowbarring (quick shut off) of the heating source, (2) turning on the 28 GHz heating source before other sources to create a background density that may suppress the growth of a hot electron population, and (3) use the 28 GHz heating source in conjunction with single other sources at variable power that can provide relatively localized internal mid-plane heating, particularly the 10.5 GHz heating source since it has a higher density cutoff.

3. **Dynamic limiter.** Install a dynamic limiter (or simply use the launcher) that allows a transition from levitated to supported operation during a shot. The rapid removal of the thermal plasma would allow its signature on the diagnostics to be deduced before the hot electron population has time to rebuild.

4. **Use Helmholtz coils to create smaller plasma volume.** A smaller plasma volume may make more efficient use of the 28 kW of microwave heating power currently available on LDX.

Experiments that are presently not financially feasible are listed below. However, scientific opportunities motivate these more costly experiments.

1. **Multi-point Thomson scattering.** Shining a laser through the plasma and observing the perpendicularly scattered light at multiple locations along the laser beam

would provide multiple local measurements of the electron density and temperature. This would decisively determine the thermal electron pressure and density profiles.

2. **Ion cyclotron resonance heating (ICRH).** A 1 MW VHF band transmitter is already on site. This has the potential to create a much denser and more thermal plasma without a hot electron population.

3. **More heating power.** LDX is currently power limited meaning that there is significant neutral penetration into the plasma. Greater heating power is expected to increase the plasma density (consistent with previous experimental observations) resulting in less neutral penetration into the plasma.

4. **Other non-ECRH heating sources.** Plasma injectors at the edge of LDX could create plasmas well suited for observing the pressure pinch. For an internally heated plasma (e.g., an ECRH plasma) the pressure profile relaxes from an overly peaked, unstable profile to a less peaked, stable profile. For a plasma created with plasma injectors the pressure source is on the outside so any peaking of the pressure profile requires an external drive such as RF or plasma pulsing; however, this also means that *any* peaking of the pressure profile would indicate a pressure pinch. The plasma injectors could be pulsed to simulate the solar wind impact on the magnetosphere.

5. **Pellet injection.** A lithium pellet injector originally built by Darren Garnier for work on Alcator C-mod still exists at the PSFC at MIT and is being considered for use on future LDX experiments. Pellet injection experiments will involve shooting a lithium pellet into the dipole confined plasma. It is expected that when the pellet reaches the locally trapped, hot electron population it will absorb nearly all the hot electron population's energy and will be rapidly ionized. This will create an unstable,

high-β flux-tube that will quickly expand outward.

Bibliography

[1] D.T. Garnier, A. Hansen, J. Kesner, M.E. Mauel, P.C. Michael, J.V. Minervini, A. Radovinsky, A. Zhukovsky, A. Boxer, J.L. Ellsworth, I. Karim, and E.E. Ortiz. Design and initial operation of the ldx facility. *Fusion Engineering and Design*, 81:2371–2380, 2006.

[2] D.T. Garnier, A. Hansen, M.E. Mauel, E. Ortiz, A.C. Boxer, J.L. Ellsworth, I. Karim, J. Kesner, S. Mahar, and A. Roach. Production and study of high-beta plasma confined by a superconducting dipole magnet. *Physics of Plasmas*, 13(056111), 2006.

[3] J. Kesner and M.E. Mauel. Plasma confinement in a levitated magnetic dipole. *Plasma Physics Reports*, 23(9):742–750, 1997.

[4] T. Gold. Motions in the magnetosphere of the earth. *Journal of Geophysical Research*, 64(9):1219–1224, September 1959.

[5] D.B. Melrose. Rotational effects on the distribution of thermal plasma in the magnetosphere of jupiter. *Planet. Space Sci.*, 15:381–93, 1967.

[6] A. Hasegawa. A dipole field fusion reactor. *Comments on Plasma Physics and Controlled Fusion*, 11(3):147–151, 1987.

[7] M.N. Rosenbluth and C.L. Longmire. Stability of plasmas confined by magnetic fields. *Annals of Physics*, 1:120–140, May 1957.

[8] C.-G. Fälthammar. Effects of time-dependent electric fields on geomagnetically trapped radiation. *Journal of Geophysical Research*, 70(11):2503–2516, June 1965.

[9] T.J. Birmingham. Convection electric fields and the diffusion of trapped magnetospheric radiation. *Journal of Geophysical Research, Space Physics*, 74(9):2169–2181, May 1969.

[10] A. Hasegawa, L. Chen, and M.E. Mauel. A D-^{3}He fusion reactor based on a dipole magnetic field. *Nuclear Fusion*, 30(11):2405–2413, 1990.

[11] J. Kesner, D.T. Garnier, A. Hansen, M.E. Mauel, and L. Bromberg. Helium catalysed D-D fusion in a levitated dipole. *Nuclear Fusion*, 44(1):193–203, 2004.

[12] M. Schulz and L.J. Lanzerotti. *Particle Diffusion in the Radiation Belts*, volume 7 of *Physics and chemistry in space*. Springer, New York, 1974.

[13] D.T. Garnier, J. Kesner, and M.E. Mauel. Magnetohydrodynamic stability in a levitated dipole. *Physics of Plasmas*, 6(9):3431–3434, September 1999.

[14] A. N. Simakov, P.J. Catto, N.S. Krasheninnikova, and J.J. Ramos. Ballooning stability of a point dipole equilibrium. *Physics of Plasmas*, 7:2526–2529, 2000.

[15] J. Kesner. Stability of electrostatic modes in a levitated dipole. *Physics of Plasmas*, 4(2):419–422, February 1997.

[16] J. Kesner. Stability of a plasma confined in a dipole field. *Physics of Plasmas*, 5(10):3675–3679, October 1998.

[17] J. Kesner. Interchange modes in a collisional plasma. *Physics of Plasmas*, 7(10):3837–3840, October 2000.

[18] J. Kesner and R.J. Hastie. Electrostatic drift modes in a closed field line configuration. *Physics of Plasmas*, 9(2):395–400, 2002.

[19] A. Kouznetsov, J. P. Freidberg, and J. Kesner. Quasilinear theory of interchange modes in a closed field line configuration. *Physics of Plasmas*, 14:102501, 2007.

[20] V.P. Pastukhov and N.V. Chudin. Self-consistent turbulent convection in a magnetized plasma. *JETP Letters*, 82(6):356–365, 2005.

[21] S. Kobayashi, B.N. Rogers, and W. Dorland. Particle pinch in gyrokinetic simulations of closed field-line systems. *Physical Review Letters*, 105:235004, 2010.

[22] A.C. Boxer, R. Bergmann, J.L. Ellsworth, D.T. Garnier, J. Kesner, M.E. Mauel, and P. Woskov. Turbulent inward pinch of plasma confined by a levitated dipole magnet. *Nature Physics*, 6:207–212, March 2010.

[23] Alexander C. Boxer. *Density profiles of plasmas confined by the field of a levitating, dipole magnet*. PhD thesis, MIT, 2008.

[24] J.L. Johnson, H.E. Dahed, J.M. Greene, R.C. Grimm, Y.Y. Hsieh, S.C. Jardin, J. Manickam, M. Okabayashi, R.G. Storer, A.M.M. Todd, D.E. Voss, and K.E. Weimer. Numerical determination of the axisymmetric toroidal magnetohydrodynamic equilibria. *Journal of Computational Physics*, 32:212–234, 1979.

[25] L.L. Lao, H. St. John, R.D. Stambaugh, A.G. Kellman, and W. Pfeiffer. Reconstruction of current profile parameters and plasma shapes in tokamaks. *Nuclear Fusion*, 25(11):1611–22, 1985.

[26] D.T. Garnier, A.C. Boxer, J.L. Ellsworth, J. Kesner, and M.E. Mauel. Confinement improvement with magnetic levitation of a superconducting dipole. *Nuclear Fusion*, 49(055023), 2009.

[27] E.I. Moses. Ignition and inertial confinement fusion at the National Ignition Facility. *Journal of Physics: Conference Series*, 244(012006), 2010.

[28] J.D. Lindl and et al. Progress towards ignition on the National Ignition Facility. *Nuclear Fusion*, 51(094024), 2011.

[29] Y. Shimomura, R. Aymar, V. Chuyanov, M. Huguet, and R. Parker. ITER overview. *Nuclear Fusion*, 39(9Y):1295–1308, 1999.

[30] N. Holtkamp. An overview of the ITER project. *Fusion Engineering and Design*, 82:427–434, 2007.

[31] R.J. Hawryluk and et al. Principal physics developments evaluated in the ITER design review. *Nuclear Fusion*, 49(065012), 2009.

[32] M.G. Kivelson and C.T. Russell, editors. *Introduction to Space Physics*. Cambridge University Press, 1995.

[33] B. Lehnert. Confinement of charged particles by a magnetic field. *Journal of Nuclear Energy, Part C*, 1(1):40–48, March 20 1959.

[34] B. Lehnert. Confinement of charged particles by a magnetic field. *Nature*, 181(4605):331–2, February 1 1958.

[35] B. Lehnert. On the possibilities of ring-current configurations as a fusion device. *Plasma Physics*, 10:281–289, 1968.

[36] J. Kesner and D.T. Garnier. Convective cell formation in a levitated dipole. *Physics of Plasmas*, 7:2733, 2000.

[37] W. M. Nevins. A review of confinement requirements for advanced fuels. *Journal of Fusion Energy*, 17(1):25–32, 1998.

[38] R.J. Goldston and P.H. Rutherford. *Introduction to Plasma Physics*. Taylor & Francis Group, New York, N.Y., U.S.A., 2000.

[39] L.D. Landau and E.M. Lifshitz. *Mechanics*, volume 1 of *Course in Theoretical Physics*, chapter VII. Butterworth-Heinemann, Oxford, U.K., third edition, 2007.

[40] T.G Northrop and E. Teller. Stability of the adiabatic motion of charged particles in the earth's field. *Physical Review*, 117(1):215–225, January 1960.

[41] A. Hasegawa. Motion of a charged particle and plasma equilibrium in a dipole magnetic field – Can a magnetic field trap a charged particle? Can a magnetic field having bad curvature trap a plasma stably? *Physica Scripta*, T116:72–74, 2005.

[42] H.P Warren, A. Bhattacharjee, and M.E. Mauel. On Arnol'd diffusion in a perturbed magnetic dipole field. *Geophysical Research Letters*, 19(9):941–944, 1992.

[43] I. Karim. *Equilibrium and Stablility Studies of Plasmas Confined in a Dipole Magnetic Field Using Magnetic Measurements*. PhD thesis, MIT, Department of Nuclear Engineering, 2007.

[44] I. Karim, M. E. Mauel, J. L. Ellsworth, A. C. Boxer, D. T. Garnier, A. K. Hansen, J. Kesner, and E. E. Ortiz. Equilibrium reconstruction of anisotropic pressure profile in the levitated dipole experiment. *Journal of Fusion Energy*, 26(1/2):99–102, 2007.

[45] N.A. Krall. Stabilization of hot electron plasma by a cold background. *Physics of Fluids*, 9:820, 1966.

[46] H.L. Berk. Stability of hot electron plasmas. *Physics of Fluids*, 19:1255–56, 1976.

[47] H. Sanuki and F.F. Chen. Physical mechanisms for hot-electron stabilization of low-frequency interchange modes. *Physics of Fluids*, 28(12):3567–71, 1985.

[48] M.E. Mauel. Laboratory observations of wave-induced radial transport within an "Artificial Radiation Belt". *J. Phys. IV France*, 7:307–318, 1997.

[49] B. Levitt, D. Maslovsky, and M.E. Mauel. Measurement of the global structure of interchange modes driven by energetic electrons trapped in a magnetic dipole. *Physics of Plasmas*, 9(6):2507–2517, 2002.

[50] E.E. Ortiz, A.C. Boxer, J.L. Ellsworth, D.T. Garnier, A. Hansen, I. Karim, J. Kesner, and M.E. Mauel. Effects of the hot electron interchange instability on plasma confined in a dipolar magnetic field. *Journal of Fusion Energy*, 26(1/2):139–144, 2007.

[51] E.E. Ortiz. *Observation of the Hot Electron Interchange Instability in a High Beta Dipolar Confined Plasma*. PhD thesis, Columbia University, 2007.

[52] Amptek, Inc. http://www.amptek.com, April 17, 2013.

[53] J.L. Ellsworth. X-ray diagnostics for the Levitated Dipole Experiment. Master's thesis, MIT, 2004.

[54] J.L. Ellsworth, J. Kesner, D.T. Garnier, A.K. Hansen, M.E. Mauel, and S. Zweben. X-ray measurements of the levitated dipole. In *Bulletin of the American Physical Society*, Denver, Colorado, 2005. 47th Annual Meeting of the APS Division of Plasma Physics.

[55] Inc. Amptek. *DP5 User Manual and Operating Instructions*. Amptek, Inc., 14 DeAngelo Dr., rev a1 edition, 2009.

[56] V.T. Jordanov, G.F. Knoll, A.C. Huber, and J.A. Pantazis. Digital techniques for real-time pulse shaping in radiation measurements. *Nuclear Instruments and Methods in Physics Research A*, 353:261–264, 1994.

[57] V.T. Jordanov and G.F. Knoll. Digital synthesis of pulse shapes in real time for high resolution radiation spectroscopy. *Nuclear Instruments and Methods in Physics Research A*, 345:337–345, 1994.

[58] C.E. McIlwain. Music and the magnetosphere. In C.S. Gllmor and J.R. Spreiter, editors, *Discovery of the Magnetosphere*, volume 7 of *History of Geophysics*, pages 137–139. American Geophysical Union, Washington, D.C., 1997.

[59] J.A. Van Allen. Energetic particles in the earth's external magnetic field. In C.S. Gllmor and J.R. Spreiter, editors, *Discovery of the Magnetosphere*, volume 7 of *History of Geophysics*, page 242. American Geophysical Union, Washington, D.C., 1997.

[60] E. Gamboa. Alcator C-Mod soft X-ray pulse height analysis system. Master's thesis, MIT, 2007.

[61] J. P. Freidberg. *Ideal Magnetohydrodynamics*. Plenum Press, New York, 1987.

[62] H. Saitoh, Z. Yoshida, J. Morikawa, Y. Yano, T. Mizushima, Y. Ogawa, M. Furukawa, Y. Kawai, K. Harima, Y. Kawazura, Y. Kaneko, K. Tadachi, S. Emoto, M. Kobayashi, T. Suguira, and G. Vogel. High-*Beta* plasma formation and observation of peaked density profile in RT-1. *Nuclear Fusion*, 51(063034), 2011.

[63] Z. Yoshida, H. Saitoh, Y. Yano, H. Mikami, W. Sakamoto, J. Morikawa, M. Furukawa, and S.M. Mahajan. Self-organized confinement by magnetic dipole: recent results from RT-1 and theoretical modeling. *Plasma Physics and Controlled Fusion*, 55(014018), 2013.

[64] S.P. Joy, M.G. Kivelson, R.J. Walker, K.K. Khurana, and C.T. Russell. Mirror mode structures in the Jovian magnetosheath. *Journal of Geophysical Research*, 111(A12212), 2006.

[65] D.P. Boyle, M.E. Mauel, D.T. Garnier, and J. Kesner. Eddy currents and magnetic reconstruction in LDX. In *Bulletin of the American Physical Society*, Atlanta, GA, 2009. 51st Annual Meeting of the APS Division of Plasma Physics.

[66] Jonathan E. Guyer, Daniel Wheeler, and James A. Warren. FiPy: Partial differential equations with Python. *Computing in Science and Engineering*, 11(3):6–15, 2009.

[67] FiPy. http://www.ctcms.nist.gov/fipy, September 10, 2012.

[68] E. Jones, T. Oliphant, P. Peterson, et al. SciPy: Open source scientific tools for Python. http://www.scipy.org, 2011–.

[69] J.D Hunter. Matplotlib: A 2d graphics environment. *Computing in Science & Engineering*, 9(3):90–95, 2007.

[70] M.E. Mauel. Dipole equilibrium with anisotropic pressure (revised). Technical report, Columbia University, 2005.

[71] A. N. Simakov, R.J. Hastie, and P.J. Catto. Anisotropic pressure stability of a plasma confined in a dipole magnetic field. *Physics of Plasmas*, 7(8):3309, 2000.

[72] J.W. Connor and R.J. Hastie. Effect of anisotropic pressure on the localized magnetohydrodynamic interchange modes in an axisymmetric torus. *Physics of Fluids*, 19:1727–32, 1976.

[73] S.I. Krasheninnikov and P.J. Catto. Effects of pressure anisotropy on plasma equilibrium in the magnetic field of a point dipole. *Physics of Plasmas*, 7:626–28, 2000.

[74] Jennifer L. Ellsworth. *Characterization of the low-frequency density fluctuations in dipole-confined laboratory plasmas*. PhD thesis, MIT, 2010.

[75] W.H. Press, B.P. Flannery, S.A. Teukolsky, and W.T. Vetterling. *Numerical Recipes in Pascal: The Art of Scientific Computing*. Cambridge University Press, 1989.

[76] J.A. Nelder and R. Mead. A simplex method for function minization. *Computer Journal*, 7:308–313, 1965.

[77] I.H. Hutchinson. *Principles of Plasma Diagnostics*. Cambridge University Press, 1987.

[78] J.E. Rice and K.L. and Chamberlain. X-ray observations between 10 and 150 keV from the Alcator-C tokamak. *Physical Review A*, 38(3):1461–67, 1988.

[79] D.R. Baker, M.R. Wade, C.C. Petty, M.N. Rosenbluth, T.C. Luce, J.S. deGrassie, B.W. Rice, R.J. Groebner, C.M. Greenfield, E.J. Doyle, C.L. Rettig, T.L. Rhodes, and M.A. Mahdavi. Particle transport phenomena in the DIII-D tokamak. *Nuclear Fusion*, 40(5):1003–16, 2006.

[80] P. Ricci and B.N. Rogers. Gyrokinetic linear theory of the entropy mode in a Z pinch. *Physics of Plasmas*, 13(062102), 2006.

Appendix A

Magnetics

A.1 Parameters for the magnetic measurements

Number	R [m]	Z [m]	σ_R, σ_Z [mm]	τ [ms]	σ_τ [ms] (1% τ)	# Turns	Gain ($\frac{\#Turns}{\tau}$)
1	0.805	1.428	3	-5.082	0.05	1	-196.8
2	0.905	1.408	3	4.965	0.05	1	201.4
3	1.110	1.361	3	5.325	0.05	1	187.8
4	2.486	0.695	3	21.43	0.21	1	46.67
5	2.515	0.229	3	19.83	0.20	1	50.43
7	1.260	-1.324	3	10.10	0.10	1	99.05
8	1.042	-1.368	3	-10.41	0.10	1	-96.02
9	0.781	-1.425	3	5.029	0.05	1	198.8
10	0.745	1.413	3	-7.702	0.08	5	-649.2
11	0.395	0.863	3	8.382	0.08	10	1193
13	0.169	0.295	3	-7.551	0.08	30	-3973
14	0.100	0.108	3	7.524	0.08	50	6646

Table A.1: Flux loop locations, gains and errors.

Number	R [m]	Z [m]	Θ [deg]	σ_R, σ_Z [mm]	σ_Θ [deg]	τ [ms]	σ_τ [ms] (1% τ)	NA [mm^2]	σ_{NA} [mm^2]	Gain ($\frac{NA}{\tau}$)
1N	0.838	1.527	192	3	1	4.787	0.10	5.225	0.04	1090
1P	0.864	1.482	280	3	1	0.948	0.02	5.453	0.02	5750
2N	1.048	1.476	195	3	1	9.129	0.18	5.056	0.01	554
2P	1.505	1.276	289	3	1	1.921	0.04	4.920	0.004	2560
3N	1.276	1.413	197	3	1	9.130	0.18	5.073	0.003	556
3P	2.051	1.023	117	3	1	4.846	0.10	5.007	0.02	1030
4N	1.499	1.374	199	3	1	9.952	0.20	5.073	0.003	510
4P	2.572	0.515	180	3	1	1.954	0.04	5.236	0.01	2680
5N	1.772	1.298	21	3	1	10.31	0.21	5.214	0.02	506
5P	2.572	-0.362	180	3	1	4.925	0.10	5.197	0.02	1060
6N	2.623	-0.115	90	3	1	5.088	0.10	5.225	0.002	1030
6P	2.559	-0.610	188	3	1	4.783	0.10	5.257	0.001	1100
7N	1.696	-1.286	342	3	1	10.89	0.22	5.067	0.005	465
7P	1.448	-1.311	72	3	1	5.032	0.10	4.980	0.004	990
8N	1.334	-1.400	344	3	1	9.977	0.20	5.214	0.01	523
8P	1.181	-1.381	254	3	1	4.797	0.10	5.312	0.01	1110
9N	1.029	-1.470	167	3	1	10.04	0.20	5.323	0.01	530
9P	0.915	-1.457	78	3	1	4.991	0.04	4.991	0.004	2600

Table A.2: B_p coil locations, gains and errors.

Appendix B

X-rays

B.1 Pre-filter board schematics for X-ray pulse counting

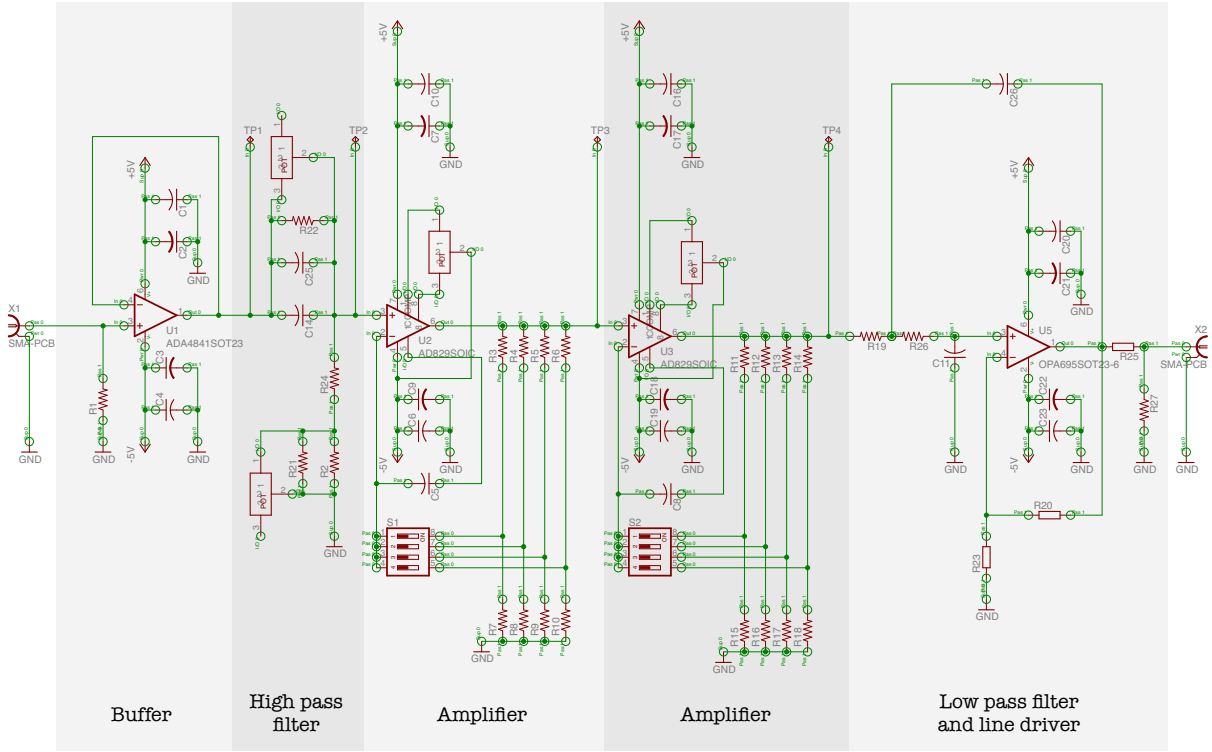

Figure B.1: Schematic of the preamplifier board used with both the SDD and CZT X-ray detectors.

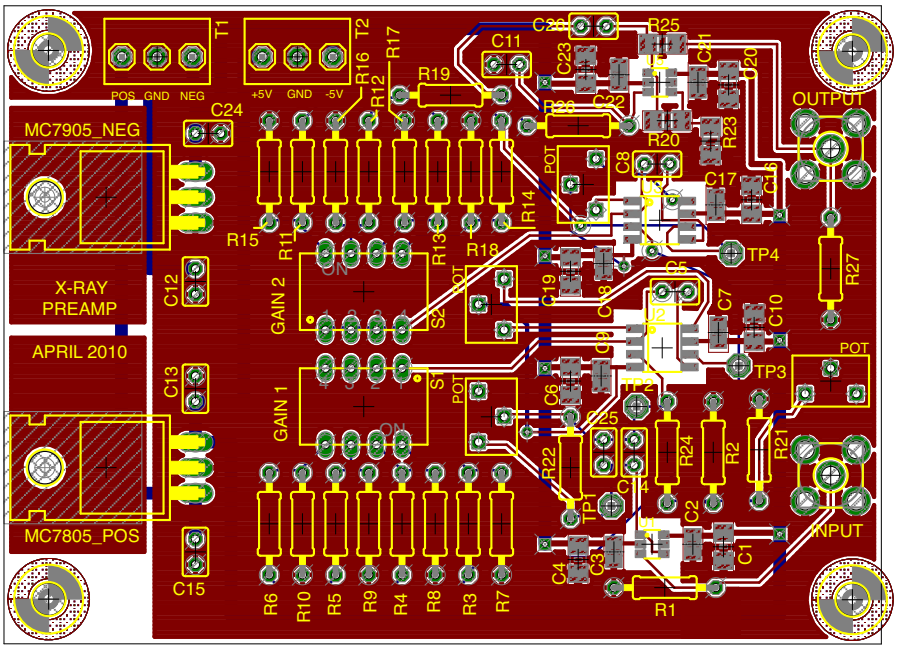

(a)

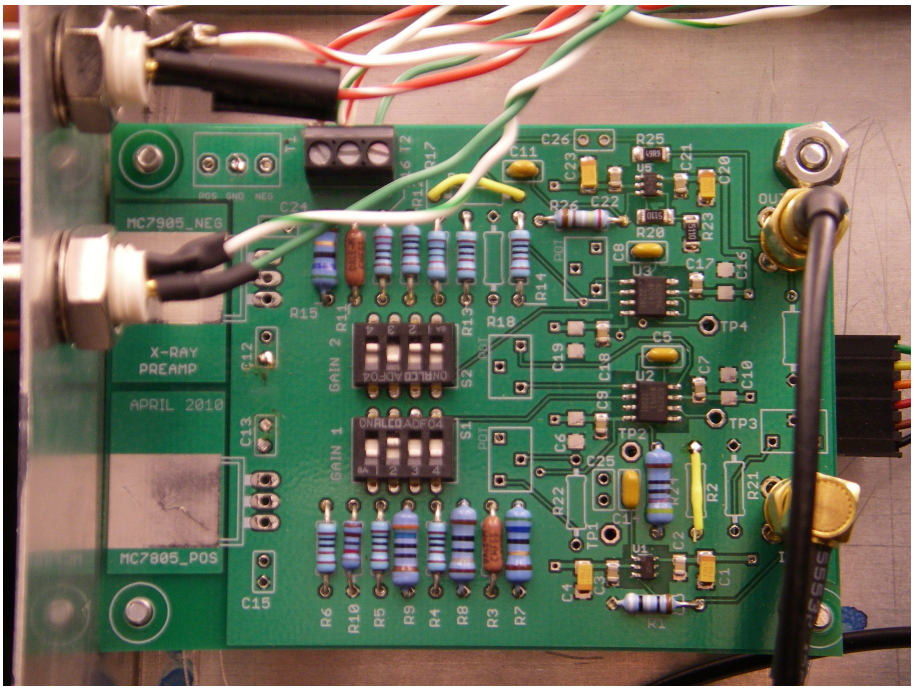

(b)

Figure B.2: (a) Design layout for the preamplifier board. (b) Photograph of the completed preamplifier board.